NSG-3005

PASSIVE MICROWAVE MAPPING OF ICE THICKNESS

John J. Apinis and William H. Peake
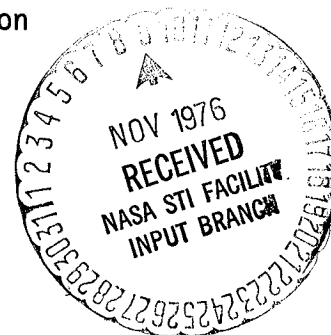
Final Report 3892-2

August 1976

The material contained in this report is also used as a
Dissertation submitted to the Department of Electrical
Engineering, The Ohio State University as partial fulfill-
ment for the degree Doctor of Philosophy

National Aeronautics and Space Administration
Lewis Research Center
Cleveland, Ohio 44135

ABSTRACT

This study presents the basic calculations from which the feasibility of a scanning microwave radiometer system for mapping the thickness of lake ice may be evaluated. An analytical model for the apparent brightness temperature as a function of ice thickness has been developed, and elaborated to include such variables as galactic and atmospheric noise, aspect angle, polarization, temperature gradient in the ice, the presence of transition layers such as snow, slush, and water, increased loss due to air inclusions in the ice layer, and the presence of multiple ice thicknesses within the antenna footprint. It was found that brightness temperature measurements at six or seven frequencies in the range of 0.4 to 0.7 GHz were required to obtain unambiguous thickness estimates. A number of data processing methods were examined; a minimum-distance algorithm and a ternary brightness temperature quantization scheme were found to give accuracies of about 1 cm for ice thicknesses up to one meter. A brief system study of the effects of antenna beamwidth, scanning rate, receiver bandwidth, noise figure, and integration time showed that the receiver sensitivity requirements could be met with state-of-the art components. The radiometric system was found to fail for sea ice thickness measurement due to the very high losses of sea ice.

TABLE OF CONTENTS

iii

CHAPTER I

INTRODUCTION

The ability to map the thickness of lake ice from an aircraft on a routine basis would have important scientific and economic consequences. For example, the shipping season on the Great Lakes could be extended if detailed ice thickness information were available on a daily basis. For a number of reasons, some of which will be discussed in the following paragraphs, the microwave radiometer, Peake (1968), appears to be the appropriate remote sensor for this task. The purpose of this report is to estimate the performance of a microwave radiometer system over a wide range of frequencies, and realistic ice conditions with a view to establishing the feasibility and design parameters of an operational instrument for the remote sensing of lake ice thickness.

The particular choice of microwave radiometer is based on a number of constraints imposed by the problem itself. In the first place, any useful system must be independent of the weather over the ice surface, thus precluding the use of sensors operating in the optical or infrared portions of the spectrum. Secondly, an imaging (i.e., scanning) sensor must estimate ice thickness of the order of a meter or less in the presence of surface roughness which may be a significant fraction of thickness. This requirement precludes the use of the typical active microwave sensors such as the short pulse on carrier, the video pulse, and the side-looking airborne radar (SLAR).

As for the altimeter-type short-pulse radars, these have proved to be quite successful in determining the properties of glacier or polar ice with thicknesses of the order of kilometers, Harrison (1973). The technical problem of producing a pulse modulated carrier with the pulses a few nanoseconds in duration and detecting the reflection from the first surface (air - ice) is not difficult. Such radars have been used successfully to study the wave structure of the ocean, Yaplee (1971). The problem in adapting to lake ice measurements is that of detecting the second surface (ice - water) in the presence of the delayed scattering from the rough first surface. In addition to requiring a smooth first surface, detection requires that the second surface be fairly well defined. For this case (i.e., well defined first and second surface layers), a successful profiling thickness measuring system has been designed and tested, Cooper (1976), Vickers (1974), using an S-band carrier frequency. A more sophisticated carrier system at 3 GHz has been described, Iizuka (1971), with an antenna focussing system. An FM radar for ice and snow measurement has been described by Page (1973). However, a gradual transition from ice to water via a mixture layer of slush would act as an impedance match over several wavelengths of the carrier, even though the thickness of the transition layer was shorter than the pulse length.

A more attractive short-pulse technique is that in which the significant spectral content of the pulse lies in the region for which the wavelength is comparable to the ice thickness, i.e., the video pulse system. Early versions, Meyer (1966), of such systems appeared to give ambiguous results even over smooth ice. However, modern versions, Moffatt (1976), Campbell (1974), with sophisticated antenna designs and data processing procedures should provide a capability for direct measurements of ice thickness. Because these active systems must operate at normal incidence, they provide a profile of the thickness along the flight path, but cannot scan to provide an image. A comparative study of a number of active systems is given by Chang (1976).

Finally, the side-looking airborne radar (SLAR), while it can provide an excellent all weather image of the extent and structure of the ice cover, does not seem adaptable to quantitative measurements of ice thickness. Even if the gray scale of the image was calibrated quantitatively, the observed intensity, particularly for the near grazing angles at the edge of the image, is determined primarily by the first surface scatter. Moderately successful attempts have been made to distinguish various types of ice, but the thickness per se could not be estimated at all, Rouse (1969), Larrowe (1971), Parashar (1974). Thus, active microwave sensors, for a variety of reasons, are not appropriate for producing images of the distribution of ice thickness.

The passive microwave (radiometer) systems, on the other hand, because their primary response is controlled more by dielectric constant than by roughness, appear to offer a good possibility for ice thickness measurement. In a qualitative way the dramatic contrast between the brightness temperature of sea ice (with a dielectric constant of three and an emissivity of over 90%) and water (with emissivities typically of 35% in the microwave region) may be seen in the images reported by, Ladely (1967) at X-band, and by Catoe (1967) at 19 GHz and in the UHF band by Adey (1973). More recently, the routine processing of data from 19 and 35 GHz images in a false color presentation have resulted in the ability to identify and map several categories of sea ice (but not ice thickness) on a synoptic basis, Campbell (1974), Gloersen (1974). Since the quantitative thickness measurement depends on having the electrical wavelength comparable to the layer thickness, these higher microwave frequencies are clearly more suited to layers a few millimeters thick, as one may see from the successful profiling of oil spill thicknesses reported by Hollinger (1973), and by laboratory measurements of ice layers a few millimeters thick reported by Edgerton (1971). More recently, several preliminary attempts have been made to demonstrate the ability of the radiometer as a sea ice thickness sensor in the profiler mode, Adey (1972), Tiuri (1975), using significantly lower frequencies (e.g., 600 MHz). A number of other researchers have experimentally observed the interference phenomenon of layered media, England, Pascalar (1964), Basharinov (1971), Jean (1971), Blinn (1972), Schmugge (1973),

Popov (1976). Thus, measurement of layer thicknesses by radiometric methods may be considered established, but it is clear that the design of a system capable of producing an image of the spatial distribution of ice thickness requires a thorough study before a suitable system configuration can be chosen and the design parameters established.

This report presents the basic calculations from which the feasibility of such a system may be evaluated. A number of figures are used to exhibit the apparent brightness temperature of layers of ice as a function of ice thickness, frequency, polarization, angle of incidence, surface roughness, etc.. Several different multi-frequency measurement systems and data processing methods are also considered. However, before presenting the details of these parametric calculations, it may be useful to provide a qualitative discussion to place the thickness measurement problem in perspective. (For similar discussions from a somewhat different point of view, see England, Popov (1976)).

CHAPTER II

GENERAL FEATURES OF A LAYERED MEDIUM RADIOMETRIC RESPONSE

The brightness temperature T_b of a plane layered medium at a uniform physical temperature T_i (see Figure 2) is composed of two terms

$$T_b = T_{be} + T_{br} \tag{2-1}$$

of which the first, T_{be}, represents the brightness temperature of the radiation emitted by the layers, and the second, T_{br}, represents external radiation reflected by the layers. These two terms may be found from the emission coefficient e of the surface,

$$T_{be} = e\,T_i$$
$$T_{br} = (1-e)(T_g + T_a) \tag{2-2a}$$

where $(1-e) = r$ is the power reflection coefficient of the surface, T_g is the brightness temperature of the incident cosmic radiation and T_a is the brightness temperature of the radiation emitted by the atmosphere.

To illustrate the general features of the response of a radiometer viewing a layer of ice over an (effectively) infinite depth of water, it is sufficient to know the voltage reflection coefficient R for an incident plane wave,

$$R = \frac{R_1 - R_2\,e^{-2\gamma d}}{1 - R_1\,R_2\,e^{-2\gamma d}} \tag{2-3}$$

$$R_1 = (1 - \sqrt{\varepsilon_i})/(1 + \sqrt{\varepsilon_i})$$

$$R_2 = (\sqrt{\varepsilon_w} - \sqrt{\varepsilon_i})/(\sqrt{\varepsilon_w} + \sqrt{\varepsilon_i})$$

where

R_1 = voltage reflection coefficient (air to ice) $\simeq -2/7$

R_2 = voltage reflection coefficient (water to ice) $\simeq +2/3$

d   = thickness of ice

γ = $\alpha + j\beta$ = complex propagation constant in ice

λ_i = wavelength in ice

β = $2\pi/\lambda_i$ propagation constant in ice

α = attenuation constant in ice

ε_i = complex relative dielectric constant of ice

ε_w = complex relative dielectric constant of water   .

For angles of incidence other than normal, one need only replace R_1, R_2 by the Fresnel reflection coefficients appropriate to the incident polarization state, and replace d by ℓ, the path length in the ice, $\ell = d/(1 - \sin^2 \theta_o/\varepsilon_i)^{1/2}$. Note that the rate of oscillation of the reflection coefficient, given by the phase $2\beta\ell$, is independent of polarization and only weakly dependent on angle of incidence. The magnitude of the oscillation is controlled by the reflection coefficients, and these are also almost independent of look angle for favorable polarization states (circular polarization or 45° linear).

If, for the purposes of a qualitative discussion, one assumes that the reflection coefficients R_1, R_2 are real, then the emission coefficient of the surface, $e = 1 - r^2$ has the form

$$e = \frac{(1 - r_i)(1 - A r_w)}{(1 + A r_i r_w + 2\sqrt{A} r_i r_w \cos 2\beta d)} \qquad (2\text{-}4)$$

$r_i = R_i R_i^*$ power reflection coefficient (air to ice) $\simeq 2/25$

$r_w = R_w R_w^*$ power reflection coefficient (ice to water) $\simeq 4/9$

$r = 1-e = RR^*$ power reflection coefficient of layers.

$A = \exp(- 4\alpha d)$.

To illustrate the behavior of the reflection coefficient, Figure 1 shows T_{be} as a function of d/λ_i (the ice thickness in wavelengths) for various values of the parameter α/β. (An attenuation of 1 dB/wavelength in ice corresponds to $\alpha/\beta = (40\pi \log_{10} e)^{-1} = .0183$.)

For fresh water ice, with attenuation of the order of 1 to 3 dB per meter, (approximately independent of frequency) in the lower microwave range, the curve $\alpha/\beta = 0$ illustrates the general behavior of the brightness temperature dependence. For sea ice, with much higher attenuations, the curves $\alpha/\beta = 0.1$ or 0.3 may be more representative.

Note that these curves represent ice with constant attenuation per wavelength (i.e., α proportional to frequency), whereas both sea ice and fresh water ice tend to have α independent of frequency. It is significant, however that even for the case $\alpha/\beta = 0.3$, representing an attenuation higher than any likely to be encountered in fresh water ice, the period of the oscillations of T_{be} with thickness is essentially unchanged.

The nature of these oscillations may be placed in better perspective by writing Equation (2-4) as a Fourier cosine series

$$T_b = \frac{T_i (1 - r_i)(1 - A r_w)}{(1 - A r_i r_w)} [1 - 2 (r_i r_w A)^{1/2} \cos 2\beta d$$

(2-5a)

$$+ 2 (r_i r_w A) \cos 4\beta d - 2(r_i r_w A)^{3/2} \cos 6\beta d + \dots$$

$$= \sum T_n \cos 2n\beta d \qquad n = 0,1,2 \dots$$

(2-5b)

which, for $\varepsilon_1 = 3.1$, $\varepsilon_w = 78$, $\alpha = 0$ becomes, as an illustration

$$T_{be} = 145 - 53 \cos 2\beta d + 10 \cos 4\beta d - \dots \,^\circ K.$$

(2-6)

Similarly, the reflected contribution is given by the corresponding series

$$T_{br} = (T_g + T_a) \frac{(1 - r_i)(1 - A r_w)}{(1 - A r_i r_w)} [A_0 + 2(r_i r_w A)^{1/2} \cos 2\beta d$$

$$- 2(r_i r_w A) \cos 4\beta d + \dots]$$

$$= \sum T_n' \cos 2n\beta d \qquad n = 0,1,2 \dots$$

(2-7)

$$A_0 = (r_i + A r_w - 2 A r_i r_w)/((1 - r_i)(1 - A r_w)) \simeq 0.89$$

which, for $T_g + T_a = 1000^\circ K$ becomes, as an illustration,

$$T_{br} = 470 + 200 \cos 2\beta d - 37 \cos 4\beta d + \dots$$

(2-8)

6

In the series form, the effect of changes in attenuation, finite instrument bandwidth, and fluctuation in ice thickness are easily found. For example, if the radiometer has an ideal band pass filter characteristic, passing frequencies corresponding to the range $\pm\Delta\beta/2$, and the ice thickness within the antenna footprint is uniformly distributed in the range $d \pm \Delta d/2$, then the averaged T_{be} becomes approximately, for ice of fairly low attenuation,

$$\bar{T}_{be} = \sum_0^\infty T_n \left(\frac{\sin nd\Delta\beta}{nd\Delta\beta}\right)\left(\frac{\sin n\beta\Delta d}{n\beta\Delta d}\right) \cos 2n \beta d \qquad (2\text{-}9)$$

i.e., the amplitude of each harmonic is simply reduced by the two "sin x/x" factors; larger attenuations will produce further small changes in the coefficients T_n over and above the explicit factor $A^{n/2}$ exhibited in Equation (2-3a). Similar effects due to random fluctuations in dielectric constant are discussed in Tsang (1976). A more detailed discussion of the effects of finite bandwidth for various bandpass shapes, is given in Popov (1976). The effects of a finite beamwidth may also be found by averaging over the range of path lengths $\ell(\theta)$ determined by the range of look angles in the beam.

The behavior of the total perceived brightness temperature T_b will depend on the relative magnitudes of the temperatures (T_g+T_a) and $T_i \simeq 270°K$. At low frequencies, below about 150 MHz, the cosmic noise temperature T_g is much larger than T_i, and strongly frequency dependent Ko, (1958). Typically, the major portion of the radio sky has temperatures larger than $T_g > 2/f^{2.7}$ (f in GHz); for frequencies around 0.1 GHz this may conveniently by written $T_g \simeq 1000/(f/\cdot 1)^{2.7}$. Thus below 150 MHz or so T_b is dominated by the reflected term

$$T_b \simeq T_{br} = \sum T_n' \cos 2 \beta nd \qquad T_n' \text{ from (2-7)}$$

and since the signs of T_n' are opposite those of T_n (n<0), the oscillation of T_{br} will be 180° out of phase with those shown in Figure 1.

Above 350MHz on the other hand, $T_g < 80° K$ over most of the radio sky and the brightness is dominated by emission,

$$T_b \simeq T_{be} = \sum T_n \cos 2 \beta nd \quad . \quad T_n \text{ from (2-5)}$$

At intermediate frequencies, between 150 MHz and 350 MHz, as will be seen subsequently (see, e.g., Figure 6) the two components of brightness are comparable in magnitude, and the variation of brightness with ice thickness depends on the (usually unknown) ratio T_g/T_i.

7

From the perspective of the two cosine series (2-5b) and (2-7) for T_{br} and T_{be}, the approach to a thickness measuring system becomes evident. At one extreme, (see Figure 1) it is possible to operate in the first half cycle of cos 2 βd, thus avoiding any problems of ambiguity by restricting the phase to lie in the range $0 < 2$ βd $< \pi$. For ice of one meter thickness, this requires $f < c/(4$ $d\sqrt{\epsilon_i}) \simeq 42$ MHz. At these frequencies, the brightness T_b is completely dominated by the reflected cosmic noise. Since the cosmic noise will vary (it is dependent on the direction of the flight path and angle of incidence) one must either measure T_g with an upward looking antenna, or avoid the problem by making certain assumptions about the behavior of T_g. For example, if it is assumed that T_g has a power dependence on frequency, $T_g = c/f^m$ where c is a constant, one might estimate the thickness by observing the reflected brightness temperature and its derivative

$$\left(\frac{T_{br}}{f}\right) \Big/ \left(\frac{dT_{br}}{df}\right) = \frac{-(T_0'/T_i' + \text{Cos } \psi)}{m(T_0'/T_i' + \text{Cos } \psi) + \psi \text{ Sin } \psi}$$

$$T_0'/T_i' = A_0/2\sqrt{r_i\ r_w\ A}$$

$$\psi = 2\beta\ell \tag{2-10}$$

This transcendental equation is now independent of T_g, and will have unambiguous solutions if ψ is somewhat less than π, i.e., the system would be restricted to frequencies below about 42 MHz. More eleborate systems, operating at somewhat higher frequencies ($\sim$ 100 MHz) are discussed in Chapter III. These systems reduce, but do not eliminate the effects of ambiguity by utilizing two or three frequencies.

The more straightforward method for estimating ice thickness is made evident by Equation (2-5) and Figure 1, both of which indicate that the period of oscillation of $T_{be}(2\beta d)$ is changed only slightly by attenuation, instrument bandwidth, or small variations in ice thickness, although both the "dc" level of the oscillations and their amplitude may vary. To extract the thickness, it is only necessary to sample the brightness at a sufficient number of different frequencies to establish the period of $2\beta\ell$. The number of frequencies required, and their separation, may be estimated from the sampling theorem, and the required maximum and minimum
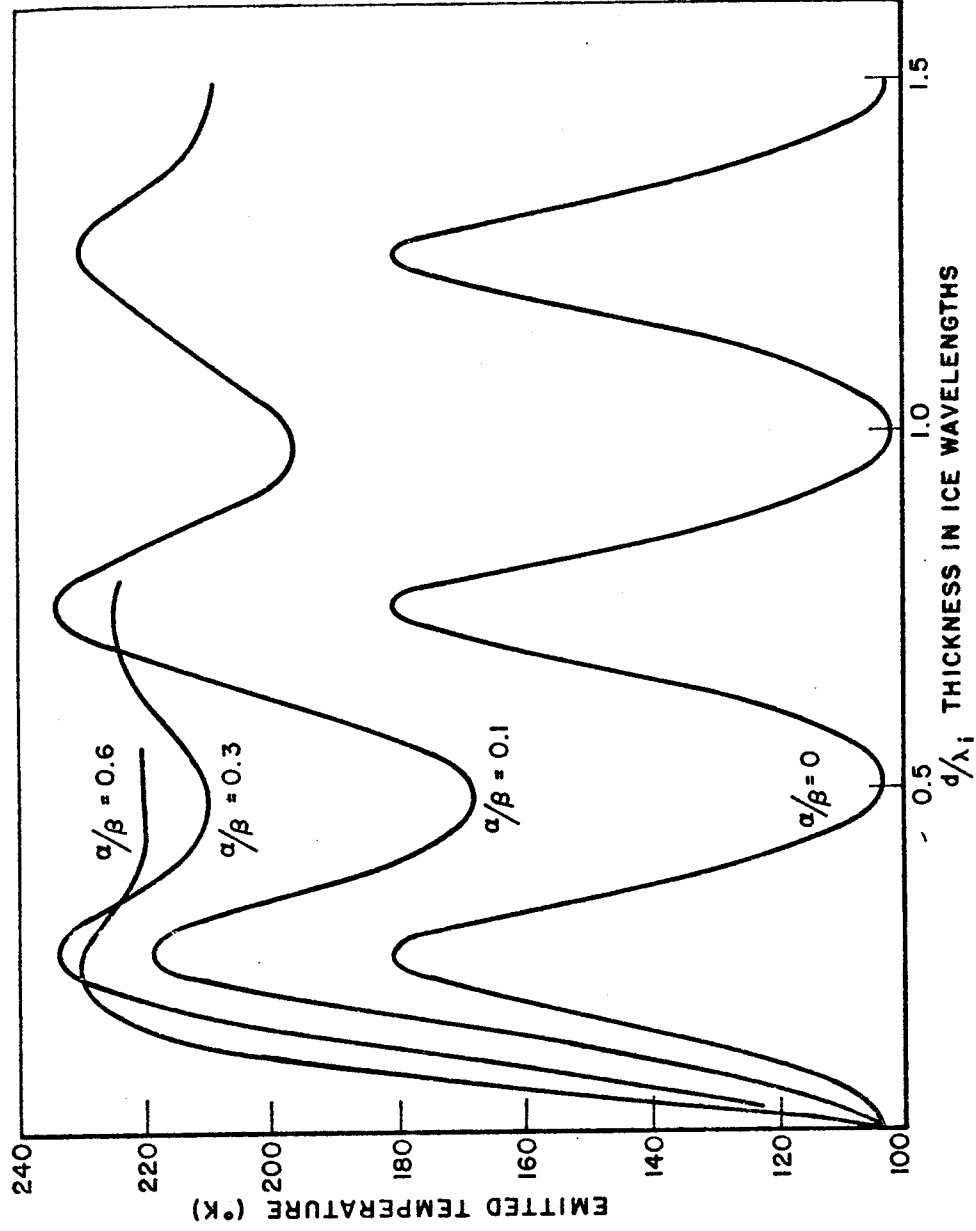
Figure 1. The emitted brightness temperature T_{be} as a function of ice layer thickness, and ice attenuation. $T_g = T_a = 0$, $T_i = 270°K$

ice thickness of interest d_{max} and d_{min}, respectively.

To establish the frequency interval between channels, note that the sampling theorem requires that $T_b(2\beta d)$ be sampled twice per period for the thickest ice to be measured. Thus, the frequency interval df between channels must be

$$df < c/(\sqrt{\varepsilon_i} \, 4 \, d_{max}) \qquad c = 3 \times 10^8 \text{ m/sec} \qquad (2-11)$$

i.e., less than 43 MHz for ice with $d_{max} = 1$ meter. On the other hand, because at least one half period must be established for the thinnest ice, the total span of frequencies Df must be greater than

$$Df > c/(\sqrt{\varepsilon_i} \, 4 \, d_{min}) \qquad (2-12)$$

and the number of frequencies required is $N \geq (d_{max}/d_{min} + 1)$.

The choice of the highest usable frequency will be determined by the uniformity in ice thickness, because the amplitude of oscillation of $T_b(2\beta d)$ is diminished by the factor $\sin(\beta \Delta d)/(\beta \Delta d)$. Thus, if one assumes that $\beta \Delta d = 2\pi/3 = x$ (so that $\sin x/x = .4$), then the highest usable frequency f_{max} is given by

$$f_{max} = c/(3 \sqrt{\varepsilon_i} \, \Delta d) \qquad (2-13)$$

Thus, if Δd is, say, 10 cm, then $f_{max} = .86$ GHz. The lower limit, in practice, will be determined by problems of antenna size, and by the fact that below about 350 MHz, the magnitude and variability of the reflected cosmic noise significantly influences the perceived brightness temperature of the ice layer.

Thus, the basic "brute-force" design for an ice thickness measuring system would consist of a circular or 45° linear polarized, multifrequency radiometer with $N \geq (1 + d_{max}/d_{min})$ channels, with

a frequency separation between channels of $df = c/(4 \sqrt{\varepsilon_i} \, d_{max})$ a highest frequency less than $f_{max} < c/(3 \sqrt{\varepsilon_i} \, \Delta d)$, and a lowest frequency that should be somewhat above $f_{min} > 300$ MHz. For an airborne imaging system, the image can be generated by scanning across the flight path, or by utilizing simultaneous multiple

beams. In the former case (i.e., scanning, which presents the more severe requirement on system sensitivity), it is not hard to show that if the angular resolution (antenna beamwidth) is θ_B radians and the system sensitivity (precision in measuring brightness temperature) is ΔT_B °K, then a system figure of merit is given by the product, Peake (1968),

$$\theta_B \ \Delta T_B \cong 2 \ T_{in} \ \sqrt{\frac{V/H}{B}} \tag{2-14}$$

where

B = bandwidth of individual radiometer channel (Hz)

V = vehicle velocity (m/s)

H = vehicle altitude (m)

$T_{in} = (F - 1) \ T_o + T_A$

F = receiver noise figure with T_o = 290° K

T_A = antenna temperature $\cong T_B$.

For an aircraft with V/H $\cong$ .08 sec^{-1}, B = 5 MHz, T_{in} = 500° K, for example,

$$\Delta T_B \ \theta_B = 1/8 \ (°K\text{-radians}).$$

Such a radiometer with, say, 10° angular resolution ($\theta_B \cong 1/6$) would allow a precision in measuring T_B of $\Delta T_B \cong .75°$ K, while a system with 3° angular resolution ($\theta_B \cong 1/20$) would have ΔT_B = 2.5° K.

It will appear subsequently that errors in measuring T_B of as much as 5° K will not seriously affect the ability of a system to estimate ice thickness. From the superficial view of system design implied by Equation (2-8), it is clear that the limited dwell time imposed by the scanning requirement would not become a problem (to be solved, for example, by multiple simultaneous beams) except for systems with high resolution (beamwidths less than a few degrees) or with large V/H ratios. Furthermore, the required radiometer system performance is well within the current state-of-the-art for radiometer hardware. Thus, the major technical problem in producing an imaging, thickness measuring radiometer is the development of a flyable, low loss, low VSWR, multichannel, scannable (or multibeam) antenna in the 300 MHz to 800 MHz frequency range. The antenna design problem is not considered in this report, the remainder of which is devoted to justifying the statements made in this brief survey, and to developing a system which will produce valid ice thickness estimates with as small a number of radiometer channels as possible.

APPARENT BRIGHTNESS MODEL OF A LAYERED MEDIUM

0.   Introduction

In this section, the theory for calculating the apparent brightness temperature of a layered medium is reviewed and used to calculate the expected brightness of a smooth ice layer over water. In order to introduce the several physical parameters controlling the perceived brightness, the case of normal incidence with ice and water at the same temperature is considered first. In the following chapter, the model is elaborated to include the effects of transition layers of various types.

1.   Brightness Model Geometry

The basic problem geometry is shown in Figure 2. An infinitely deep layer of fresh water is assumed to be covered by a layer of ice of uniform thickness d. The ice temperature T_i and water temperature T_w are both assumed to be 273° K. The surface layer is illuminated by galactic noise T_g and atmospheric noise T_a. The observing antenna will then receive two contributions from the direction of the surface, namely the reflected sky noise temperature and the noise temperature emitted by the ice and water. The total apparent brightness temperature T_b of the radiation incident on the antenna is then given by

$$T_b = \underbrace{(1 - |R|^2)\, T_i}_{\text{emission } (T_{be})} + \underbrace{|R|^2\, (T_g + T_a)}_{\text{reflection } (T_{br})} \qquad (3\text{-}1)$$

where

    R is the voltage reflection coefficient of the ice-water combination

    T_i is the physical temperature of the ice and water

    T_g is the brightness temperature of the galactic noise

    T_a is the brightness temperature of the atmospheric noise.

For normal incidence,

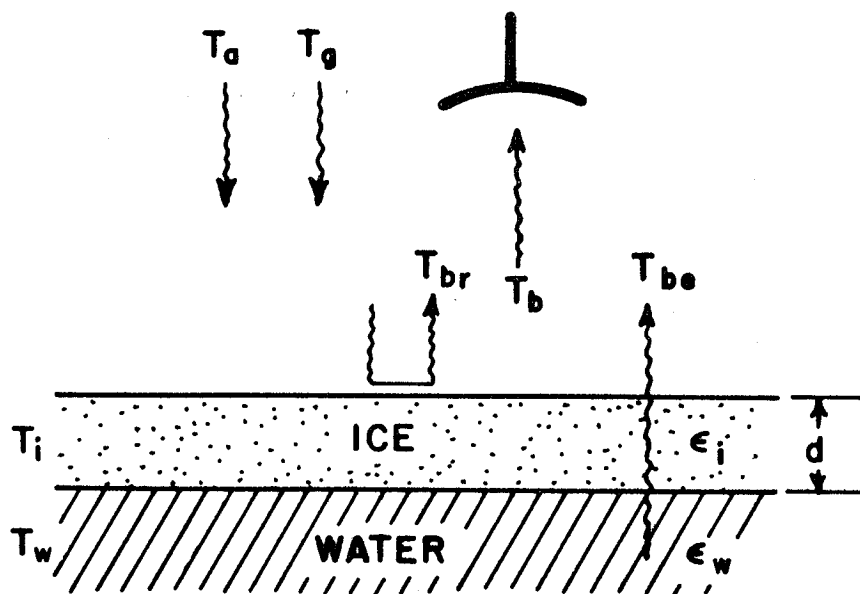$$R = \frac{Z_1 - Z_0}{Z_1 + Z_0} \qquad (3\text{-}2)$$

where

Figure 2. The apparent brightness temperature of the ice layer/
water system is the sum of the emitted component
$T_{be}=(1 - |R|^2)$ T_i, and the reflected component $T_{br}=$
$|R|^2$ $(T_g + T_a)$.

$$Z_0 = \sqrt{\frac{\mu_0}{\epsilon_0}} \approx 377 \,\Omega$$

$$Z_1 = Z_i \frac{Z_w + Z_i \tanh \gamma_i d}{Z_i + Z_w \tanh \gamma_i d}$$

$$Z_i = \frac{Z_0}{\sqrt{\epsilon_i}} \qquad Z_w = \frac{Z_0}{\sqrt{\epsilon_w}} \qquad \gamma_i = \frac{j\omega}{c} \sqrt{\epsilon_i}$$

and

ϵ_i is the relative complex dielectric constant of ice

ϵ_w is the relative complex dielectric constant of water

d is the thickness of the ice layer

Z_0 is the free space impedance

Z_i is the ice impedance

Z_w is the water impedance

γ_i is the complex propagation constant in ice

c is the free space propagation velocity   .

This basic model assumes:

- the apparent brightness temperature is observed at normal incidence

- the ice layer has a smooth surface on the top and bottom

- the top surface of the ice is free of snow, slush, or water

- the bottom surface of the ice has no slush at the ice-water interface

- the ice layer has no air bubbles in it

- the water and ice are at the same uniform temperature.

The effect of relaxing each of these model constraints will be considered in the following chapter. Before doing so, the input parameters ϵ_w, ϵ_i, T_g, and T_a will be defined.

14

2. Brightness Model Parameters

A. Water Model

The dielectric constant of water may be represented by an equation of the Debye form. The particular model used in this report is the one developed by Stogryn (1971).

$$\varepsilon_W = \varepsilon_{\infty W} + \frac{\varepsilon_{dw} - \varepsilon_{\infty W}}{1 + j\, 2\, \pi \tau\, f} - j\, \frac{\sigma}{2\, \pi\, \varepsilon_0\, f} \qquad (3\text{-}3)$$

where

$\varepsilon_{\infty W}$ is the high frequency dielectric constant

S is the salinity in parts per thousand

T is the temperature in °C

N is the normality of the solution

ε_{dw} is the static dielectric constant

σ is the ionic conductivity of the dissolved salts

τ is the relaxation time in seconds

f is the frequency in Hz

$\varepsilon_{\infty W}$ = 4.9

$N = S(1.707 \times 10^{-2} + 1.205 \times 10^{-5}\, S + 4.058 \times 10^{-9}\, S^2)\, .9141$

$a = 1.0 - 0.2551\, N + 5.151 \times 10^{-2}\, N^2 - 6.889 \times 10^{-3}\, N^3$

$\varepsilon_{dw} = a(87.74 - 0.4008\, T + 9.398 \times 10^{-4}\, T^2 + 1.410 \times 10^{-6}\, T^3)$

$\Delta = 25.0 - T$

$g = 2.003 \times 10^{-2} + 1.266 \times 10^{-4}\Delta + 2.464 \times 10^{-6}\, \Delta^2 -$
$\qquad S(1.849 \times 10^{-5} - 2.551 \times 10^{-7}\Delta + 2.551 \times 10^{-8}\, \Delta^2)$

$\sigma = S(0.182521 - 1.46192 \times 10^{-3}\, S + 2.09324 \times 10^{-5}\, S^2 -$
$\qquad 1.28205 \times 10^{-7}\, S^3)\, \exp\, (-\Delta g\,)$

$$b = 0.1463 \times 10^{-2} \, N \, T + 1.0 - 0.04896 \, N - 0.2967 \, N^2 + 5.644 \times 10^{-3} \, N^3$$

$$2\pi\tau = b(1.1109 \times 10^{-10} - 3.824 \times 10^{-12} \, T + 6.938 \times 10^{-14} \, T^2 - 5.096 \times 10^{-16} \, T^3)$$

$$\varepsilon_0 = 8.854 \times 10^{-12} \text{ farads/m} \quad .$$

These equations are for sea water of standard composition. A recent study by Klein and Swift shows that for a NaCl solution, the factor .9141 in the expression for the normality N should be replaced by unity.

B. Ice Model

The model for the dielectric constant of the ice layer, as for the water, is of the Debye form. The main difference between the two is that the relaxation frequency for ice is in the KHz range and for water in the GHz range. The relative complex dielectric constant of fresh water ice is given by

$$\varepsilon_i = \varepsilon_{\infty i} + \frac{\varepsilon_{di} - \varepsilon_{\infty i}}{1 + jf/f_0} \qquad (3-4)$$

where

$\varepsilon_{\infty i}$ is the high frequency dielectric constant

ε_{di} is the static dielectric constant

f_0 is the relaxation frequency in Hz

T is the temperature in °K

$\varepsilon_{di} = 90. - (T - 273.) \, 0.3581$

$\varepsilon_{\infty i} = 2.846 + 0.001333 \, T$

$f_0 = a_4 \, T^4 + a_3 \, T^3 + a_2 \, T^2 + a_1 \, T + a_0$

$a_4 = 0.11666643 \times 10^{-4}$

$a_3 = -0.11573310 \times 10^{-1}$

$a_2 = 0.43053546 \times 10^{1}$

$a_1 = -0.71170619 \times 10^{3}$

$a_0 = 0.44104997 \times 10^{5} \quad .$

16

These parameters were derived by fitting the Debye model to measurements of Hasted (1961), and Iglesias (1967). A comparison of the loss tangent given by this ice model with the measurements upon which it is based is shown in Figure 3. The real part of the relative complex dielectric constant shows no dependence on frequency but does decrease from 3.21 to 3.18 as the temperature decreases from 0°C to -40°C. This ice model corresponds to very good ice, i.e., ice without air bubbles, cracks, etc.. At frequencies well above the relaxation frequency (a few KHz), this model produces a loss tangent that is approximately proportional to wavelength so that the attenuation is roughly frequency independent. ($\alpha \simeq$ 163 * tan δ * f in dB/meter with f in GHz.) The values of attenuation recently measured for actual lake ice, Vickers (1975), ranged from 1 to 3 dB/meter (depending on the condition of the ice), almost independent of frequency in the range 1 to 10 GHz; these attenuations correspond to

.006/f < tan δ <.019/f with f in GHz.

C.   Galactic Noise Model

The noise temperature contribution T_g from the galaxy is variable with time, frequency, and direction. For the purposes of the calculations made here, it will be assumed that the cosmic background is isotropic but of variable intensity with a (-2.7) power dependence on frequency. The model used is

$$T_g = G/f^{2.7} \text{ °K} \qquad\qquad (3-5)$$

where

G is the galactic temperature factor ($2 \leq G \leq 40$)

f is the frequency in GHz.

The bounds of possible galactic temperatures are shown in Figure 4. The actual temperature distribution in the sky has a complex structure, Ko (1958), including individual radio sources. Figure 5 shows typical radio maps of the sky at several different frequencies. The effective T_g is thus not only a function of position in the sky but of the antenna beamwidth as well. For this reason, Figure 4 can be considered only as an approximation for the temperature which might be encountered. The maximum temperature (G = 40) would be observed in the direction of the galactic center, but the brightness falls off rapidly toward the minimum (G = 2) as the look direction moves toward the direction of the galactic pole. The solid angle subtended by any given brightness temperature contour also decreases
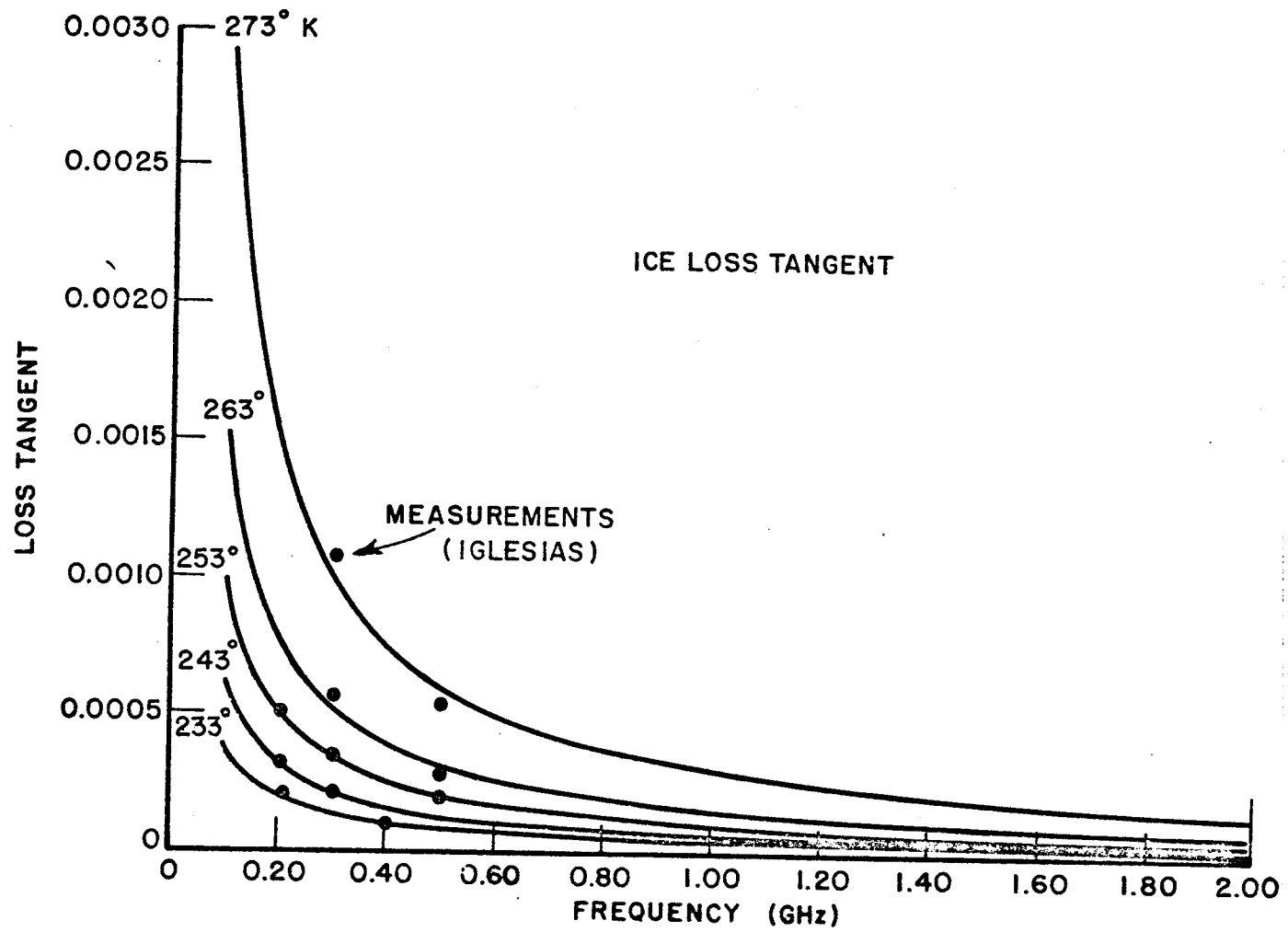
Figure 3. The loss tangent of an ice model fitted to measurements presented by Iglesias.

GALACTIC NOISE TEMPERATURE

$T_g = G/f^{2.7}$

G=40

G=2
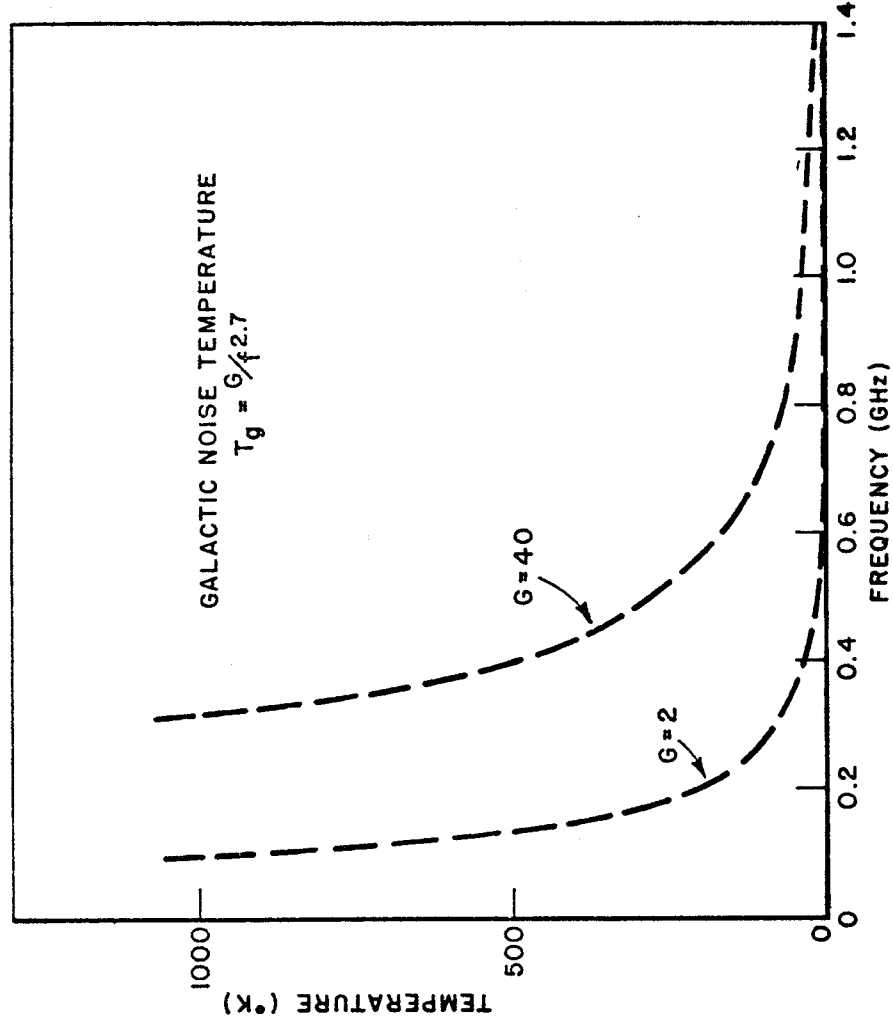
Figure 4.   The extremes of galactic noise temperature which may be encountered.

19
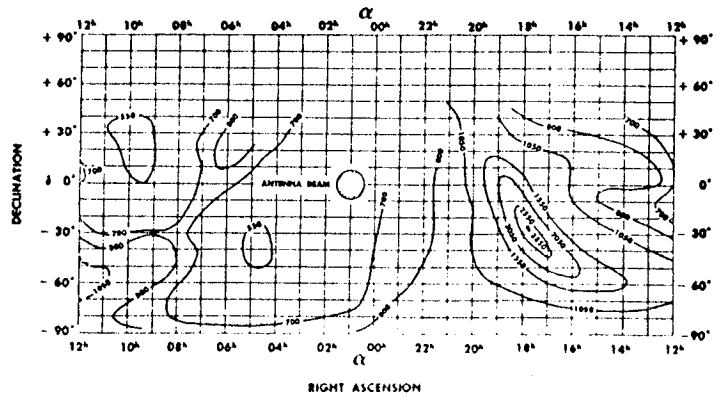
100 MHz MAP (AFTER BOLTON AND WESTFOLD)
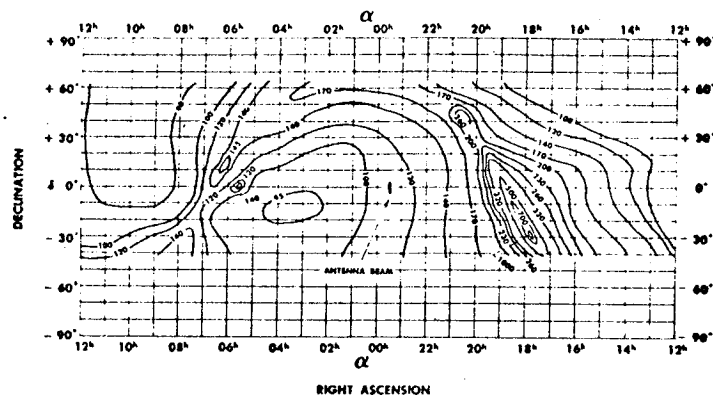
250 MHz MAP (AFTER KO AND KRAUS)
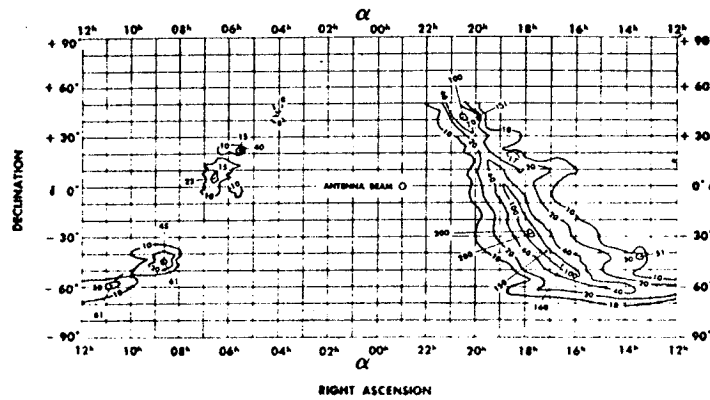
600 MHz MAP (AFTER PIDDINGTON AND TRENT)

Figure 5. Actual galactic temperature distribution in the sky for three different frequencies.

20

rapidly with frequency. Thus, to evaluate precisely the cosmic
noise contribution for any particular mission, it would be necessary
to take into account the actual antenna pattern and the flight
path, relative to the galactic coordinates.

A general survey of the cosmic noise distribution over the
entire range of frequencies of interest here is given by Ko (1958).
The sky maps of Figure 5 are taken from this reference. More
detailed brightness maps are given by Seeger (1959) and Landecker
(1970) at 400 MHz and 150 MHz respectively.

D. Atmospheric Noise Model

The atmospheric noise model is based on data published by Hogg
(1961). The atmospheric contribution to the sky temperature at low
frequencies (1 GHz or less) shows little dependence on humidity,
and consequently, all calculations are made assuming the standard
atmosphere. In the frequency range 0.1 GHz to 1.0 GHz, the
atmospheric noise contribution is on the order of 5°K or less.

E. Urban Noise

In addition to the universally present cosmic and atmospheric
noise, there are locally severe sources of man-made noise which
may influence radiometer operation. The coherent sources of man-
made radiation include radar, television, communications equipment,
navigation aids, etc.. These sources of interference are a function
of frequency band and geographic location and will not be considered
in detail here. The incoherent noise is due to such sources as
ignition systems, power lines, and electric motors. Investigation
of this type of noise has been reported by a number of authors,
Ploussios (1968), Skomal (1969). It has been found that the
measured temperatures over large urban areas may be quite high,
many thousands of degrees at 369 MHz for example, but that the
brightness decreases rapidly beyond the limits of urbanization.
For example, the brightness temperature dropped from 48000 °K to
∿ 300 °K in one mile as an aircraft flying at 2000 feet passed
over Newark, New Jersey, Ploussios (1968). Thus, an aircraft flying
at a few thousand feet, a mile or more off-shore would not be
expected to experience interference from incoherent urban noise.
A special investigation, however, would have to be made to ensure
that the chosen radiometer frequencies do not coincide with possible
sources of coherent interference.

3. Brightness Model Power Reflection

Coefficient and Temperature

As can be seen from Equations (3-1) and (3-2), the apparent
brightness temperature depends on the reflection coefficient, and

this in turn is a function of the ice layer thickness d. A
representative plot of the reflection coefficient as a function
of d for two different frequencies is shown in Figure 6. The
apparent brightness temperatures corresponding to those frequencies
for three different levels of galactic temperature are shown in
Figures 7(a), (b), and (c). The power reflection coefficient is
also a sinusoidal function of frequency. Figure 8 shows the
frequency dependence of the power reflection coefficient for two
different ice thicknesses. The corresponding brightness temper-
atures are shown in Figures 9 (a), (b), and (c) for several
galactic temperatures. The model assumed here for good ice has
very small but non-zero loss. Thus, as the thickness of the
ice layer increases, it will tend to become more absorptive. This
effect can be seen in Figure 8., where the oscillation in the power
reflection coefficient for the 100 cm ice layer is somewhat smaller
than for the 10 cm layer. Similarly, the emissivity increases with
corresponding slight increases in apparent brightness temperature,
as shown in Figure 9 (a), (b), and (c).
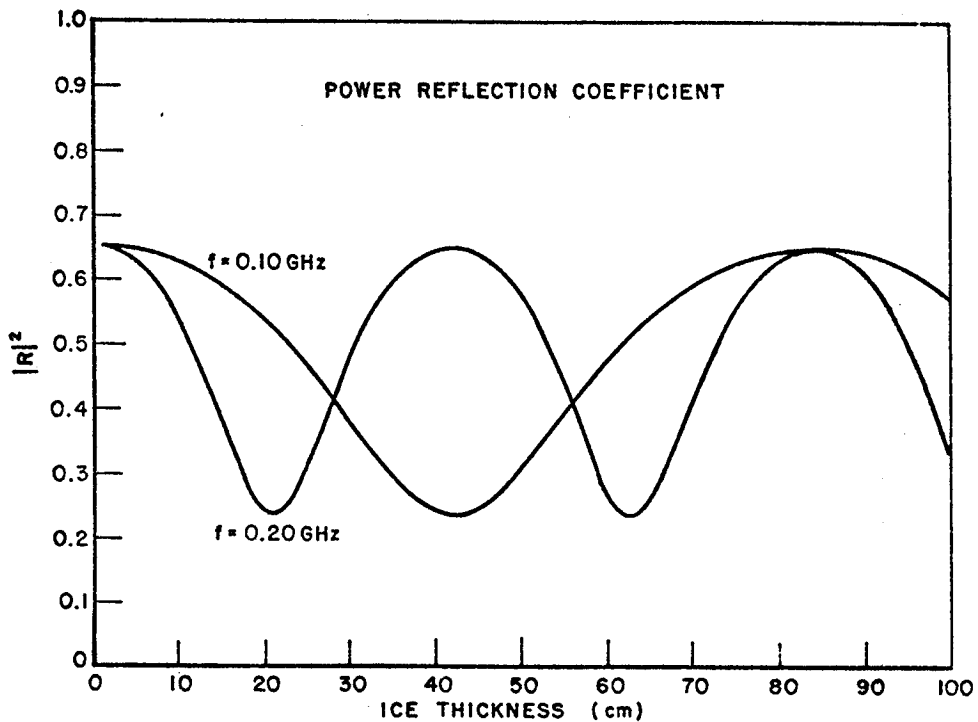
Figure 6. The power reflection coefficient of the ice layer
as a function of the layer thickness for two
different frequencies.

APPARENT BRIGHTNESS TEMPERATURE

$T_g = 2/f^{2.7}$

f = 0.10 GHz

f = 0.16 GHz

f = 0.30 GHz

(a)

APPARENT BRIGHTNESS TEMPERATURE

$T_g = 20/f^{2.7}$

f = 0.30 GHz

f = 0.38

f = 0.50 GHz

(b)

Figure 7. The apparent brightness temperature of the ice layer as a function of layer thickness and magnitude of galactic temperature.
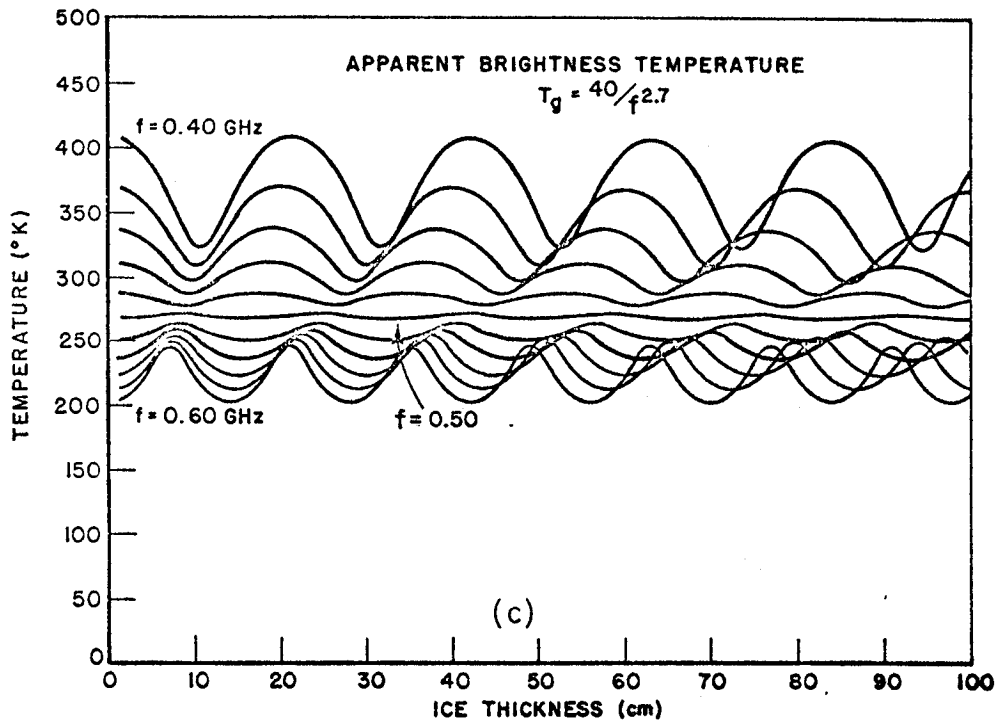
Figure 7 (c). The apparent brightness temperature of the ice
layer as a function of layer thickness and
magnitude of galactic temperature.
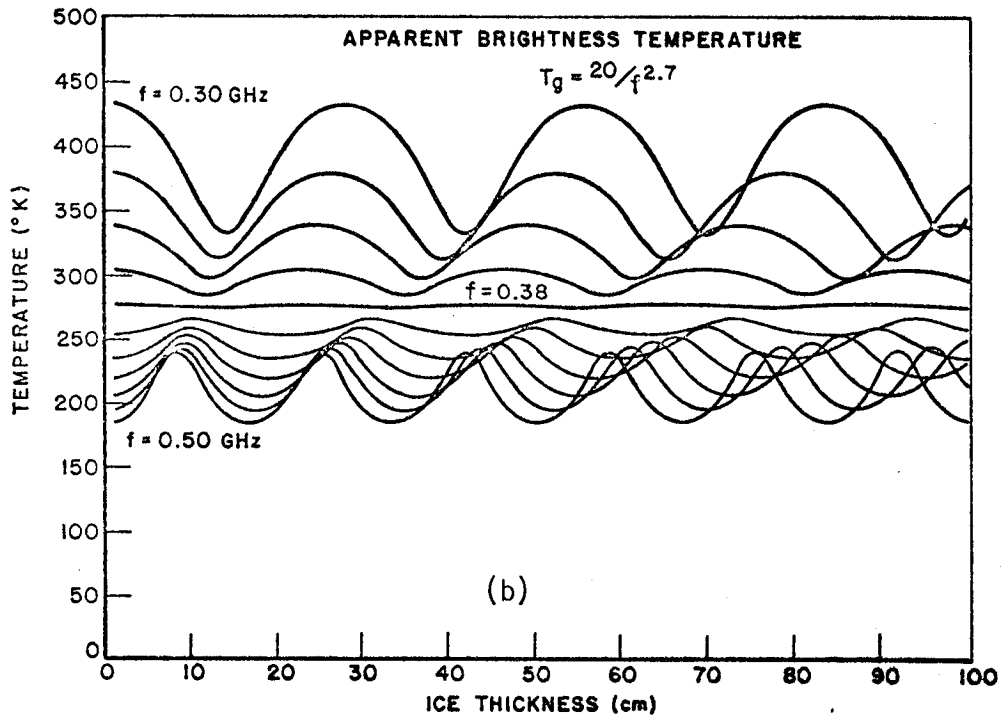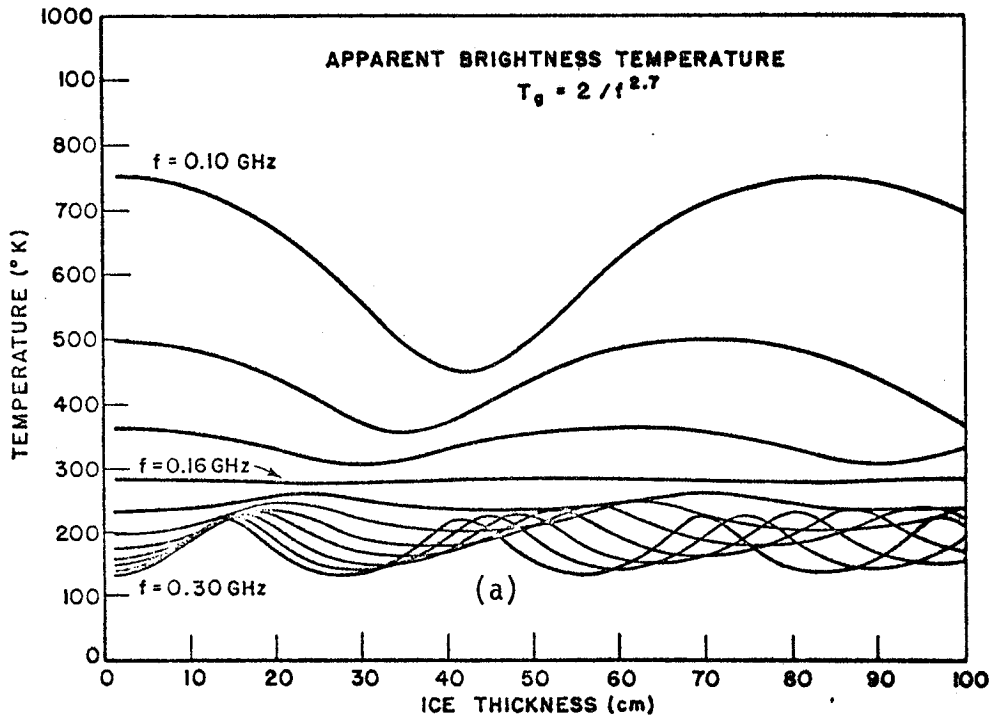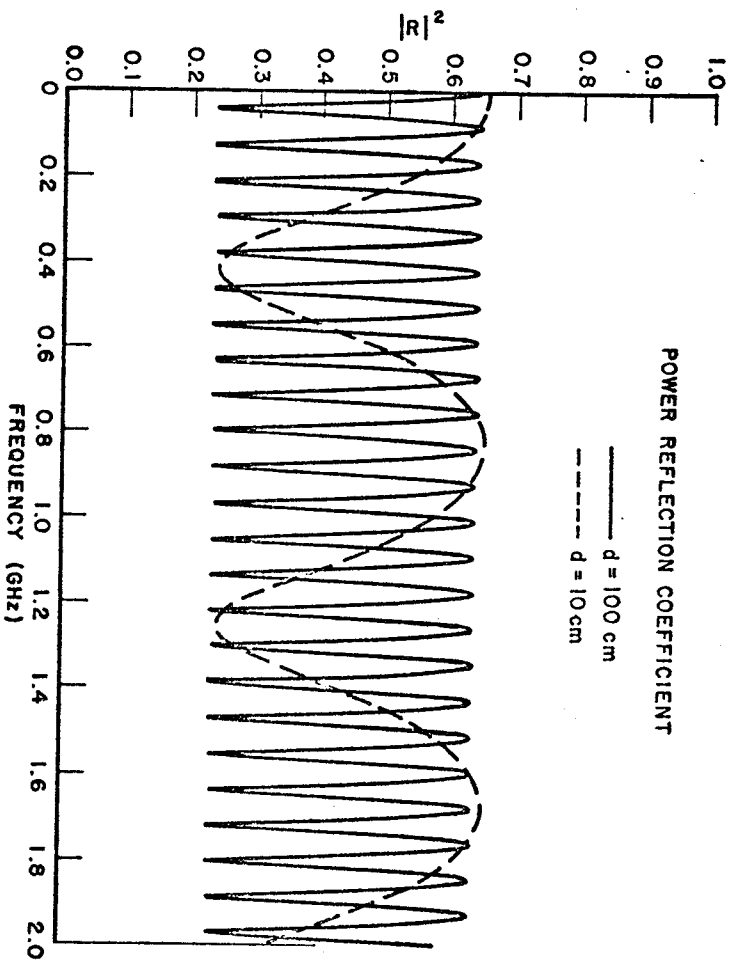
Figure 8. The power reflection coefficient as a function of frequency for two different ice layer thicknesses.

25
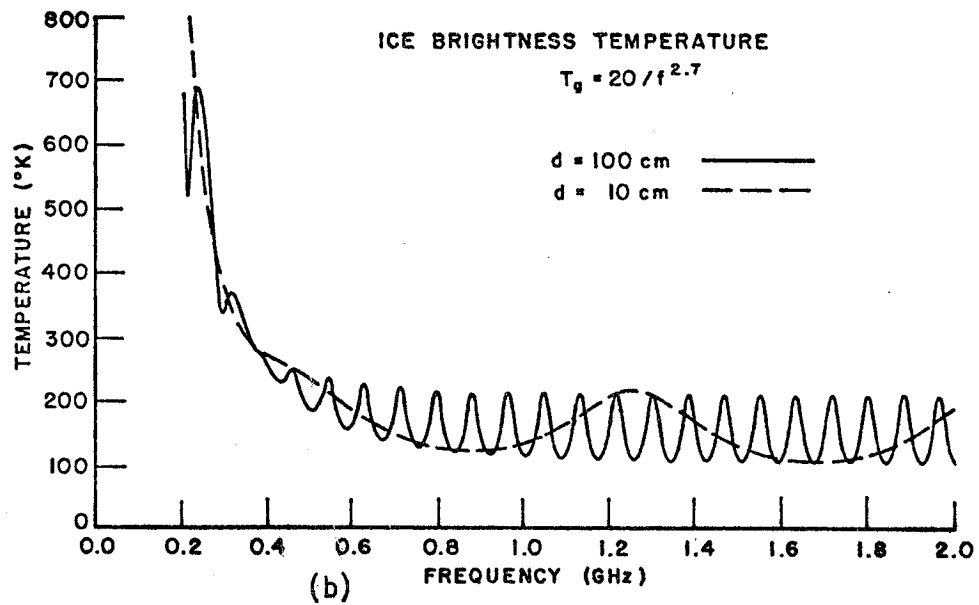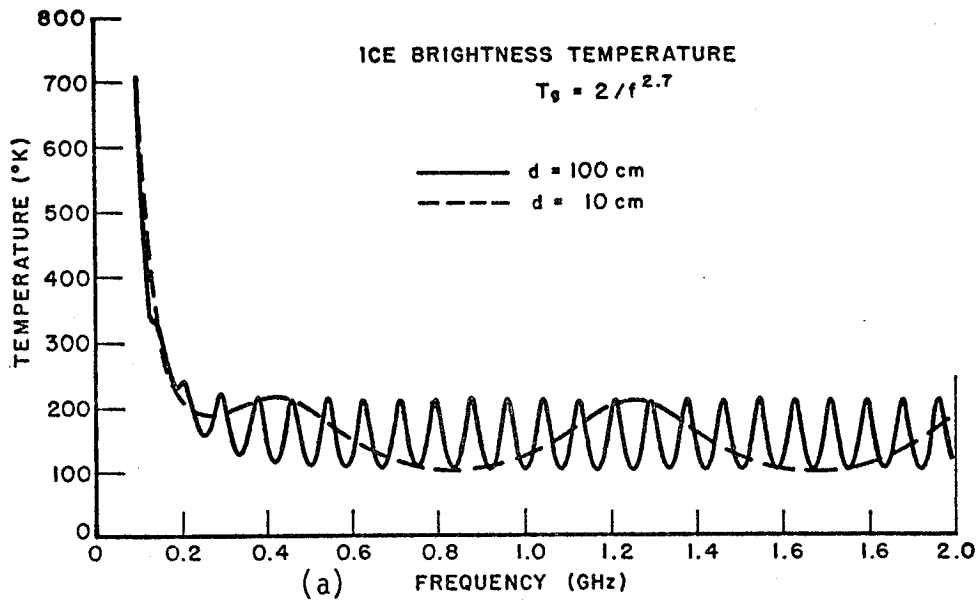
Figure 9. The apparent brightness temperature of the ice layer as a function of frequency and magnitude of galactic temperature for two different ice thicknesses.

26

ICE BRIGHTNESS TEMPERATURE

$$T_g = 40/f^{2.7}$$

d = 100 cm ———

d = 10 cm — — —
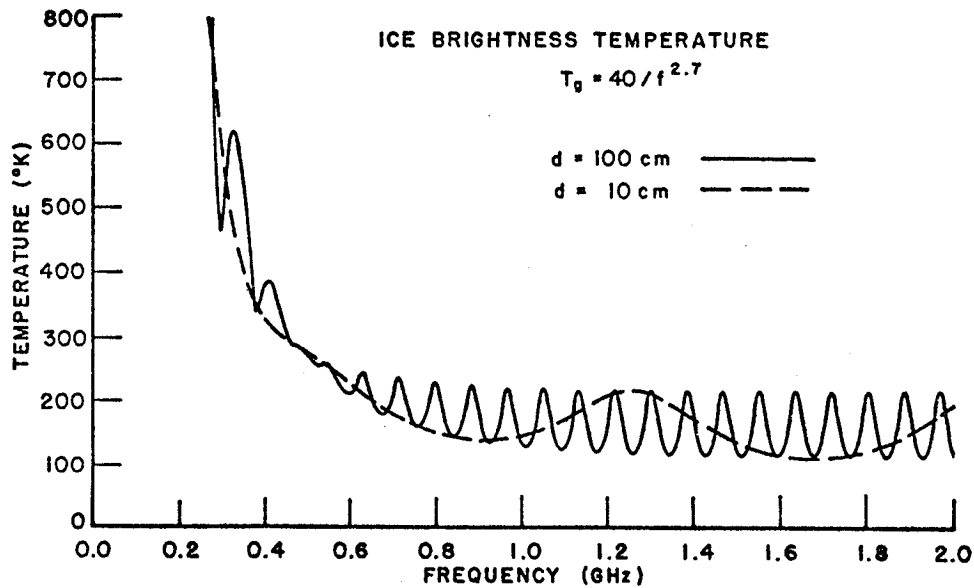
Figure 9 (c).   The apparent brightness temperature of the ice
layer as a function of frequency and magnitude
of galactic temperature for two different ice
thicknesses.

For low frequencies, the galactic temperatures are very
large, the reflection mechanism predominates, and the apparent
brightness temperature curves resemble in form those of the power
reflection coefficient. As frequency increases, the galactic temper-
ature decreases to the point where $T_g + T_a$ equals T_i (about 150 MHz
for small G), the sum of the emitted power and reflected power be-
comes constant, and the apparent brightness temperature becomes
independent of the power reflection coefficient, and hence of the
ice thickness d. At still higher frequencies, the emission clearly
dominates the reflection, and the character of the T_b versus d curves
is reversed. It can be seen from Figures 7 (a), (b), (c) and
Figures 9 (a), (b), and (c) that the frequency for which the
emissivity equals the reflectivity, is a function of the galactic
temperature T_g. At these "null" frequencies the apparent brightness
temperature is independent of ice thickness. Clearly frequencies
in the range 100 - 300 MHz are unsuitable for a general purpose
instrument, because the reflected cosmic noise contribution depends
strongly on the position of the galactic plane relative to the
reflected beam.

CHAPTER IV

APPARENT BRIGHTNESS MODEL GENERALIZATIONS

0. Introduction

The theory for calculating the apparent brightness temperature of a layered medium at normal incidence was reviewed in the previous chapter. Since the major advantage of the radiometer over active systems is the ability to scan, it is now desirable to include the effects of look angle and polarization. The model is also generalized to include the effects of temperature gradients in the ice. In the natural state, there may also be transition layers such as snow, slush, or water on top of the ice layer. In addition, natural ice will have some texture on the top surface and may also exhibit significant thickness variations. Such ice will also have losses greater than those predicted by Equation (3-4), due to air inclusions, etc.. The effect of these conditions on the apparent brightness temperature will be calculated in this chapter.

1. Variation with Look Angle and Polarization

If there existed only a single interface between two media, the reflection coefficient as a function of scan angle would be given by the well-known Fresnel reflection coefficients. When there are one or more homogeneous layers, the reflection and emission coefficients take a more complex form. Although, closed form solutions may be easily found for the single layer case, it is more convenient to approach the problem by use of an iterative procedure described by Richmond (1965). This procedure can handle any number of layers, and so it will be useful for approximating the effects of temperature gradients in the ice. The geometry of the problem is shown in Figure 10. Each layer has thickness d_n, uniform thermometer temperature T_n, and relative complex electric and magnetic permittivities ϵ_n and μ_n. Consider a plane wave incident from the direction θ. For horizontal polarization,

$$\bar{E}_{inc} = A_h \, i_x \, e^{(jky \sin \theta + jkz \cos \theta)} \tag{4-1}$$

where A_h is the incident electric field strength. In each layer, the appropriate fields may be written
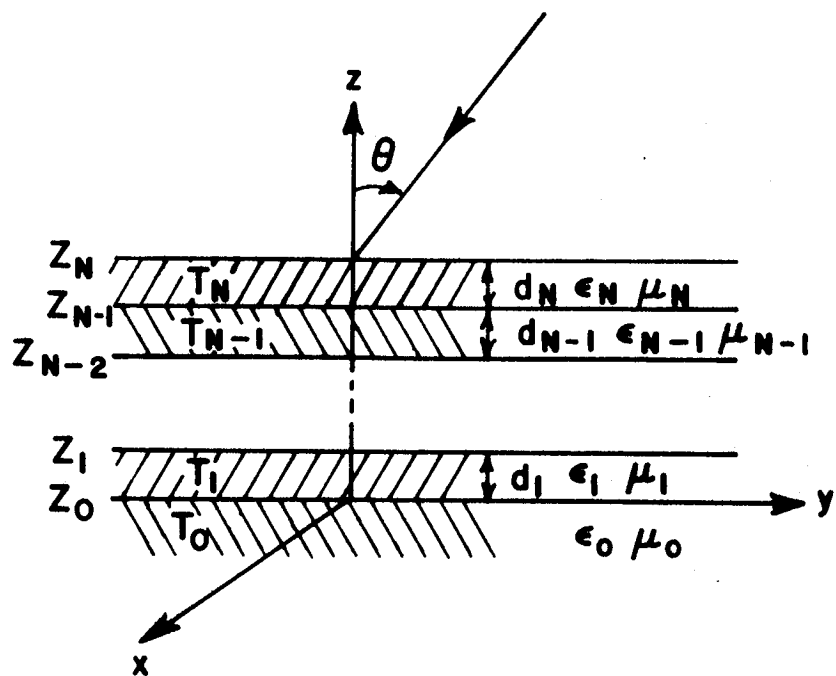
Figure 10. Geometry for modeling temperature gradients in the ice layer.

$$E_n^x = (A_n e^{\gamma_n z} + B_n e^{-\gamma_n z}) \, e^{(jky \sin\theta)} \qquad (4\text{-}2)$$

$$H_n^y = (-\gamma_n / jkZ_o \mu_n)(A_n e^{\gamma_n z} - B_n e^{-\gamma_n z}) e^{(jky \sin\theta)} \qquad (4\text{-}3)$$

where

$$Z_o = (\mu_o / \varepsilon_o)^{1/2} \qquad (4\text{-}4a)$$

$$\gamma_n = jk(\mu_n \varepsilon_n - \sin^2\theta)^{1/2} \quad . \qquad (4\text{-}4b)$$

By enforcing boundary conditions, the coefficients of the $n + 1^{st}$ layer can be found, Richmond (1965), from those of the layer below it.

$$A_{n+1} = P_n A_n + Q_n B_n \qquad (4\text{-}5a)$$

$$B_{n+1} = R_n A_n + S_n B_n \qquad (4\text{-}5b)$$

where

$$P_n = (.5)(1 + \rho_n) e^{(\gamma_n - \gamma_{n+1}) z_n} \qquad (4\text{-}6a)$$

$$Q_n = (.5)(1 - \rho_n) e^{(-\gamma_n - \gamma_{n+1}) z_n} \qquad (4\text{-}6b)$$

$$R_n = (.5)(1 - \rho_n) e^{(\gamma_n + \gamma_{n+1}) z_n} \qquad (4\text{-}6c)$$

$$S_n = (.5)(1 + \rho_n) e^{(-\gamma_n + \gamma_{n+1}) z_n} \qquad (4\text{-}6d)$$

$$\rho_n = (\mu_{n+1} \gamma_n) / (\mu_n \gamma_{n+1}) \quad . \qquad (4\text{-}6e)$$

The lower half space is assumed to extend to $-\infty$, and therefore $B_o = 0$. Setting $A_o = 1.$ and applying the recursion relations yields A_{n+1} and B_{n+1}. The power reflection coefficient is then given by

$$|R_h|^2 = |B_{n+1}/A_{n+1}|^2 \quad . \qquad (4\text{-}7)$$

For the case of vertical polarization, the results are identical except that now the fields are found from an assumed incident magnetic field

$$\bar{H}_{inc} = A_v \, i_x \, e^{(jky \sin \theta + jkz \cos \theta)} \tag{4-8}$$

with the fields in the nth layer being

$$H_n^x = (A_n e^{\gamma_n z} + B_n e^{-\gamma_n z})e^{(jky \sin\theta)} \tag{4-9}$$

$$E_n^y = (\gamma_n Z_0/jk \, \varepsilon_n)(A_n e^{\gamma_n z} - B_n e^{-\gamma_n z}) \, e^{(jky \sin\theta)} \tag{4-10}$$

where now

$$\rho_n = (\varepsilon_{n+1} \gamma_n)/(\varepsilon_n \gamma_{n+1}) \tag{4-11}$$

and

$$|R_v|^2 = |B_{n+1}/A_{n+1}|^2 \quad . \tag{4-12}$$

The variation of the power reflection coefficient with angle of incidence and polarization is shown in Figures 11 and 12. Vertical polarization clearly exhibits a Brewster angle phenomenon which causes a reduction in the dependence of the apparent brightness temperature on the ice layer thickness at a certain scan angle. These changes in the magnitude of the oscillation of the reflection coefficient with look angle, which may have an undesirable effect on certain thickness estimation systems, may be compensated for by utilizing circular or 45° linear polarization. In these cases, assuming that the horizontal and vertical components of the sky and cosmic noise are uncorrelated, the effective power reflection coefficient is given by $(|R_h|^2 + |R_v|^2)/2$. As $|R_v|^2$ decreases with increasing θ, so $|R_h|^2$ increases, and the average of the two shows very little variation with θ. A plot of the power reflection coefficient for circular polarization is given in Figure 13.
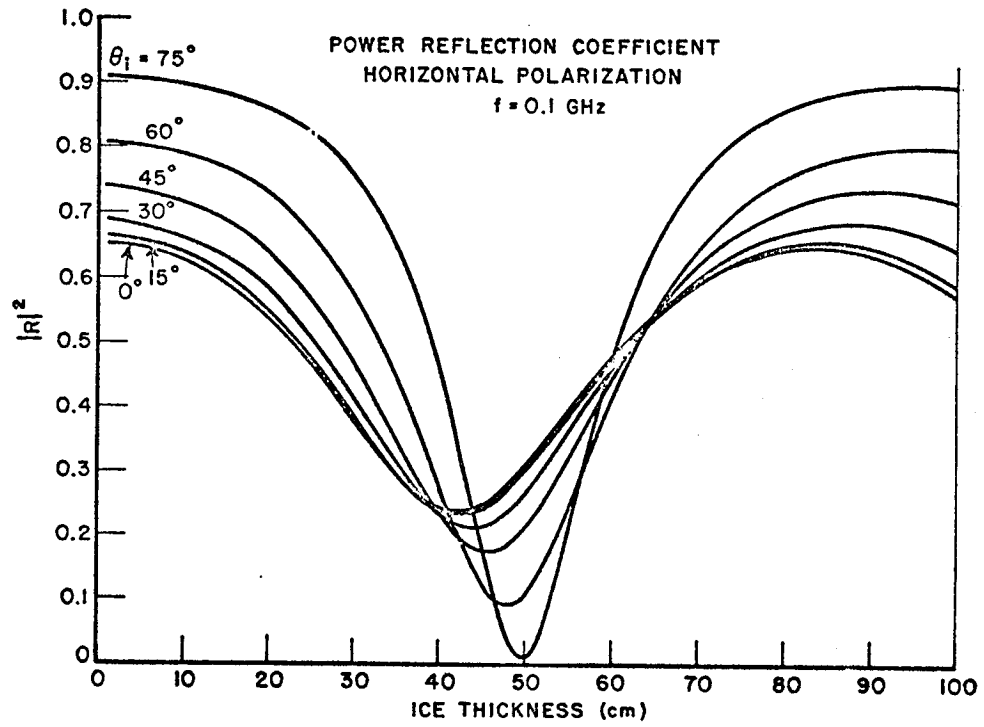
Figure 11. The power reflection coefficient as a function of aspect angle and ice layer thickness for horizontal polarization.

32

POWER REFLECTION COEFFICIENT
VERTICAL POLARIZATION
f = 0.1 GHz
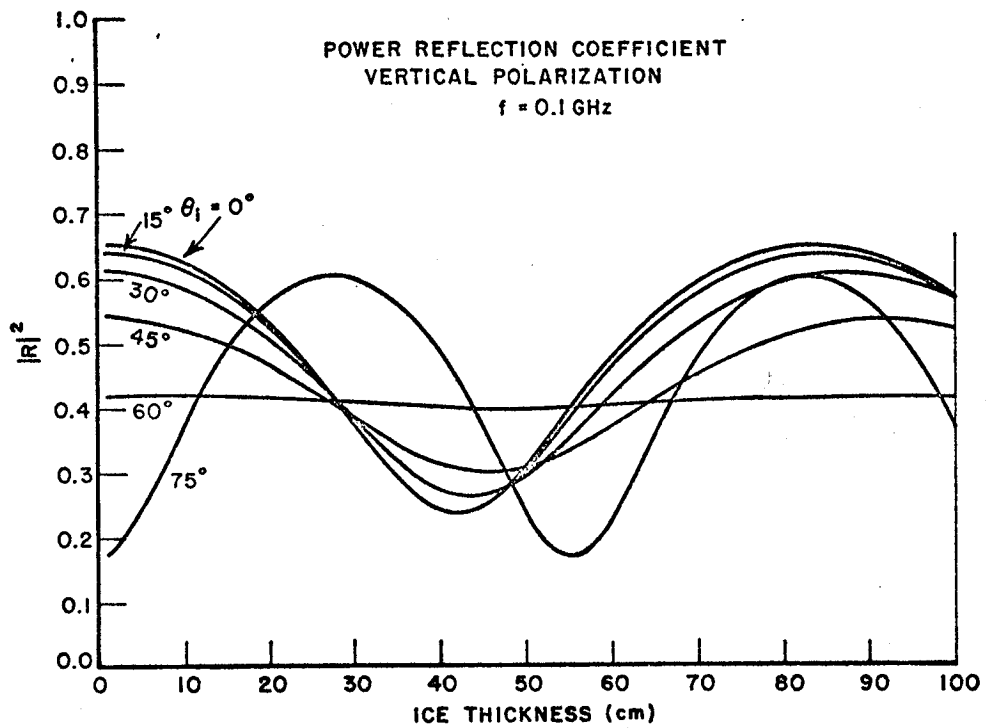
Figure 12. The power reflection coefficient as a function of aspect angle and ice layer thickness for vertical polarization.

33
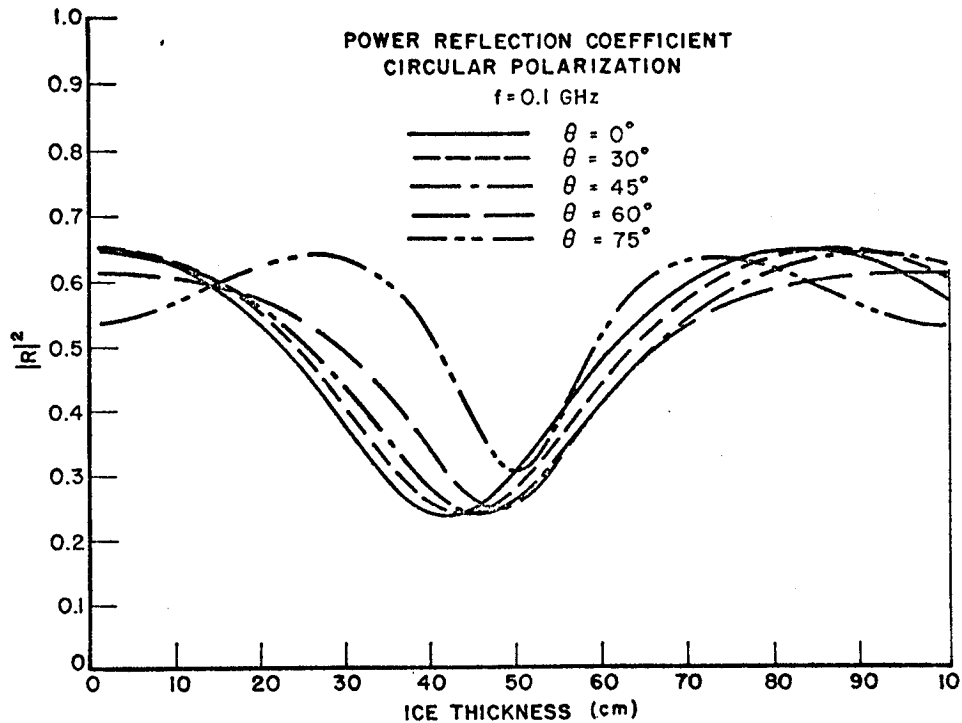
Figure 13. The power reflection coefficient as a function of
aspect angle and ice layer thickness for
circular polarization.

As a check of the foregoing iterative procedure, the complex
voltage reflection coefficient versus frequency was transformed
to the time domain using a numerical FFT routine. (To avoid
computational difficulties inherent in a true impulse response,
the reflection coefficient spectrum was multiplied by the
spectrum of very narrow raised cosine pulse.) Figure 14 shows
the response of a 100 cm ice layer to excitation by a pulse of
unit amplitude at normal incidence. The spacing between the
successive pulses just corresponds to the two-way travel time
through the ice slab and their magnitudes to the "air-ice",
"ice-water", etc., voltage reflection coefficients.

Although, the motivation for this work has been to solve the
problem of an ice layer over water, the procedure is completely
general. Any inhomogeneous, lossy, dispersive, planar medium can
be handled at any incidence angle or polarization. Although,
analytic expressions for the reflection and transmission coefficient
of certain graded dielectrics are known, the piecewise linear
approximation has been found to be superior computationally,
Sivaprasad (1976). Furthermore, the response to any time domain

34
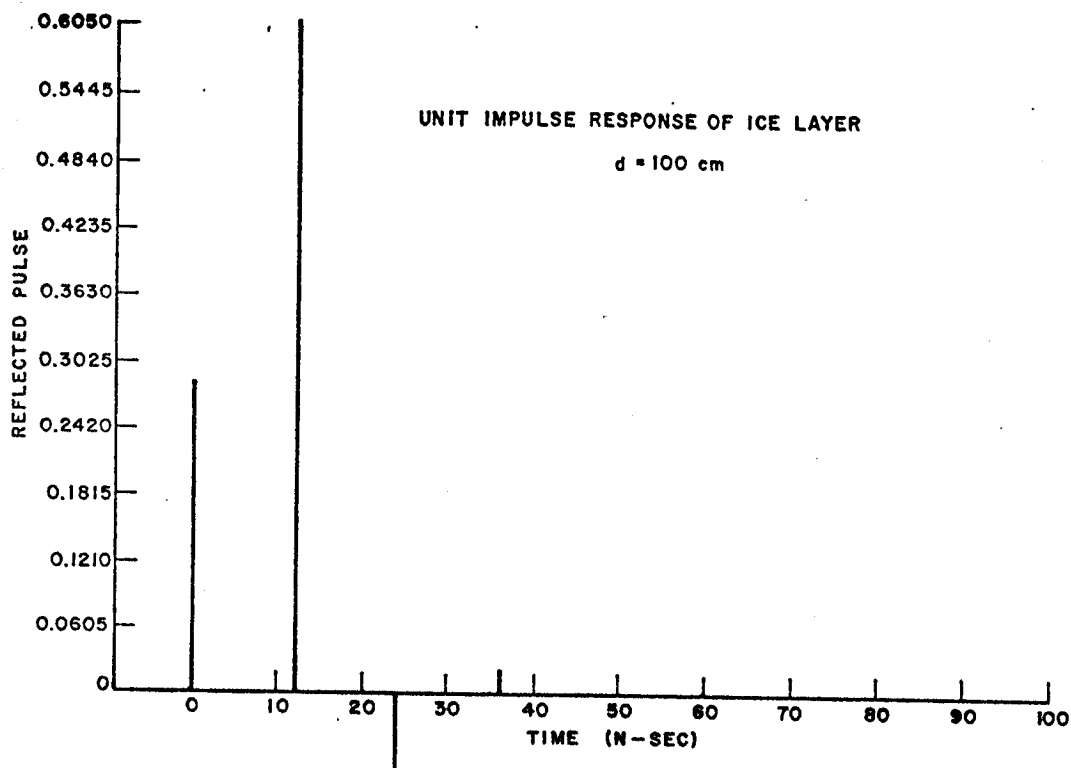
Figure 14. Normalized ice layer response to narrow unit pulse
excitation.

excitation can be obtained by simply multiplying the excitation
spectrum by the complex reflection coefficient and transforming
the product to the time domain. The response of several different
types of media for a wide sine squared pulse excitation has been
calculated by Simpson (1976).

2. Temperature Gradient in Ice

On cold days, with the air temperature well below freezing,
a physical temperature gradient will exist in the ice layer. For
this case, the numerical procedure given in the preceding section
can be extended to calculate the apparent brightness temperature
by utilizing a form of reciprocity principle. This asserts that
if a plane wave were incident on a surface from direction θ, and
if a fraction F of the total incident power were absorbed in a
certain layer having the physical temperature T, then the contri-
bution of that layer to the total brightness temperature of
radiation leaving the surface in the direction θ would be FT.

The brightness temperature of a medium composed of uniform layers is then

$$T_b = \sum_{n=0}^{N} F_n T_n + |R|^2 (T_g + T_a) \qquad \text{(4-13)}$$

where

$$F_n = (P_n - P_{n-1})/P_{inc}$$

is the fraction of the power in a hypothetical incident plane wave absorbed in the nth layer, and P_n is the net power incident on the nth layer.

For horizontal polarization,

$$P_n = Re(- E_n^X H_n^{y*})_{z=z_n} \qquad \text{(4-14)}$$

$$P_{inc} = A_{n+1} A_{n+1}{}^* \cos\theta /Z_0 \qquad . \qquad \text{(4-15)}$$

For vertical polarization,

$$P_n = Re(E_n^y H_n^{X*})_{z=z_n} \qquad \text{(4-16)}$$

$$P_{inc} = A_{n+1} A_{n+1}{}^* \cos\theta \ Z_0 \qquad . \qquad \text{(4-17)}$$

To find how well a continuous, linear temperature gradient may be approximated by discrete, homogeneous layers, a number of cases were calculated. A typical result is shown in Table 1.

TABLE 1

Linear Temperature Gradient Approximation

No. of Layers	f=0.10GHz			f=0.40GHz		
	$\|R\|^2$	T_{be}	T_b	$\|R\|^2$	T_{be}	T_b
2	.30927	188.50	500.27	.35406	176.29	186.71
4	.30894	188.59	500.02	.34729	178.13	188.36
10	.30882	188.62	499.93	.34520	178.71	188.87
20	.30878	188.63	499.90	.34437	178.93	189.07
40	.30876	188.64	499.89	.34393	179.05	189.18
80	.30874	188.64	499.88	.34370	179.11	189.24
100	.30874	188.64	499.87	.34366	179.13	189.25
200	.30872	188.65	499.86	.34355	179.16	189.27

Total Ice Thickness = 50 cm
Air Temperature = -40°C
Water Temperature = 0°C
Normal Incidence
Galactic Temperature Factor G = 2.

The temperature profiles were chosen such that for example, in the case of four layer approximation, the top 12.5 cm of the ice was set to -40°C, the next 12.5 cm to -30°C, the next 12.5 cm to -20°C, and the bottom 12.5 cm was set to -10°C.

It is clear that for fresh water ice, for which the attenuation α does not change much with physical temperature, only a few homogeneous layers are needed to simulate a linear continuous temperature distribution in the ice layer. Because of the low thermal conductivity of ice, and the fact that the temperature distribution is controlled by a diffusion equation, a sudden change in the air temperature at the surface of the ice will produce an internal effect only after some considerable time, proportional to the square of the distance from the surface, Pounder (1965). It would take a number of days for a linear temperature gradient to be established in a 50 cm ice layer for example. The actual temperature gradient in the ice would then be approximately a linear one, reflecting the long term temperature conditions, with a daily variation confined to the top few centimeters of the ice layer. The mathematical model developed here can approximate any temperature gradient as accurately as desired, but as may be seen from Table 1, changes in the physical temperature of the ice have

negligible effect on the apparent brightness temperature. Thus, all subsequent calculations will assume a uniform ice temperature.

3. Snow on Top of Ice

In the natural state, it is quite possible that a snow cover may exist on top of the ice layer. Natural snow is very difficult to model accurately because of the great variation possible in the relative complex dielectric constant which is a function of the snow density and moisture content. Investigators report snow densities ranging in value from .06 gm/cc to .517 gm/cc, Yosida (1963), Kennedy (1966), Yoshino (1967), Meier (1971), Hoekstra (1972), Sackinger (1972), Vickers (1972). According to Cumming (1952), this span of densities for dry snow results in the permittivity ranging between 1.1 and 2.0, and the loss tangent (at $f = 9.375$ GHz, and 0°C) between .0003 and .0011. If the snow, however, contains as little as 1.6% water content (by weight), the loss tangent increases by a factor of 20. Von Hippel (1961) gives the loss tangent (at $f = 3$ GHz) of freshly fallen snow as .0009 and of hard-packed snow followed by light rain as .0029.

A typical calculation showing the effect of the snow layer on the ice is shown in Figures 15 (a) and 15 (b). If the snow is completely dry, it has very little loss and acts as an impedance matching layer. For certain frequency and thickness combinations, the dependence of the power reflection coefficient on the ice thickness completely vanishes. This can be seen for example in Figure 15 (a). In this instance, the reflection coefficient shows negligible dependence on the ice thickness for frequency of .3GHz and a 20 cm snow layer. If the snow, on the other hand, has some moisture, it will become more lossy. As the thickness of the moist snow increases, the total loss and the emissivity increase, and the ripple disappears. Thus, the variation in the apparent brightness temperature as a function of the ice layer thickness can be greatly reduced by either dry or wet snow. From Figure 15 (b), it can be seen that for wet snow the apparent brightness temperature will also greatly increase with increasing snow layer thickness. Even at higher frequencies (33.6 GHz), however, the snow cover is often sufficiently transparent that terrain features such as field patterns, roads, etc., are all readily identifiable under the snow cover, Moore (1974). Thus in practice, unless there is a fairly thick cover of wet snow, the variation of brightness with ice thickness should remain observable.

4. Water on Top of Ice

During periods of warm weather, some of the surface ice may melt forming a layer of water on top of the ice. Changes in

38
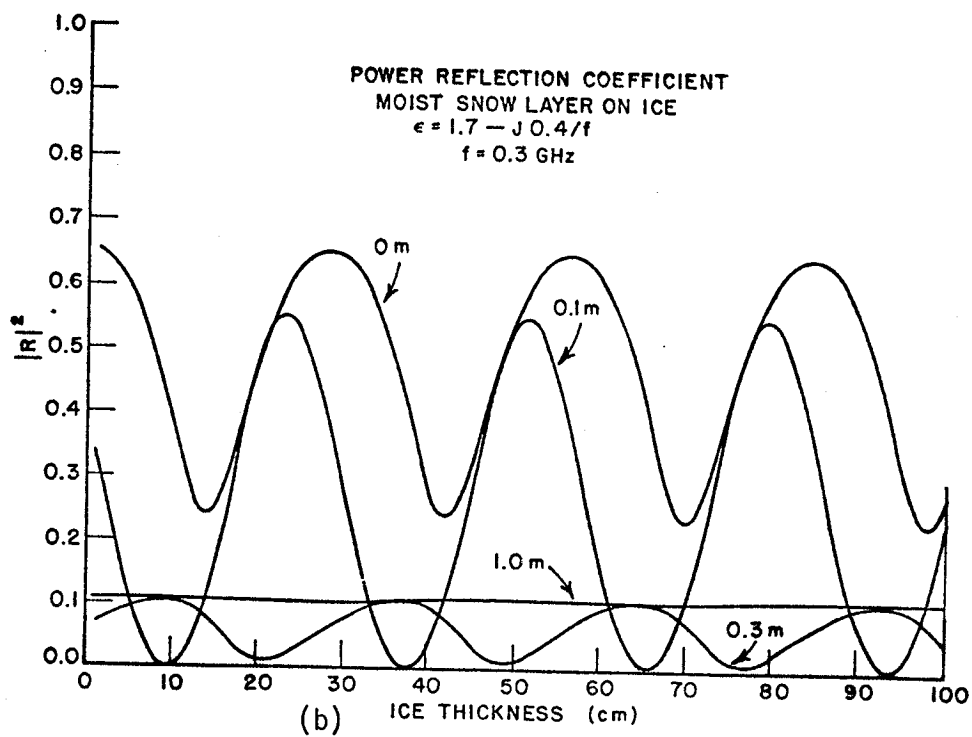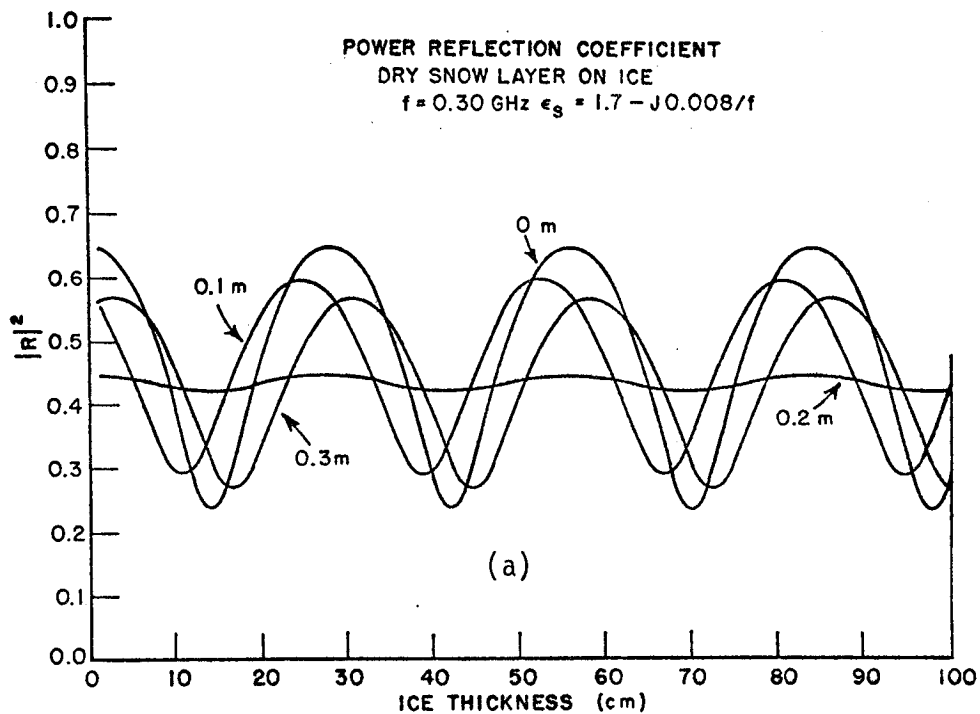
Figure 15. Changes in the power reflection coefficient due to a snow layer on top of the ice. Note, a quarter wavelength in dry snow is .19 meters.

power reflection coefficient with increasing water layer thickness are shown in Figures 16 (a), (b), and (c). It is clear that it may be possible to tolerate a millimeter or so of water on top of the ice without destroying the T_b versus d curve but not much more. The actual power absorbed in the water layer is not large as shown in Figures 17 (a), (b), (c), and Figures 18 (a), (b), (c), but the power reflection coefficient has changed drastically due to changes in the impedance match. The effects of a water layer on reflection coefficient at lower frequencies (300 MHz) are discussed in Smith (1972).

5. Slush on Top of Ice

During weather conditions producing alternate thawing and freezing, it is possible that a layer of slush may form on top of the ice layer. For lack of published data on the dielectric constant for such a layer, recourse must be made to mixture formulas for slush modeling.
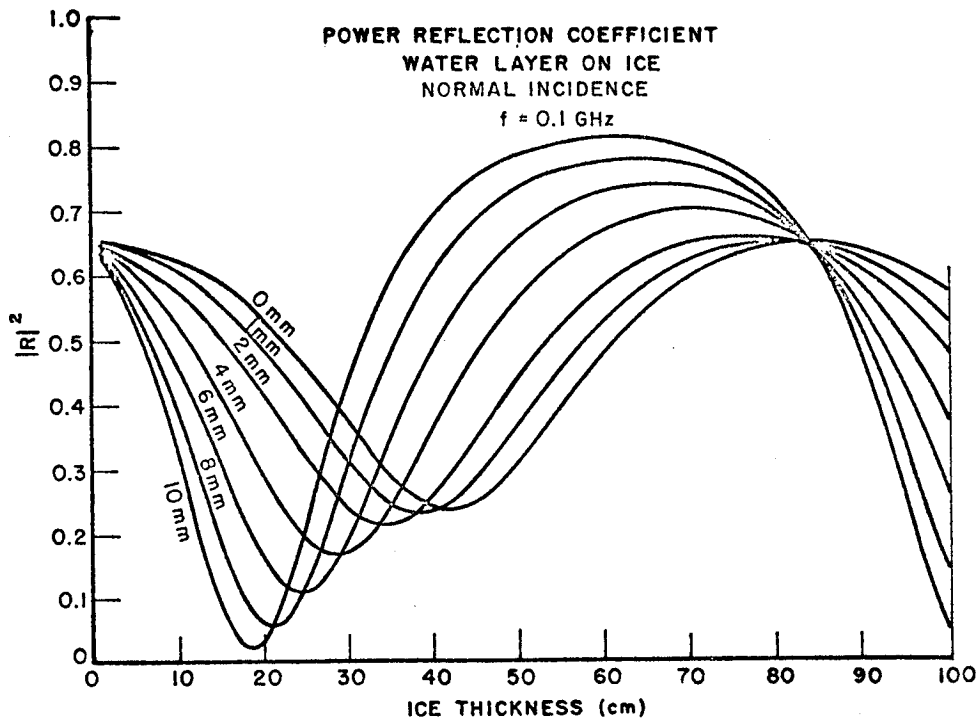
Figure 16 (a). Changes in the power reflection coefficient due to a water layer on top of the ice.
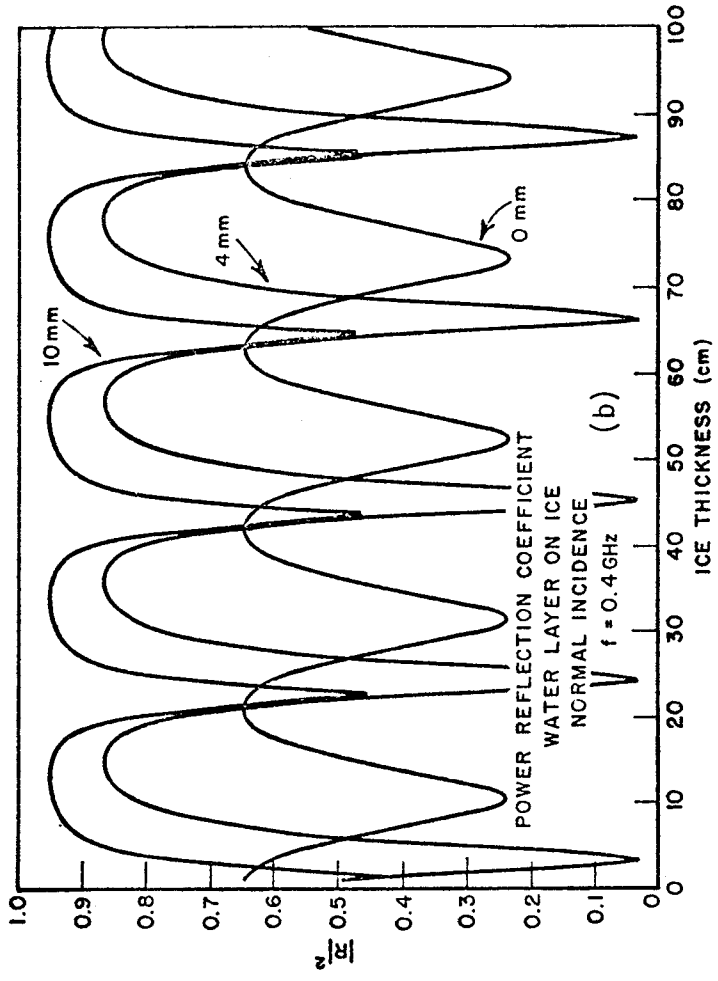
Figure 16 (b). Changes in the power reflection coefficient due to a water layer on top of the ice.

41
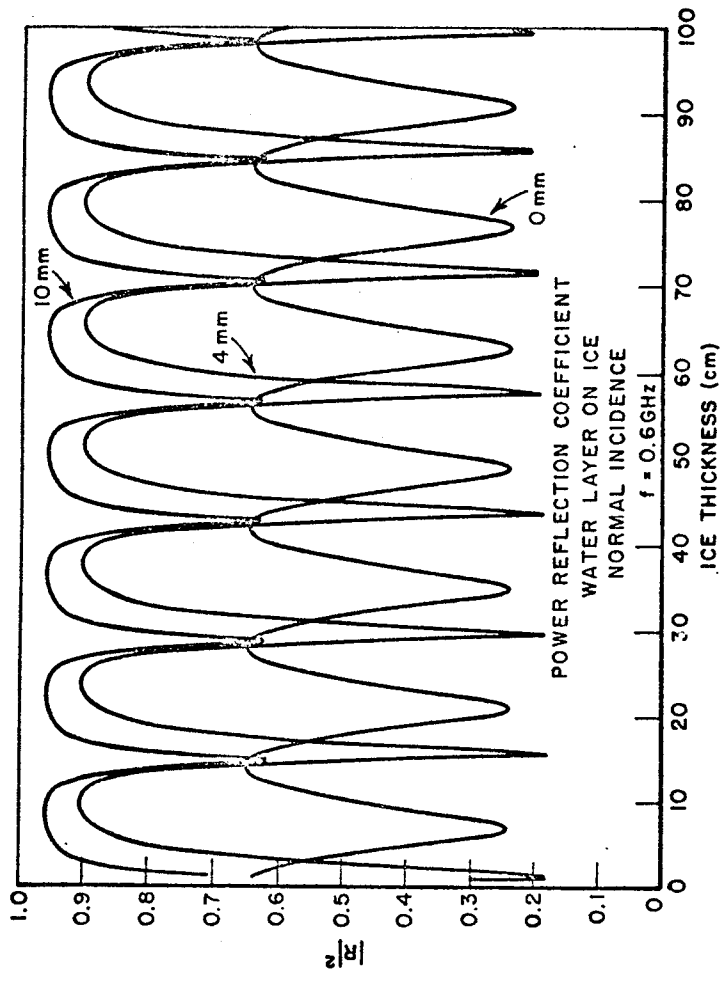
Figure 16 (c). Changes in the power reflection coefficient
due to a water layer on top of the ice.
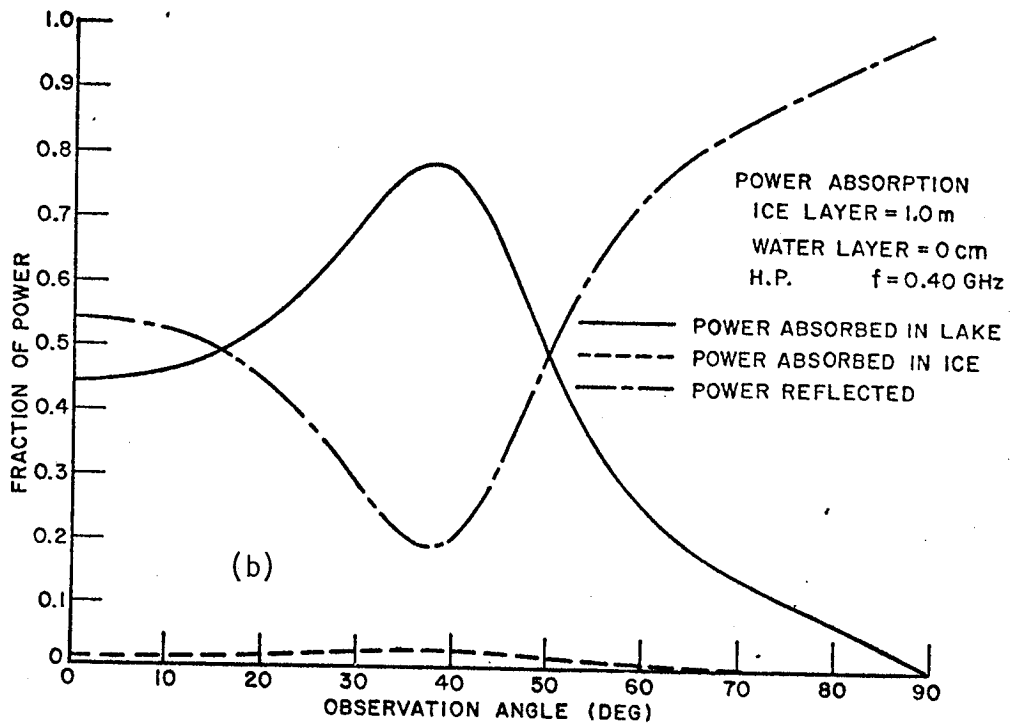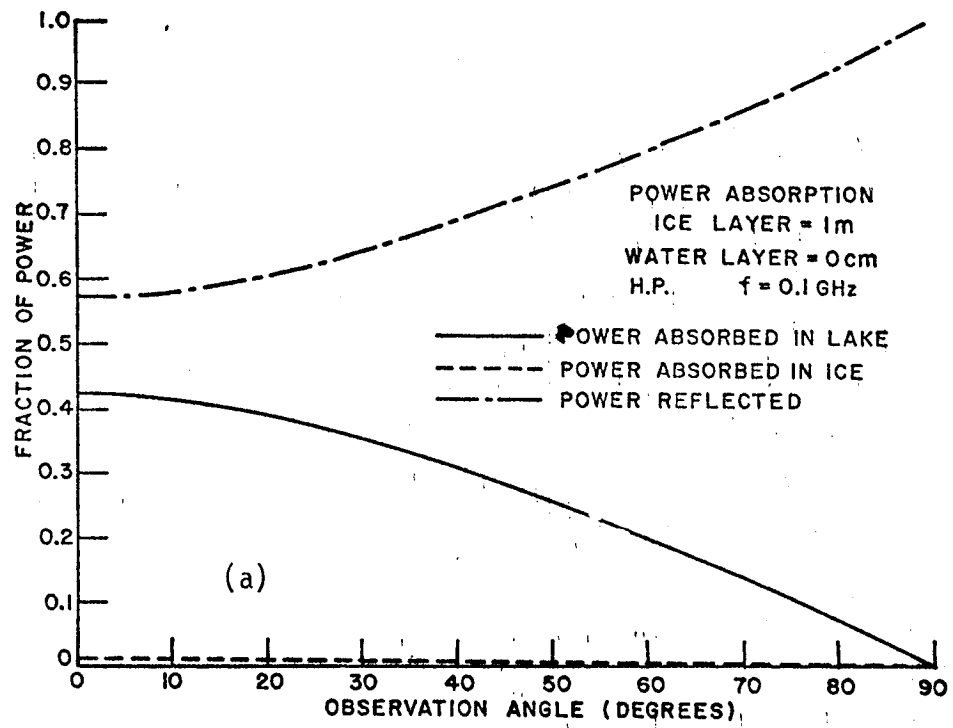
Figure 17 (a-b). Power absorption in the ice/water system as a
function of aspect angle, assuming no water
layer on top of the ice.

43
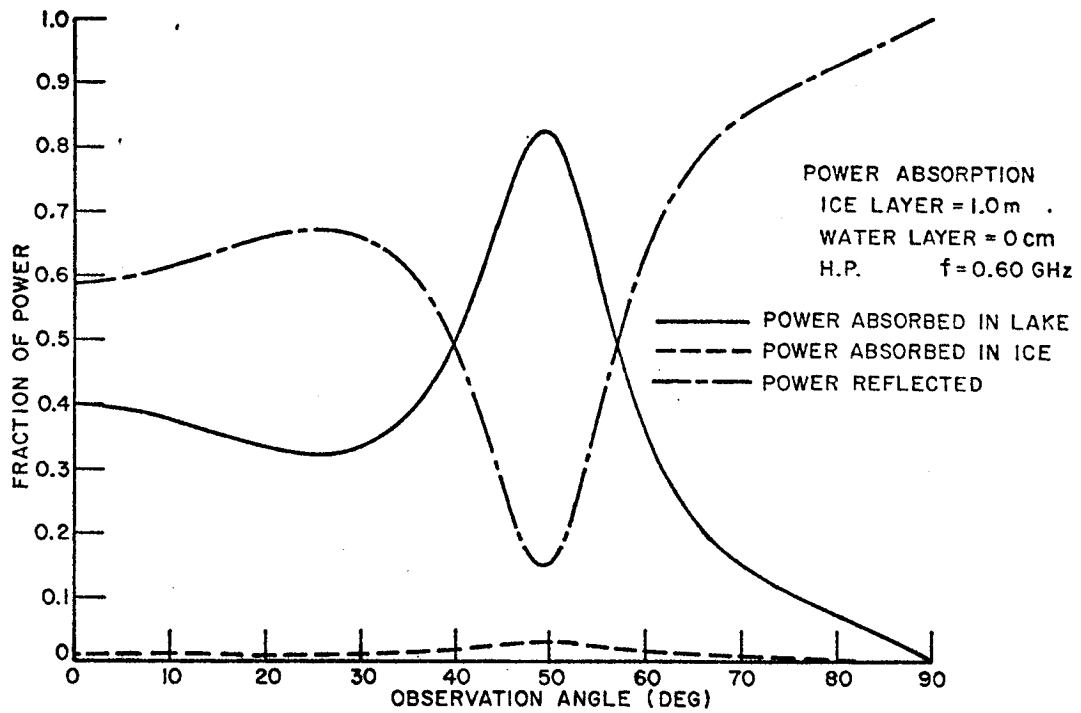
Figure 17 (c). Power absorption in the ice/water system as a function of aspect angle, assuming no water layer on top of the ice.
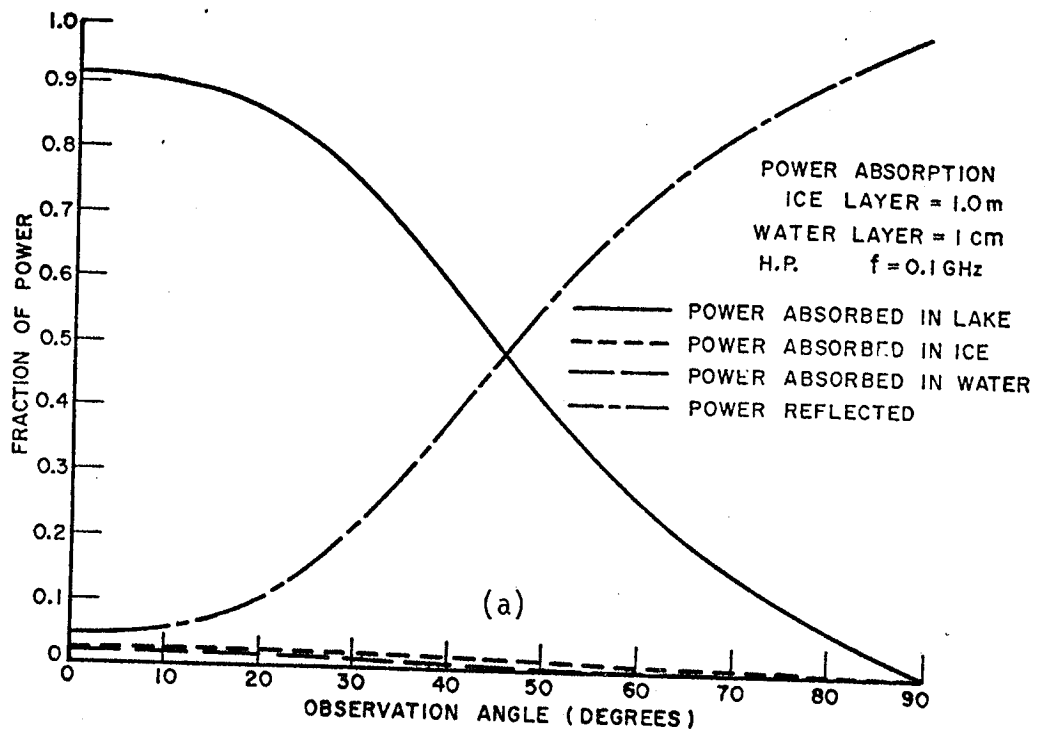
Figures 18 (a-b). Power absorption in the ice/water system as a function of aspect angle, assuming a water layer on top of the ice.
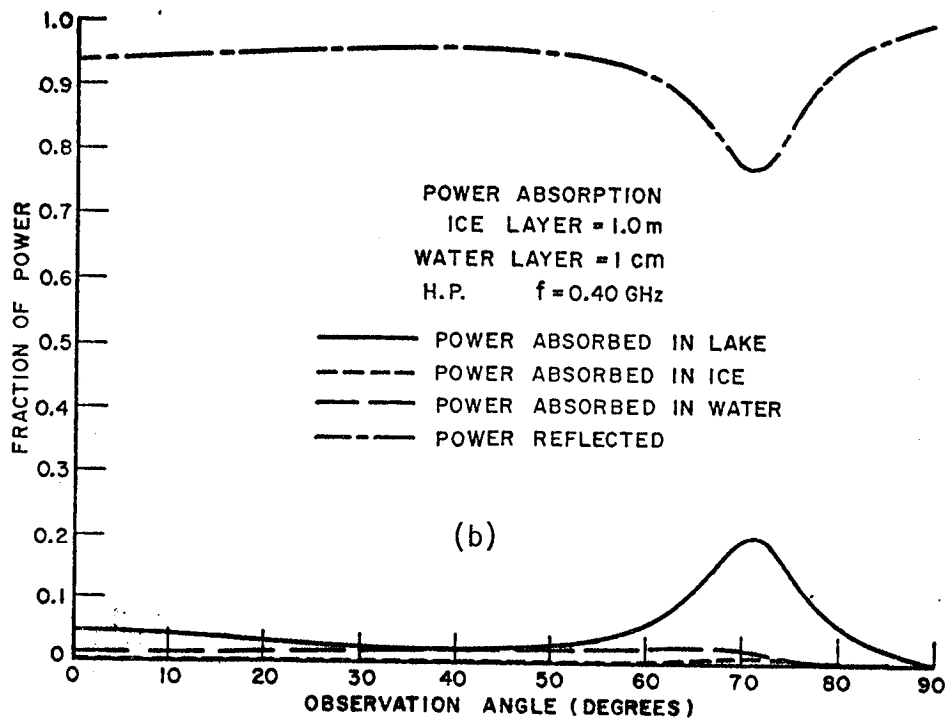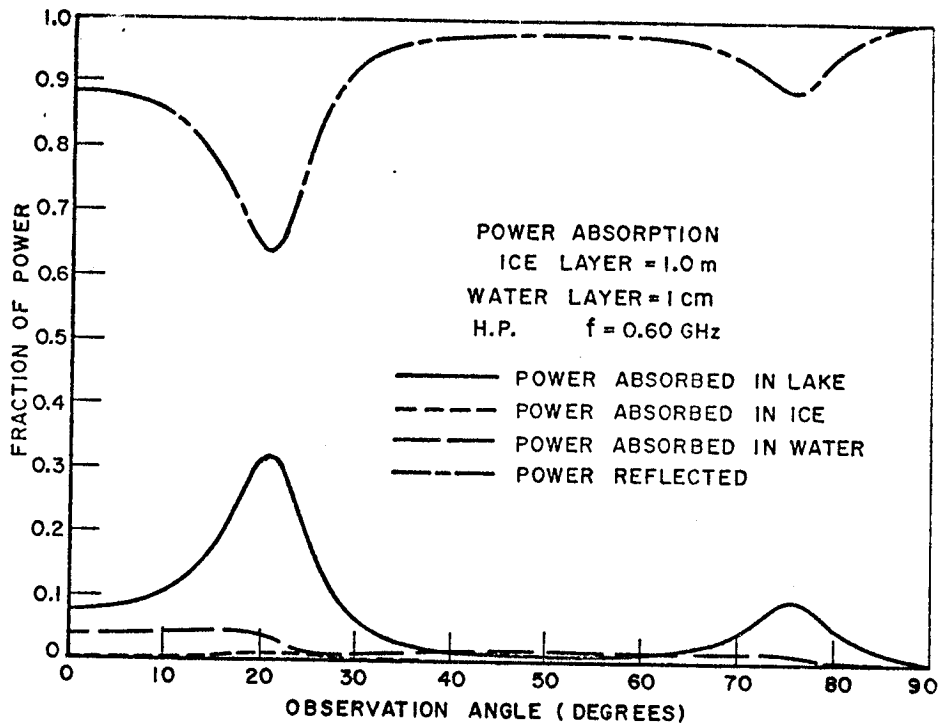
Figure 18 (c). Power absorption in the ice/water system as a
function of aspect angle, assuming a water
layer on top of the ice.

A number of mixture formulas have been derived, but those with
an adjustable parameter, called the form number, offer the greatest
flexibility in describing effects such as particle shape, size,
orientation, distribution, etc.. One such formula is due to Weiner,
Evans (1965)

$$\frac{\varepsilon_m - 1}{\varepsilon_m + u} = \frac{p(\varepsilon_1 - 1)}{\varepsilon_1 + u} + \frac{(1 - p)(\varepsilon_2 - 1)}{\varepsilon_2 + u} \qquad (4\text{-}18)$$

where

ε_m is the relative complex dielectric constant of the mixture

ε_1, ε_2 are the relative complex dielectric constants of the
two mixture components

p is the fraction of mixture volume occupied by component 1

u is the form number $(o < u < \infty)$.

If the two components are thoroughly mixed, or if one component in the form of chunks is suspended in the other (such as small pieces of ice floating in water), then u is on the order of 10. If the two mixture components are in the form of interleaved layers, then the form number takes its limiting value. u approaches zero if the layer boundaries are oriented orthogonal to the propagation direction of the incident field and approaches infinity if the layer structure is parallel (i.e., in the latter case, the field does not cross the boundaries between the two constituents, Evans (1965)).

The relative complex dielectric constants of water and ice given in the previous sections were substituted in Equation (4-18) to calculate possible values of the dielectric constant of slush. The real and imaginary parts of the water-ice mixture dielectric constant for various form numbers are shown in Figures 19 (a) and (b). An equal volume occupancy by the two constituents has been assumed in this calculation. The great variation in dielectric constant possible for a given volume occupancy and the possibility of any fractional composition indicates the difficulty in realistic modeling of the actual slush found in the natural state.

The variation of the power reflection coefficient with increasing slush layer thickness was calculated using a representative value of p = .5 and u = 10 in the mixture formula. This choice of percentage volume occupancy and of form number gives the relative complex dielectric constant values listed in Table 2.

TABLE 2

Water-Ice Mixture Dielectric Constant Values

f(GHz)	$Re(\epsilon_{wi})$	$Im(\epsilon_{wi})$
0.1	13.274	-0.0406
0.2	13.274	-0.0595
0.3	13.274	-0.0831
0.4	13.273	-0.1079
0.5	13.272	-0.1333
0.6	13.272	-0.1589

The change in the power reflection coefficient with increasing slush layer thickness is shown in Figures 20 (a) and (b). It is clear that a few centimeters of slush on top of the ice would seriously affect most data processing methods that rely on the shape of the power reflection coefficient. It should be noted that because the actual properties of the slush layer are not known, calculations such as this one can be considered only as an indication of the true behavior of the surface.
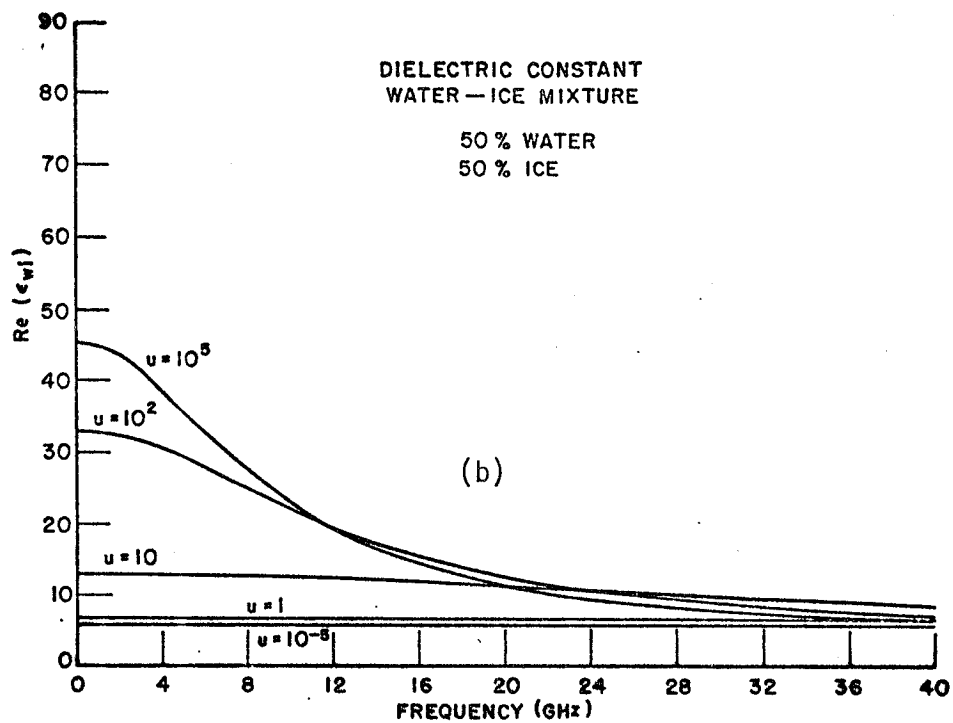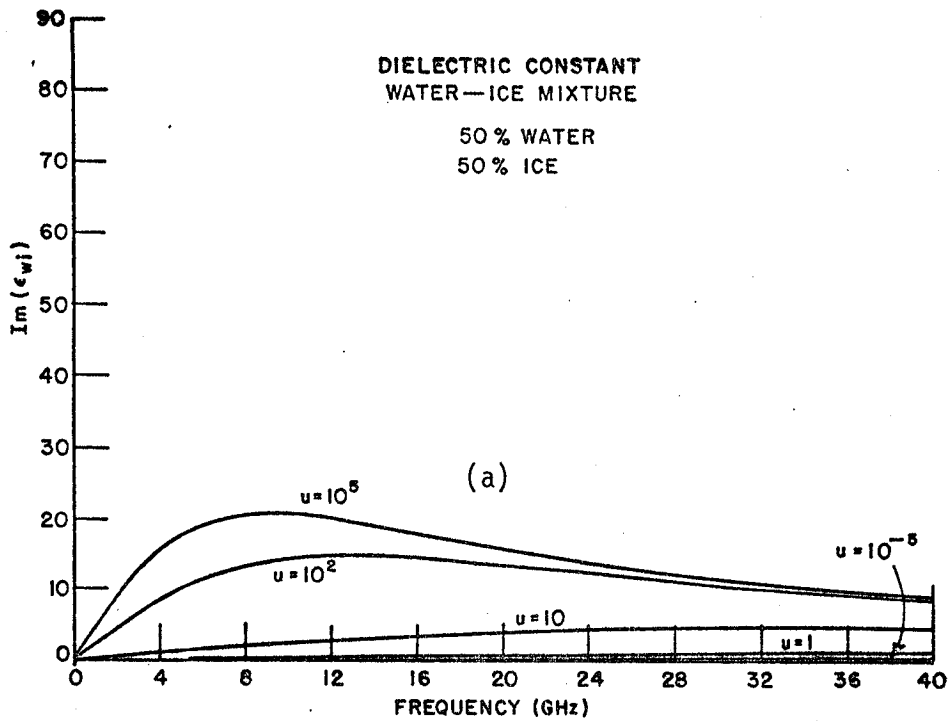
Figures 19 (a-b). The relative complex dielectric constant of
a water-ice mixture as a function of
frequency and form number.

48
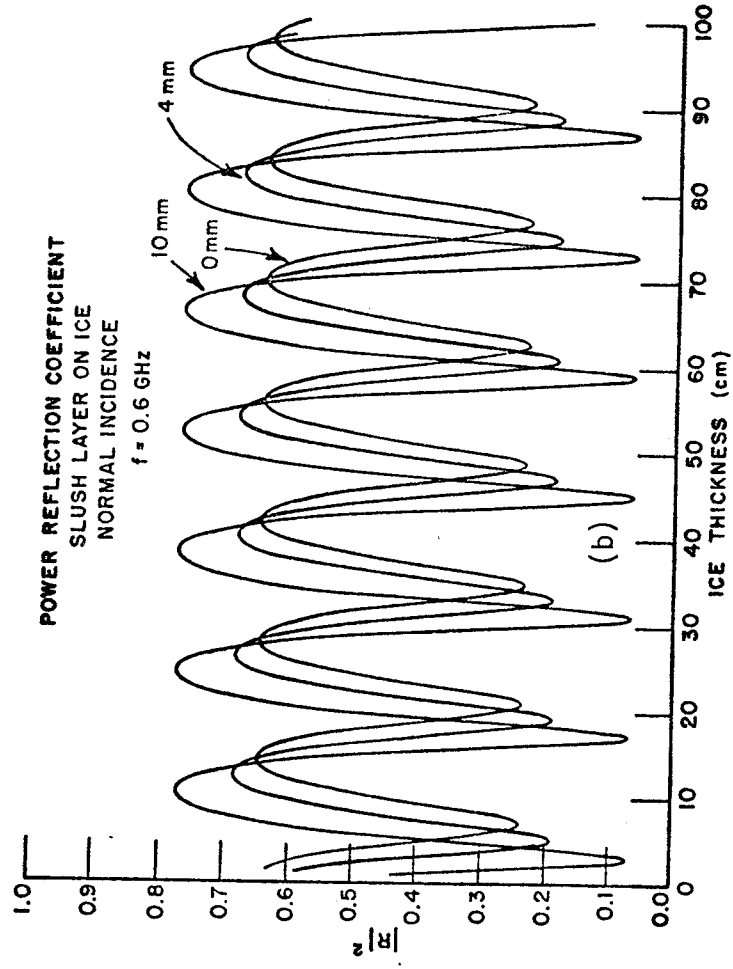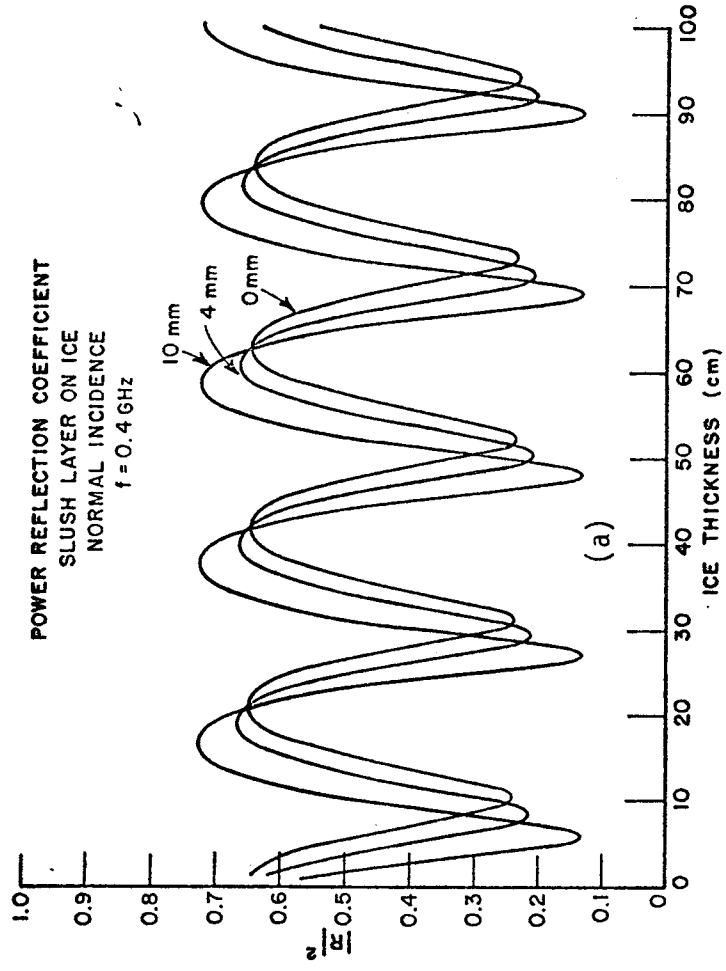
Figures 20 (a-b). Changes in the power reflection coefficient
as a function of slush layer thickness on
top of the ice.

6. Slush Between Water and Ice

It may also happen that a mixed layer of water and ice exists on the bottom surface of the ice slab, though that is not usually the case for a fresh water ice system. The same values as in the previous section were used to model the relative complex dielectric constant of the slush layer. The power reflection coefficient of the ice layer-slush layer-water system were calculated for several different slush layer thicknesses and frequencies of 0.4 GHz and 0.6 GHz. These results are shown in Figures 21 (a) and (b). Two different effects can be seen here. At f=0.4 GHz the slush acts more like a resonant matching layer which reduces the oscillation in the reflection coefficient only at certain thicknesses (4 cm, for example). At .6 GHz, there appears to be a steady decline in the oscillation of the power reflection coefficient due to "smoothing out" of the ice-water boundary. Again, these calculations are useful only for indicating qualitative behavior due to the large variation possible in slush dielectric constant. As stated before, slush layers below the ice are not expected in fresh water.

7. Small Scale Surface Roughness

Any real ice surface found in the natural state will have some surface texture. The effect of this small scale surface roughness on a boundary between two media is to cause diffuse scattering in all directions at the expense of power in the specular direction. The order of power reduction in the specular direction is given by, Ruck (1970),

$$|R_i|^2 \, \varepsilon^{-(2kh\cos\theta)^2} \tag{4-19}$$

where

h is the RMS surface roughness height

θ is the angle of incidence

k is the propagation constant in air

R_i is the reflection coefficient (air-ice)   .

The exponential factor is plotted in Figure 22. Usually the criterion $h/\lambda \leq .04$ defines a "slightly rough surface." Thus, for frequencies around 1 GHz for example, the RMS surface roughness height should be less than 1.2 cm for Equation (4-19) to be valid.

50
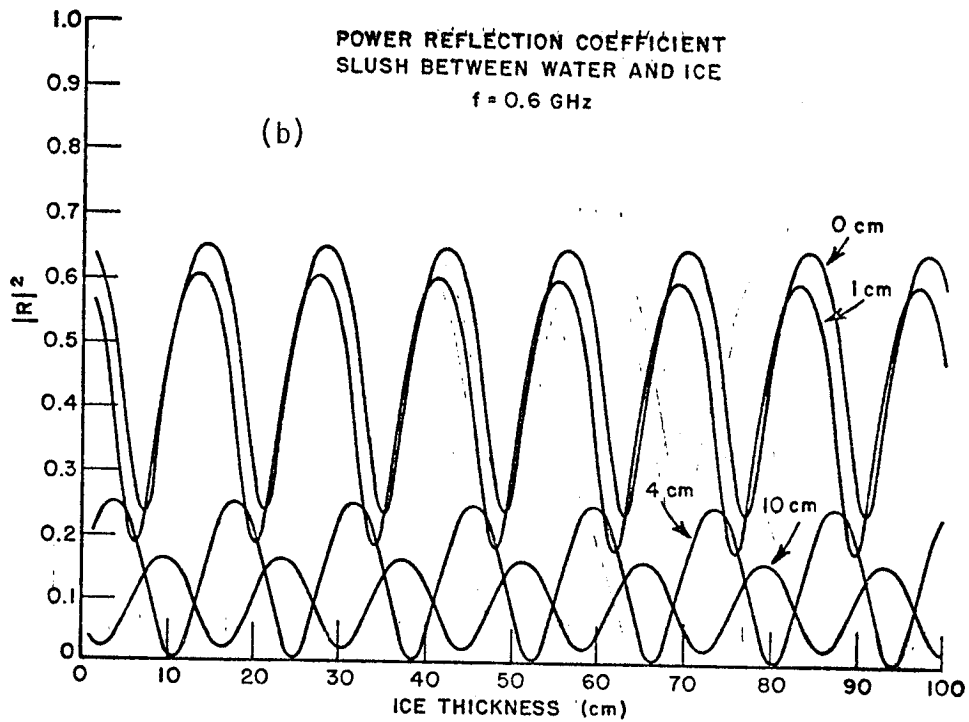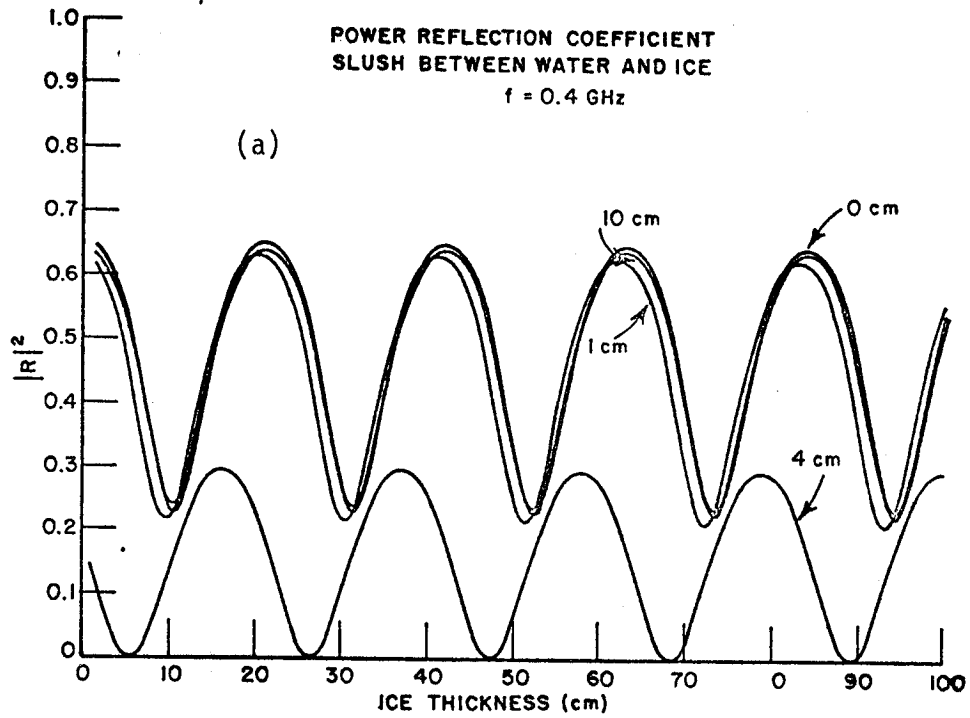
Figures 21 (a-b). Changes in the power reflection coefficient as a function of slush layer thickness between the water and the ice.

51
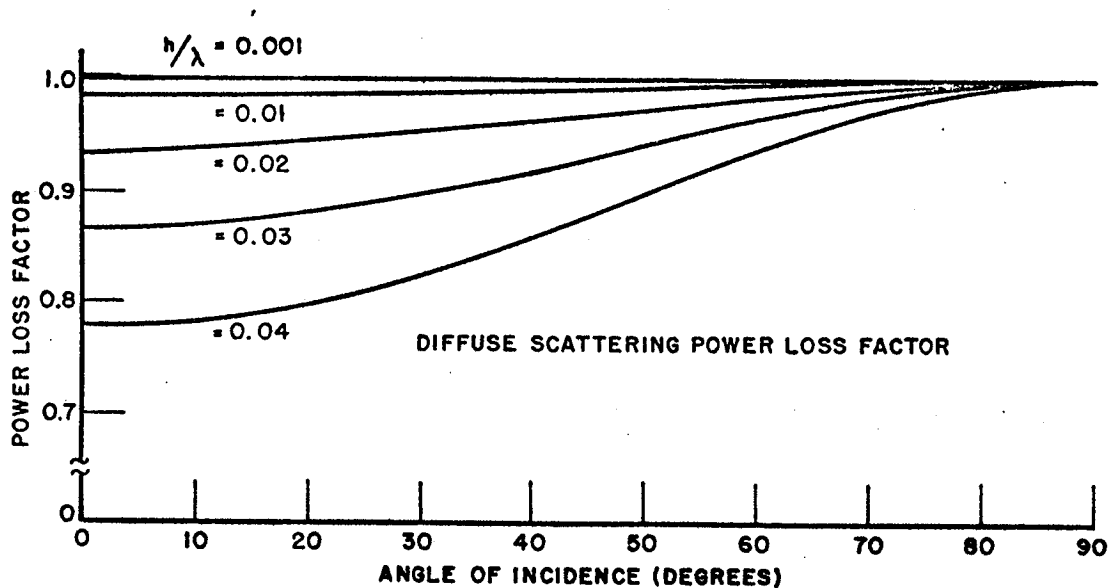
Figure 22. The reduction of the specular power reflection coefficient $|R_i|^2$, due to slight surface roughness.

The fraction of incident power scattered diffusely from a slightly rough surface may be calculated more precisely using the differential incoherent scattering cross-sections σ_{jk} (o,s) and σ_{jj}(o,s), Ruck (1970) and Peake (1971). Consider power density I_o incident on an area A at an angle θ_i. The total incident power P_i is then

$$P_i = I_o \, A \, \cos \theta_i \qquad .\tag{4-20}$$

The power density scattered from A at a distance R is

$$I_s = \frac{I_o \, A \, [\sigma_{jk} \, (o,s) + \sigma_{jj} \, (o,s)]}{4\pi \; R^2}\tag{4-21}$$

and the total scattered diffuse power is

$$P_s = \int_{\phi_s=0}^{2\pi} \int_{\theta_s=0}^{\pi/2} I_s \; R^2 \, \sin \theta_s \; d\theta_s \; d\phi_s\tag{4-22}$$

52

and

$$P_s = \frac{I_o A}{4\pi} \int\limits_{\phi_s=0}^{2\pi} \int\limits_{\theta_s=0}^{\pi/2} [\sigma_{jk} (o,s) + \sigma_{jj} (o,s)] \qquad (4\text{-}23)$$

$$\cdot \sin \theta_s \, d \theta_s \, d \phi_s \qquad .$$

The fraction of power scattered diffusely, F_d is then

$$F_d = \frac{1}{4\pi \cos\theta_o} \int\limits_{\phi_s=0}^{2\pi} \int\limits_{\theta_s=0}^{\pi/2} [\sigma_{jk} (o,s) + \sigma_{jj} (o,s)]$$

$$\cdot \sin \theta_s \, d \theta_s \, d \phi_s \qquad . \qquad (4\text{-}24)$$

For a slightly rough suface, the differential incoherent scattering cross-sections are given by Ruck (1970)

$$\sigma_{hn} (o,s) = \frac{4}{\pi} k^4 h^2 \cos^2 \theta_i \cos^2 \theta_s \, |\alpha_{hh}|^2 I \qquad (4\text{-}25)$$

$$\sigma_{hv} (o,s) = \frac{4}{\pi} k^4 h^2 \cos^2 \theta_i \cos^2 \theta_s \, |\alpha_{hv}|^2 I \qquad (4\text{-}26)$$

$$\sigma_{vh} (o,s) = \frac{4}{\pi} k^4 h^2 \cos^2 \theta_i \cos^2 \theta_s \, |\alpha_{vh}|^2 I \qquad (4\text{-}27)$$

$$\sigma_{vv} (o,s) = \frac{4}{\pi} k^4 h^2 \cos^2 \theta_i \cos^2 \theta_s \, |\alpha_{vv}|^2 I \qquad (4\text{-}28)$$

where

$$\alpha_{hh} = \frac{- (\epsilon_c - 1) \cos \phi_s}{(\cos \theta_i + \sqrt{\epsilon_c - \sin^2 \theta_i})(\cos \theta_s + \sqrt{\epsilon_c - \sin^2 \theta_s})}$$

$$(4\text{-}29)$$

$$\alpha_{hv} = \frac{- \sin \phi_s (\epsilon_c - 1) \sqrt{\epsilon_c - \sin^2 \theta_s}}{(\cos \theta_i + \sqrt{\epsilon_c - \sin^2 \theta_i})(\epsilon_c \cos \theta_s + \sqrt{\epsilon_c - \sin^2 \theta_s})}$$

$$(4\text{-}30)$$

53

$$\alpha_{vh} = \frac{\sin \phi_s \, (\varepsilon_c - 1) \, \sqrt{\varepsilon_c - \sin^2 \theta_i}}{(\varepsilon_c \cos \theta_i + \sqrt{\varepsilon_c - \sin^2 \theta_i})(\cos \theta_s + \sqrt{\varepsilon_c - \sin^2 \theta_s})}$$

$$(4\text{-}31)$$

$$\alpha_{vv} = \frac{(\varepsilon_c - 1)(\varepsilon_c \sin \theta_i \sin \theta_s - \cos \phi_s \sqrt{\varepsilon_c - \sin^2 \theta_i} \sqrt{\varepsilon_c - \sin^2 \theta_s})}{(\varepsilon_c \cos \theta_i + \sqrt{\varepsilon_c - \sin^2 \theta_i})(\varepsilon_c \cos \theta_s + \sqrt{\varepsilon_c - \sin^2 \theta_s})}$$

$$(4\text{-}32)$$

$$I = \pi \ell^2 \, e^{-\frac{\ell^2 t^2}{4}}$$

$$(4\text{-}33)$$

for a Gaussian correlation coefficient, and

$$I = 2\pi \ell^2 \, \frac{1}{(1 + \ell^2 t^2)^{3/2}}$$

$$(4\text{-}34)$$

for an Exponential correlation coefficient, where

$$t = k_o \sqrt{\xi_x^2 + \xi_y^2}$$

$$(4\text{-}35)$$

$$\xi_x = \sin \theta_i - \sin \theta_s \cos \phi_s$$

$$(4\text{-}36)$$

$$\xi_y = \sin \theta_s \sin \phi_s$$

$$(4\text{-}37)$$

$k = \frac{2\pi}{\lambda}$ is the propagation constant in air

θ_i is the angle of incidence

θ_s, ϕ_s are the scattering angles

h is the RMS surface roughness height

ℓ is the surface height correlation length

ε_c is the relative complex dielectric constant.

Surfaces having a Gaussian surface height correlation coefficient
are smoothly curving, with derivatives existing at all points.
Surfaces with exponential correlation coefficients are jagged
and have many vertical facets.

The significance of these fractional power calculations for
the perceived brightness of the surface may be seen by considering
the total reflection from the surface in two parts. The fraction
F_d of the incident power that is scattered diffusely above the
ice surface is given in Equation (4-24). Numerical integration
of this expression for both polarizations gives the results shown in
Figures 23 (a), (b), (c) and (d). It should be emphasized that
these curves indicate only the amount of power diffusely scattered
into the half-space above the ice surface.
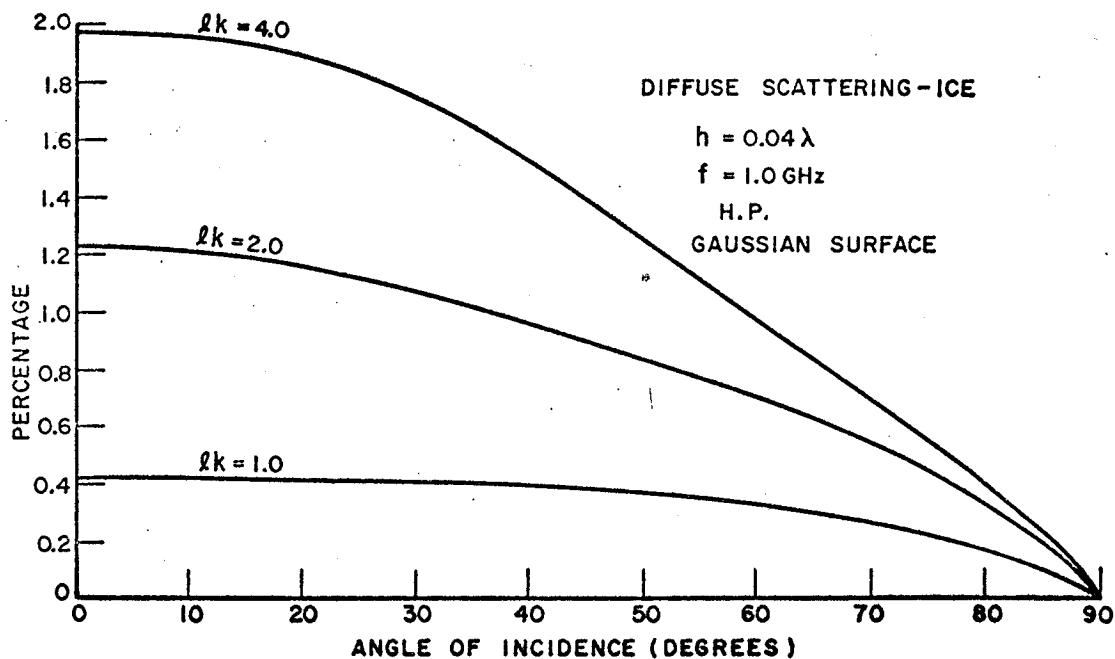
Figure 23 (a). The percentage of the incident power that is
scattered diffusely above the slightly rough
surface.

55
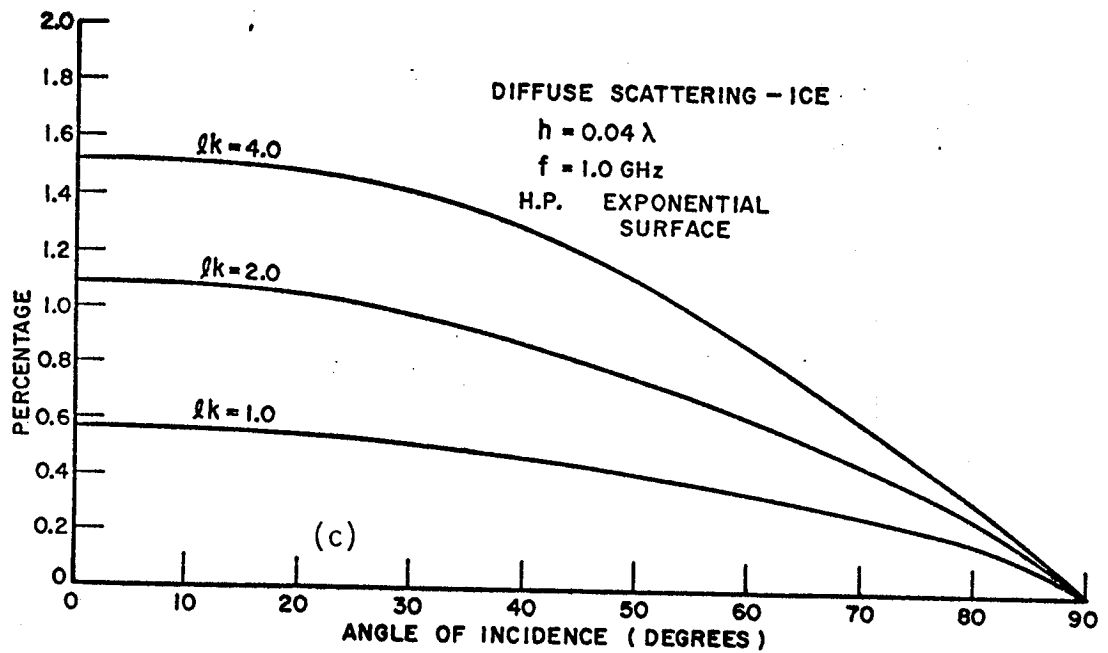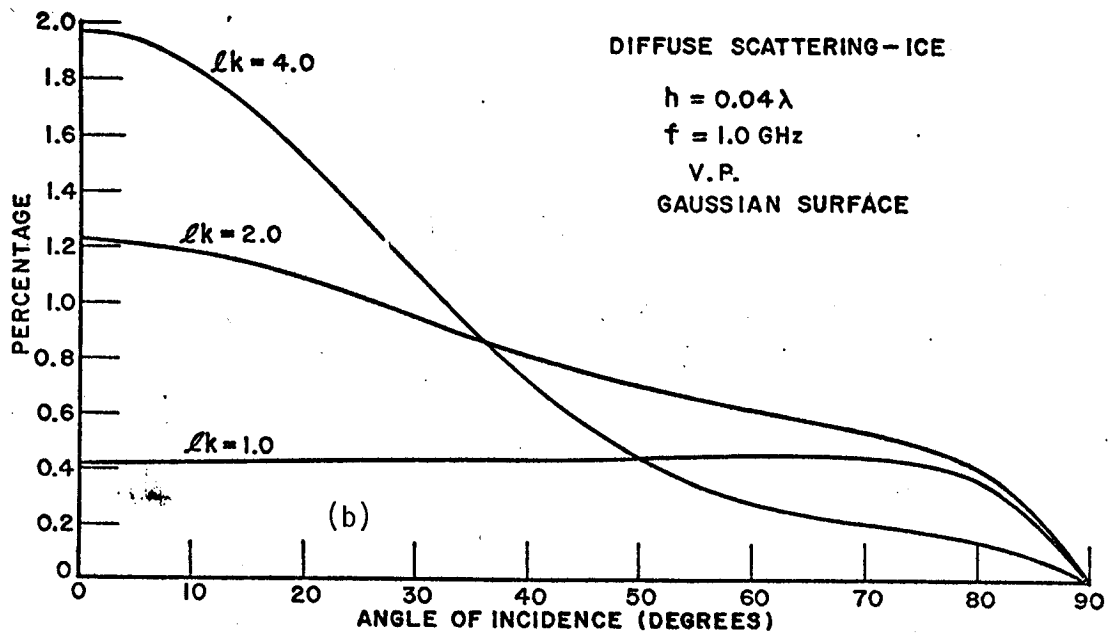
Figures 23 (b-c). The percentage of the incident power that is scattered diffusely above the slightly rough surface.
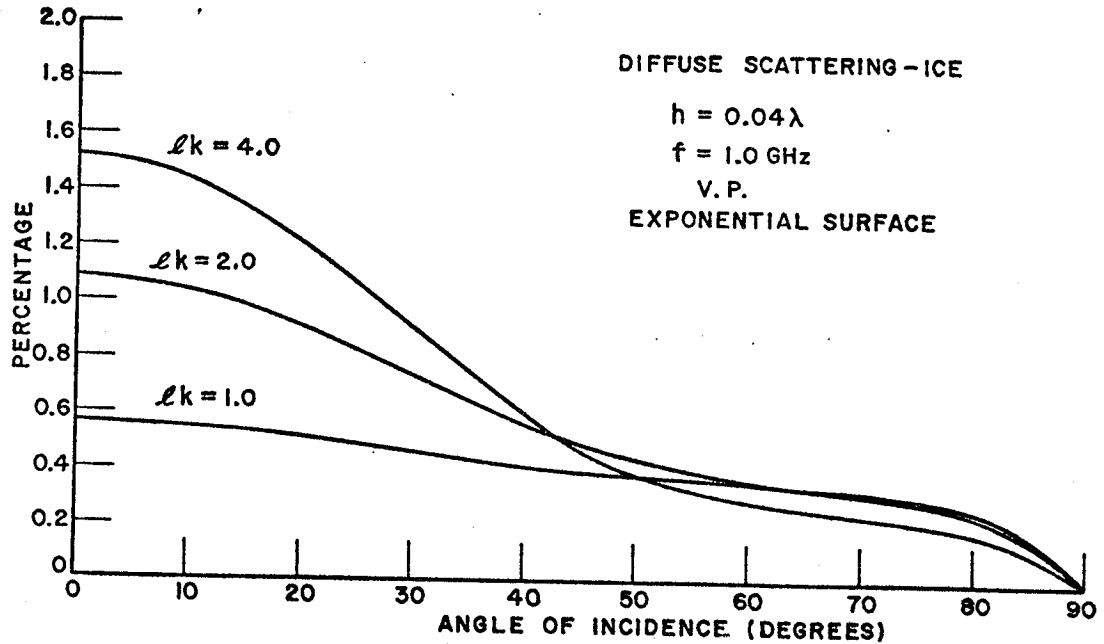
Figure 23 (d). The percentage of the incident power that is
scattered diffusely above the slightly rough
surface.

The actual change in apparent brightness temperature caused
by the surface being slightly rough may then be computed using
results of Valenzuela (1970). He showed that the effective re-
flection coefficients for horizontal and vertical polarization are

$$R'_h = R_h + \frac{1}{2} \frac{k^2 \psi(\varepsilon_c - 1)}{(\psi + \sqrt{\varepsilon_c - T^2})^2} I_h \qquad (4\text{-}38)$$

and

$$R'_v = R_v - \frac{1}{2} \frac{k^2 \psi(\varepsilon_c - 1)\varepsilon_c}{(\varepsilon_c \psi + \sqrt{\varepsilon_c - T^2})^2} I_v \qquad (4\text{-}39)$$

where

57

$$R_h = \frac{\psi - \sqrt{\varepsilon_c - T^2}}{\psi + \sqrt{\varepsilon_c - T^2}} \qquad (4\text{-}40)$$

$$R_v = \frac{\varepsilon_c \psi^- \sqrt{\varepsilon_c - T^2}}{\varepsilon_c \psi^+ \sqrt{\varepsilon_c - T^2}} \qquad (4\text{-}41)$$

$$I_n = \int_{-\infty}^{\infty} dp \int_{-\infty}^{\infty} dq \left\{ \sqrt{\varepsilon_c - T^2} + \frac{k(\varepsilon_c - 1)}{d} \left(\frac{q^2}{D_{pq}} - 1 \right) \right\} w(p - Tk, q)$$

$$(4\text{-}42)$$

$$I_v = \int_{-\infty}^{\infty} dp \int_{-\infty}^{\infty} dq \left\{ \frac{-T}{k} \left[p\sqrt{\varepsilon_c - T^2} - Tc \right] + \sqrt{\varepsilon_c - T^2} \right.$$

$$\frac{-k T^2 \varepsilon_c b}{D_{pq}} + \frac{p k T(\varepsilon_c - 1)\sqrt{\varepsilon_c - T^2} b}{d D_{pq}}$$

$$\left. \frac{-pk T\sqrt{\varepsilon_c - T^2}}{D_{pq}} - \frac{k(\varepsilon_c - 1)(\varepsilon_c - T^2)}{\varepsilon_c d} \left(\frac{1 - p^2}{D_{pq}} \right) \right\} w(p - Tk, q)$$

$$(4\text{-}43)$$

where

ε_c is the relative complex dielectric constant

$w(p,q)$ is the spectral density of the surface profile

k is the free space propagation constant,

and

$\psi = \cos \theta_i$ $T = \sin \theta_i$

$b = \sqrt{k^2 - p^2 - q^2}$ $c = \sqrt{k^2 \varepsilon_c - p^2 - q^2}$

$d = b + c$ $D_{pq} = bc + p^2 + q^2$.

The change in the apparent brightness temperature due to the surface roughness is then

$$\Delta T_b = (|R|^2 - |R'|^2 - F_d) \, T_i \qquad\qquad (4\text{-}44)$$

where

$$\Delta T_b = T_b \text{ (slightly rough surface)} - T_b \text{ (flat surface)}.$$

Because the sky brightness is quite small for the frequencies of interest here, the change in brightness due to reflected components has been assumed to be negligible in Equation (4-44). Numerical integrations of Equations (4-42) and (4-43) were performed to calculate ΔT_b. Representative results are shown in Figures 24 (a), (b), (c), and (d). These results can be considered only indicative of the brightness changes to be expected due to slight roughness on the surface. As can be seen from the figures, the slightly rough surface will look a few degrees warmer, than the smooth surfaces for scan angles of 30°, or less.

The rather complicated reflection coefficients R_h', R_v' for a slightly rough surface are often approximated by the simpler expression (4-19) where the exponential term is the power loss factor caused by roughness for a perfectly conducting surface. That the approximation is quite a good one may be judged from Table 3, which displays the correct and approximate reflection coefficients for an ice surface with $h/\lambda = .04$ for several values of correlation length ℓ.

TABLE 3

Power Reflection Coefficient of Slightly Rough Surface
Gaussian Correlation Coefficient - Horizontal Polarization

θ	$|R_h|^2$	$|R_h|^2 e^{-(2kh\cos\theta)^2}$	$\ell k=1.0$ $|R_h'|^2$	$\ell k=2.0$ $|R_h'|^2$	$\ell k=4.0$ $|R_h'|^2$
0°	0.0804	0.0625	0.0588	0.0626	0.0614
10°	0.0832	0.0651	0.0613	0.0654	0.0642
20°	0.0921	0.0737	0.0693	0.0744	0.0732
30°	0.1091	0.0903	0.0847	0.0917	0.0907
40°	0.1382	0.1191	0.1115	0.1211	0.1210
50°	0.1864	0.1679	0.1572	0.1699	0.1717
60°	0.2668	0.2505	0.2352	0.2511	0.2557
70°	0.4016	0.3899	0.3699	0.3876	0.3949
80°	0.6274	0.6626	0.6025	0.6173	0.6246
90°	1.0000	1.0000	1.0000	1.0000	1.0000

Gaussian Correlation Coefficient - Vertical Polarization

θ	$\lvert R_v \rvert^2$	$\lvert R_v \rvert^2 e$	$-(2kh\cos\theta)^2$ $\ell k=1.0$ $\lvert R_v' \rvert^2$	$\ell k=2.0$ $\lvert R_v' \rvert^2$	$\ell k=4.0$ $\lvert R_v' \rvert^2$
0°	0.0804	0.0625	0.0588	0.0626	0.0614
10°	0.0777	0.0608	0.0572	0.0609	0.0598
20°	0.0694	0.0555	0.0522	0.0557	0.0547
30°	0.0554	0.0459	0.0433	0.0462	0.0453
40°	0.0363	0.0313	0.0299	0.0318	0.0309
50°	0.0145	0.0131	0.0135	0.0137	0.0129
60°	0.0001	0.0001	0.0023	0.0004	0.0001
70°	0.0266	0.0258	0.0275	0.0232	0.0252
80°	0.2091	0.2075	0.2034	0.1981	0.2040
90°	1.0000	1.0000	1.0000	1.0000	1.0000

Exponential Correlation Coefficient - Horizontal Polarization

θ	$\lvert R_h \rvert^2$	$\lvert R_h \rvert^2 e$	$-(2kh\cos\theta)^2$ $\ell k=1.0$ $\lvert R_h' \rvert^2$	$\ell k=2.0$ $\lvert R_h' \rvert^2$	$\ell k=4.0$ $\lvert R_h' \rvert^2$
0°	0.0804	0.0625	0.0570	0.0597	0.0609
10°	0.0832	0.0651	0.0595	0.0623	0.0636
20°	0.0921	0.0737	0.0676	0.0709	0.0724
30°	0.01091	0.0903	0.0832	0.0874	0.0892
40°	0.1382	0.1191	0.1103	0.1159	0.1183
50°	0.1864	0.1679	0.1564	0.1638	0.1675
60°	0.2668	0.2505	0.2348	0.2446	0.2497
70°	0.4016	0.3899	0.3699	0.3811	0.3876
80°	0.6274	0.6226	0.6028	0.6124	0.6182
90°	1.0000	1.0000	1.0000	1.0000	1.0000

Exponential Correlation Coefficient - Vertical Polarization

θ	$\lvert R_v \rvert^2$	$\lvert R_v \rvert^2 e$	$-(2kh\cos\theta)^2$ $\ell k=1.0$ $\lvert R_v' \rvert^2$	$\ell k=2.0$ $\lvert R_v' \rvert^2$	$\ell k=4.0$ $\lvert R_v' \rvert^2$
0°	0.0804	0.0625	0.0570	0.0597	0.0609
10°	0.0777	0.0608	0.0555	0.0581	0.0593
20°	0.0694	0.0555	0.0508	0.0530	0.0542
30°	0.0554	0.0459	0.0426	0.0439	0.0448
40°	0.0363	0.0313	0.0309	0.0302	0.0305
50°	0.0145	0.0131	0.0176	0.0134	0.0128
60°	0.0001	0.0001	0.0108	0.0020	0.0004
70°	0.0266	0.0258	0.0405	0.0279	0.0258
80°	0.2091	0.2075	0.2161	0.2054	0.2048
90°	1.0000	1.0000	1.0000	1.0000	1.0000
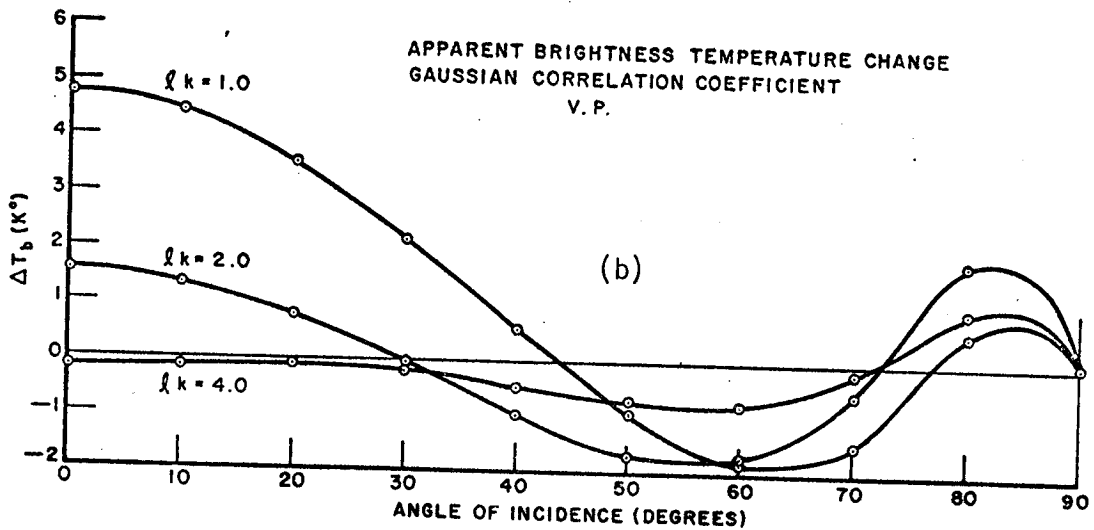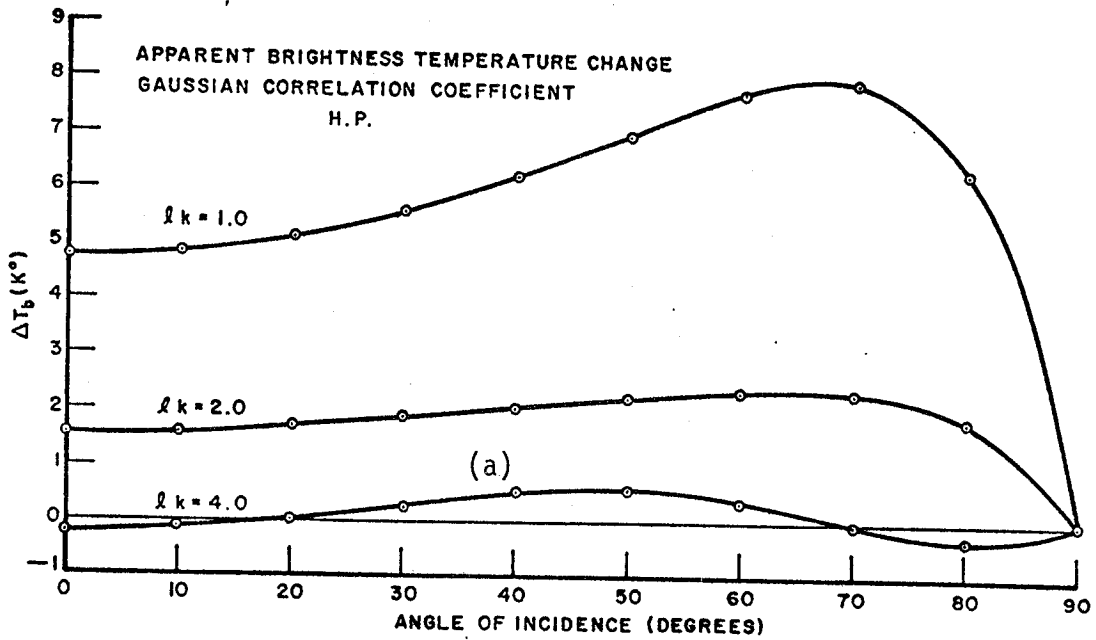
Figures 24 (a-b). Changes in the apparent brightness temperature due to slight roughness on the surface. Reflected components have been neglected.

61
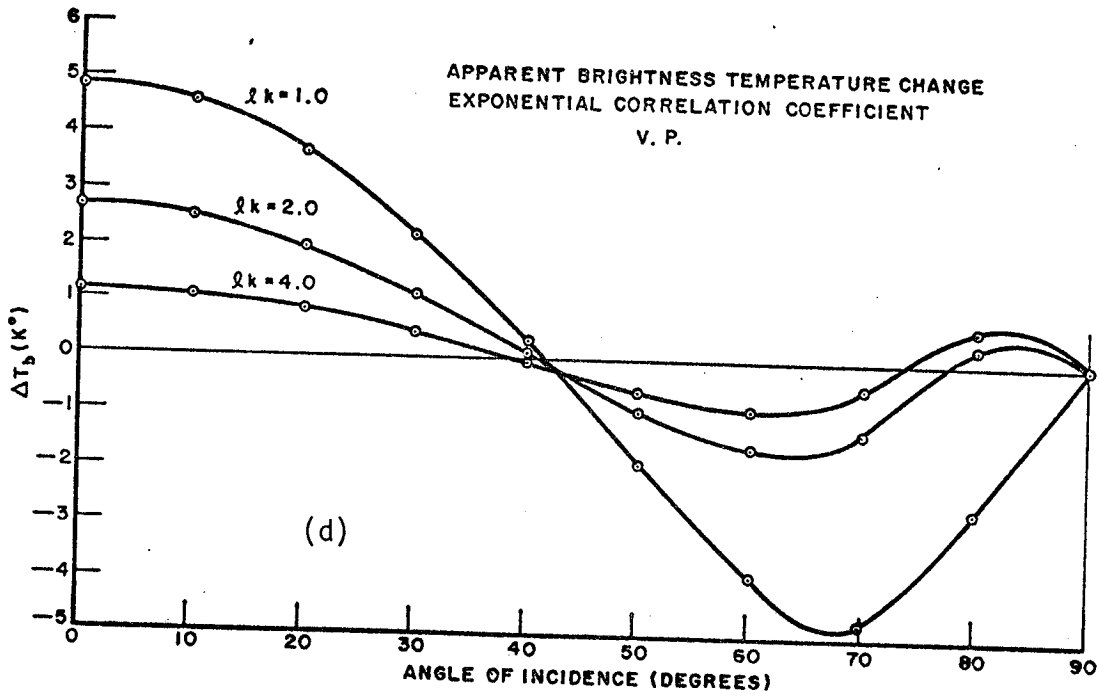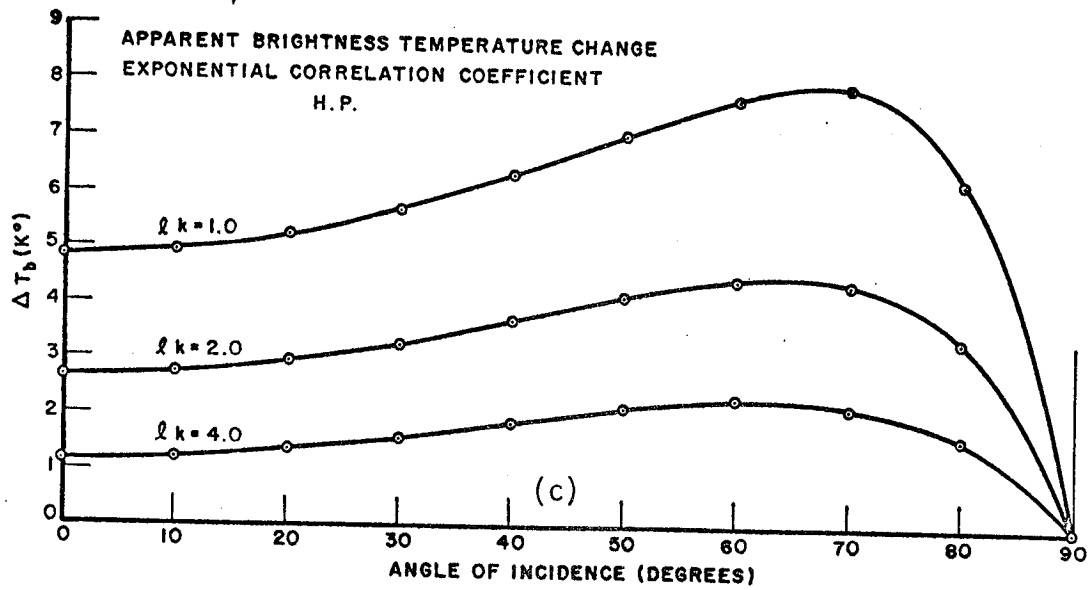
Figures 24 (c-d). Changes in apparent brightness temperature due to slight roughness on the surface. Reflected components have been neglected.

8. Multilayering of Ice - Large Scale Roughness

The small scale roughness theory of the preceding section can predict the effect of surface roughness between two media on the order of a few centimeters or less (for the frequencies concerned in this report). The actual lake ice could very well have surface variations much greater than this if, for example, any rafting is present. The radiometer antenna could also see a continuum of ice layer thicknesses if it was observing the ice close to open water. The effect of the presence of a number of different thicknesses within the antenna footprint on the apparent brightness temperature is shown in Figure 25. The "9.5 cm" curve, for example, shows the temperature the antenna would see if on top of any given ice layer there were additional slabs ranging in thickness from 0.5 to 9.5 cm, with equal weighting as seen by the antenna. The presence of multiple thicknesses tends to smooth out the oscillation in brightness. The increase in the effective total thickness is reflected in the lateral shift of the sinusoidal curve. The effect of the smoothing in the frequency domain is shown in Figures 26 (a) and (b). The separation of the nulls along the frequency axis is inversely proportional to the spread in thickness as predicted by Equation (2-4). For example, in Figure 26 (b) when the thickness spread increases from 4 cm to 10 cm, the location of the first null changes from 2.0 GHz to 0.8 GHz. Furthermore, the null locations depend only on the multilayering, and not on the basic ice thickness, so that a 10 cm thickness variation places a null around 0.8 GHz regardless of the average ice thickness. It is clear that the presence of multiple thicknesses will have an adverse effect on most ice thickness prediction methods that depend on the presence of the interference phenomenon, and place an upper limit on the maximum useful frequency, $f_{max} \simeq c/(3\sqrt{\varepsilon_i} \; \Delta d)$ where Δd is the range of thicknesses within the beam.

9. Air Bubbles in Ice

The ice model used in the previous calculation is quite low in loss, and applies to ice free of cracks, bubbles, inclusions, etc.. Unfortunately, that is not always the case for ice found in the natural state. Ice samples taken from the Great Lakes, for example, can show a high air bubble content. Measurement, Vickers (1975), of the relative complex dielectric constant of these samples produces real parts that vary between 3.2 and 3.0 with losses from 1 dB/m to approximately 4 dB/m at 1 GHz. This loss variation corresponds to the imaginary part of the dielectric constant varying from -.02/f to -.08/f (f is in GHz). The classic mixture formulae correctly predict the change in the real part of the dielectric constant but not in the imaginary part, and therefore cannot be used in modeling air bubbles in ice. The

63
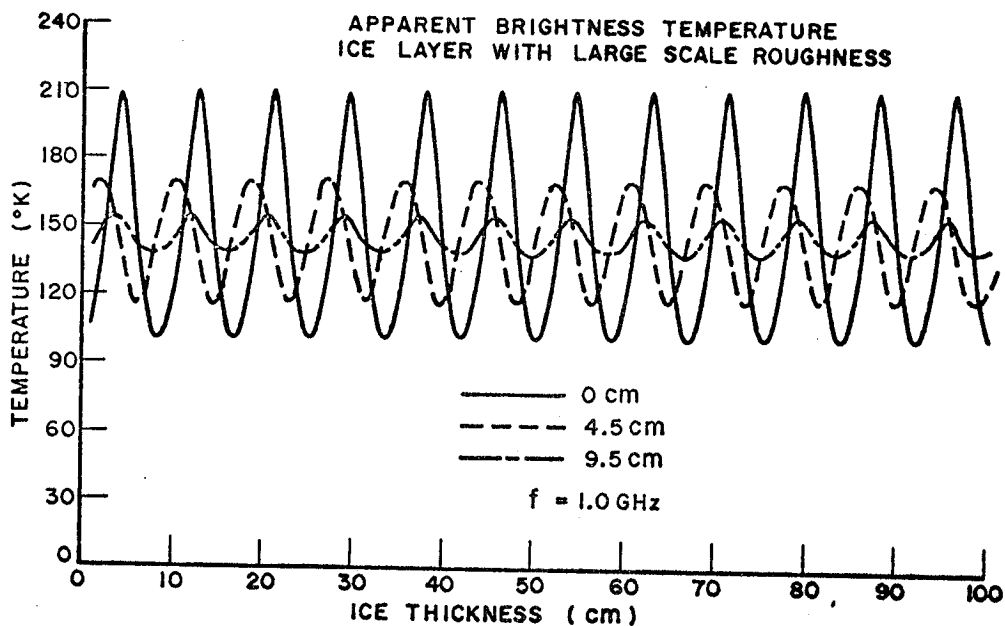
Figure 25. Changes in the apparent brightness temperature due to presence of additional ice slabs on top of the basic ice layer.
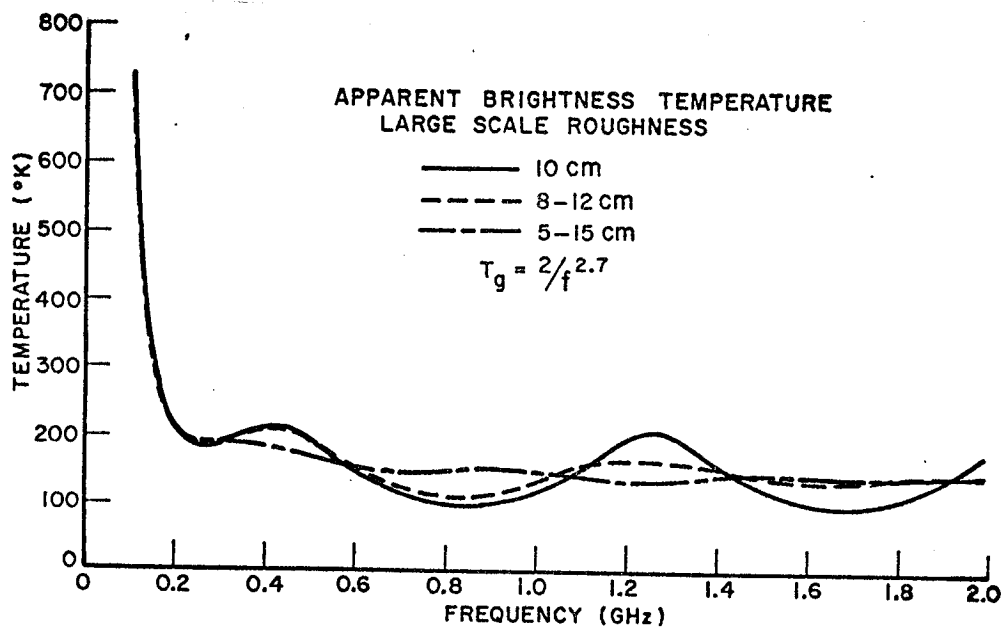
Figure 26 (a). Changes in the apparent brightness temperature due to presence of ice multi-thickness.

APPARENT BRIGHTNESS TEMPERATURE
LARGE SCALE ROUGHNESS

$$T_g = 2/f^{2.7}$$
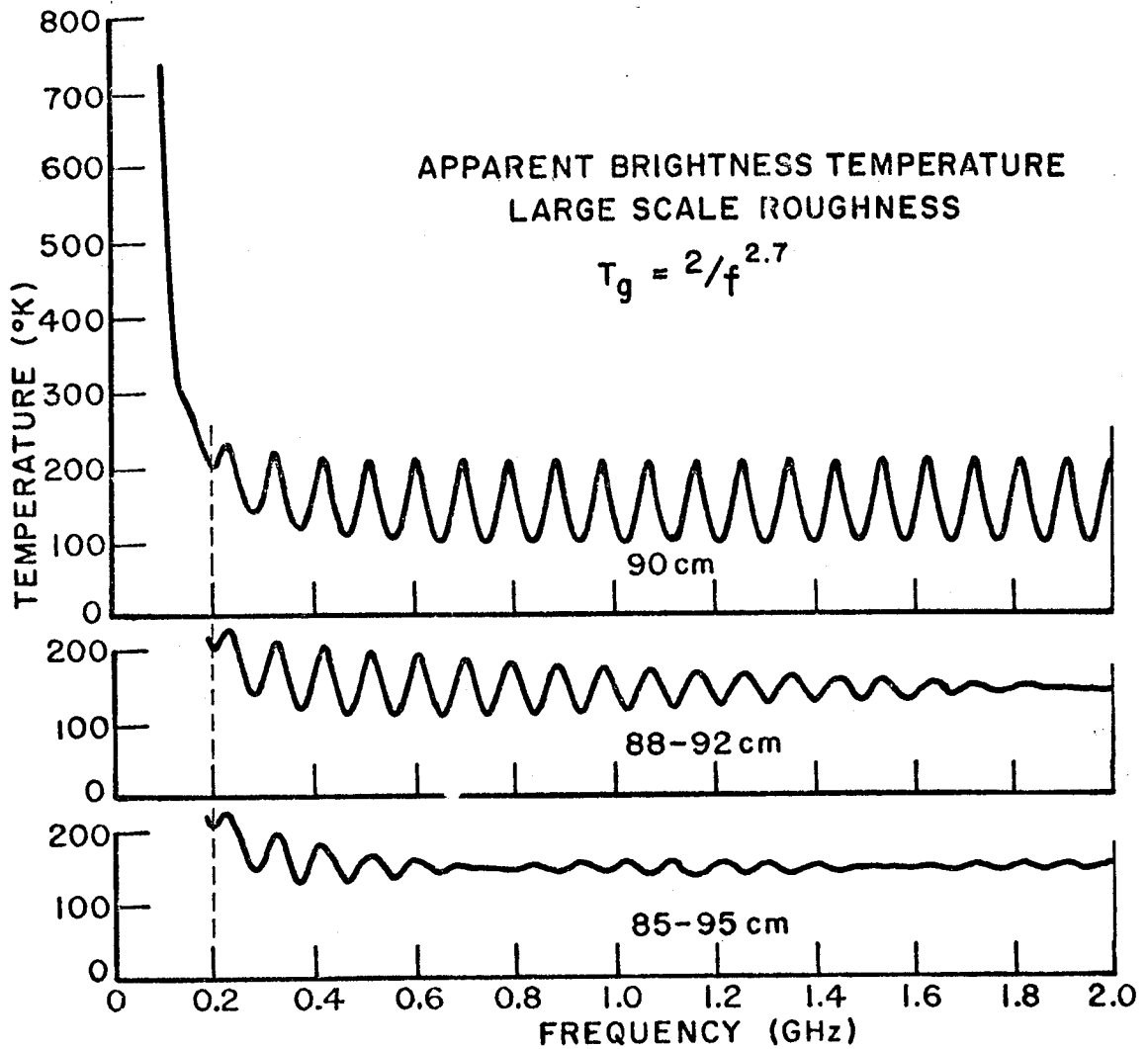
Figure 26 (b). Changes in the apparent brightness temperature due
to presence of ice multi-thickness.

effect of the increased lossiness on the apparent brightness temper-
ature for two different ice thicknesses as a function of frequency
is shown in Figures 27 (a) and (b). Typical effects of lossy ice
and multilayering on the apparent brightness temperature at .4 GHz
is shown in Figure 28. The "harmonic content" changes and the
"dc" level shifts considerably, but the period of oscillations re-
mains about the same. Any data processing method will have to ad-
just to this fact if it is to cope with lossiness and multilayering.
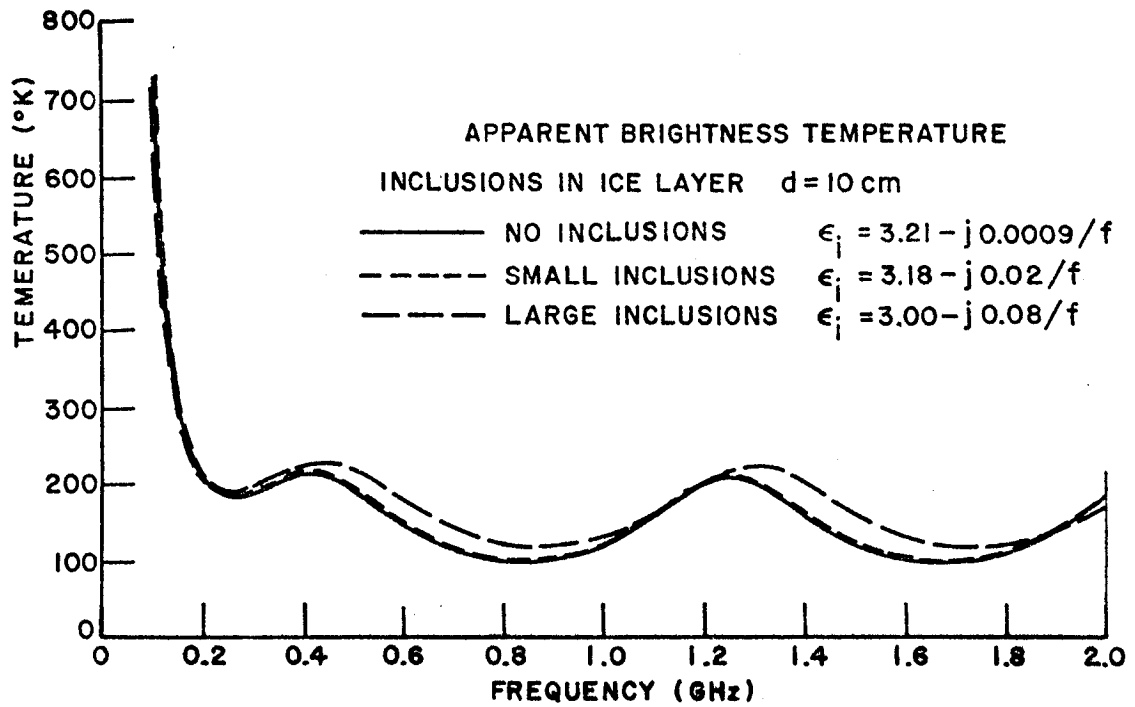
Figure 27 (a). Changes in the apparent brightness temperature due to presence of air inclusions in ice.

APPARENT BRIGHTNESS TEMPERATURE

INCLUSIONS IN ICE LAYER d = 100 cm

$$T_g = {}^2/f^{2.7}$$

NO INCLUSIONS ϵ_i = 3.21 - j0.0009/f

SMALL INCLUSIONS ϵ_i = 3.18 - j0.02/f

LARGE INCLUSIONS ϵ_i = 3.00 - j0.08/f
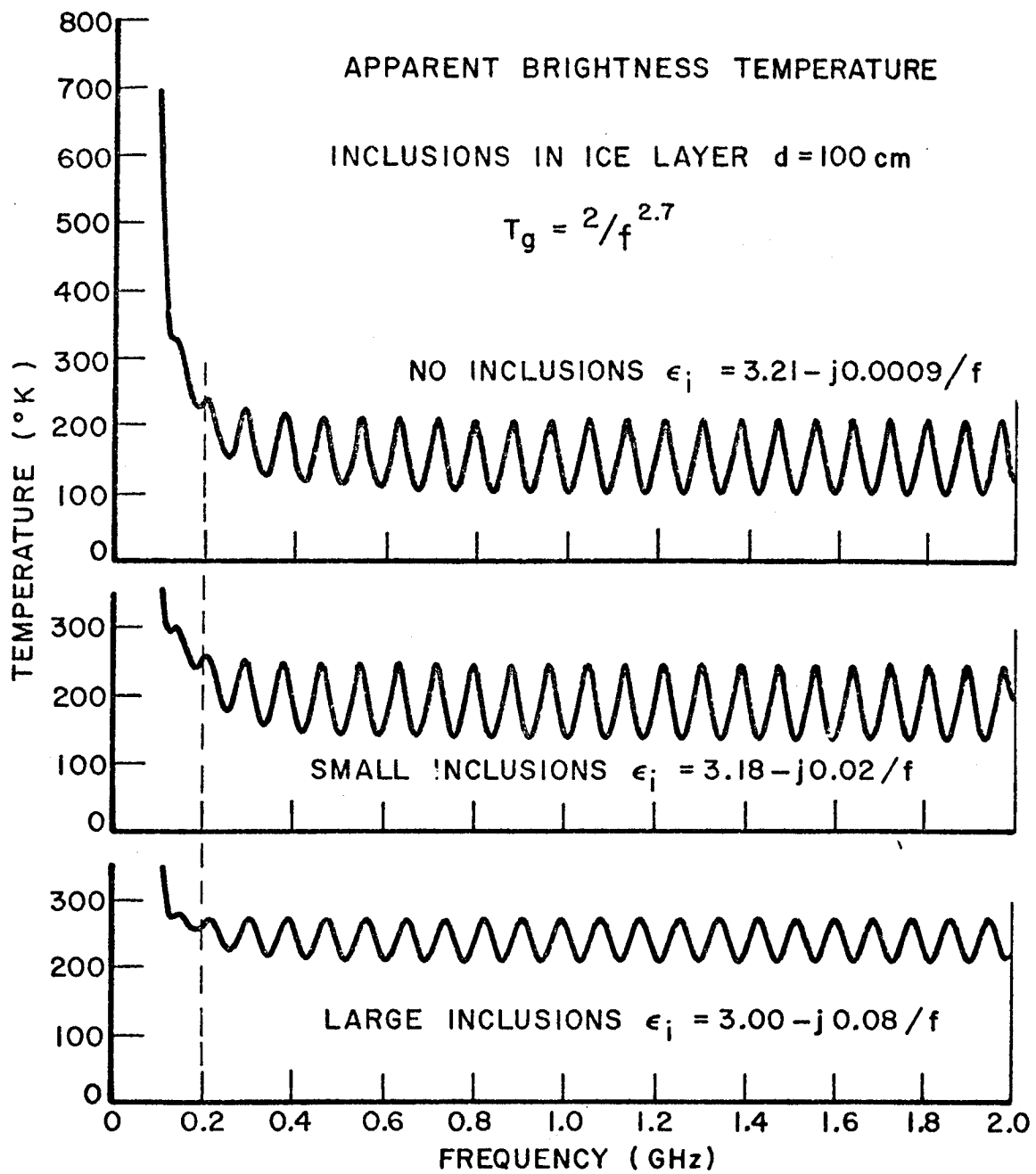
Figure 27 (b). Changes in the apparent brightness temperature due to presence of air inclusions in ice.

APPARENT BRIGHTNESS TEMPERATURE

f = 0.4 GHz

Legend:
- $\epsilon_i = 3.21 - j0.0009/f$
- $\epsilon_i = 3.00 - j0.08/f$
- $\epsilon_i = 3.00 - j0.08/f$ 10 cm LAYERING

X-axis: ICE THICKNESS (cm)

Y-axis: TEMPERATURE (°K)
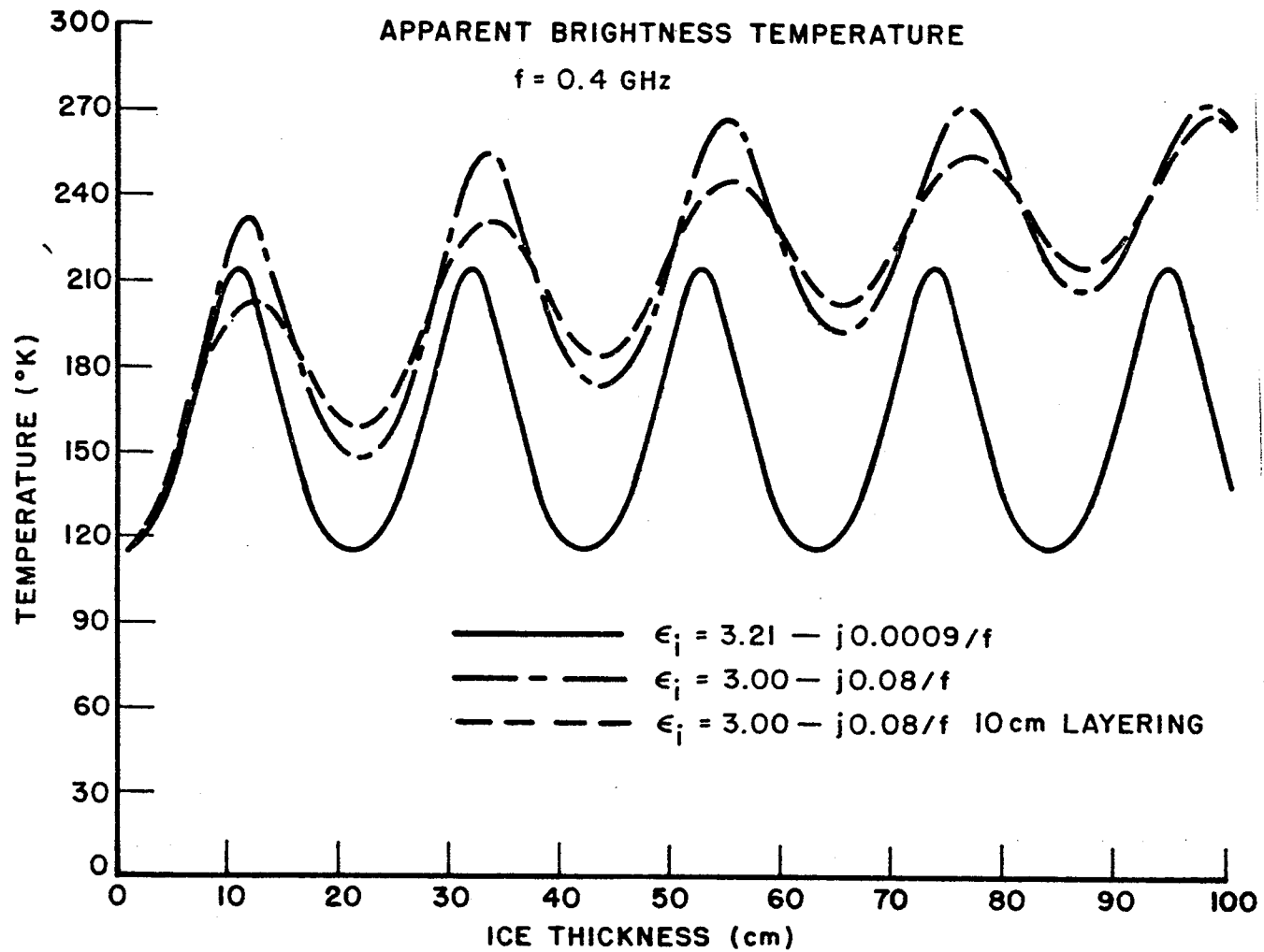
Figure 28. The apparent brightness variation with increasing ice loss and ice multilayering.

CHAPTER V

DATA PROCESSING FOR CLEAR SINGLE LAYER ICE

0. Introduction

In this chapter, we consider two types of realizations of
automatic ice thickness measuring schemes. The first is based
on measurements at frequencies low enough (say 150 MHz or less)
so that the apparent brightness temperature is dominated by the
reflected cosmic radiation. At such low frequencies, for ice
up to a meter or so thick, only two or three frequency channels
are needed for an unambiguous thickness determination. The
second type of system, operating at frequencies where the
brightness temperature is dominated by emission (about 300 MHz
or higher), requires in its most direct form, $N = d_{max}/d_{min} + 1$
channels. The object of the work described here, however,
is to develop data processing schemes which will permit unam-
biguous thickness determination using the least possible number
of frequency channels consistent with a reasonable constraint
on the probable ice thickness error. All calculations in this
chapter will assume the ice to be clear and of uniform thickness.

1. Low Frequency Measurements

This section is basically concerned with how to measure ice
as much as a meter thick, using as few frequencies as possible.
It will be seen that the requirement for minimum number of
frequency channels forces the frequencies to be very low. At low
frequencies, however, the galactic noise temperature is a very
large, imprecisely known quantity, and the data processing
methods have to be designed to cope with this. Although in
principle, by working on the first half cycle of the reflection
coefficient vs. ice thickness curve, only a single frequency would
suffice, we do not consider such systems here because at the
frequencies required (less than 50 MHz), problems of antenna
design and cosmic noise uncertainty make them impractical.

A. Two Antenna System

From Figure 6, it can be seen that unambiguous resolution of
ice thicknesses up to one meter, by means of brightness measure-
ments at two or three frequencies, requires that the frequencies
be on the order of 0.1 GHz. In this frequency range, the galactic
noise temperature has great variation but is in general very
large as shown in Figures 4 and 5. The actual value of the
galactic noise temperature depends on the position in the sky,

the antenna beamwidth, etc. It is on the order of many thousands of degrees near the galactic center, and it falls off to many hundreds of degrees in the direction of the galactic pole. The physical temperature of ice, on the other hand, is 273° K or less, and so the reflection mechanism clearly dominates the emission at these low frequencies. The apparent brightness temperature was given as

$$T_b = (1 - |R|^2) T_i + |R|^2 (T_g + T_a) \quad , \tag{3-1}$$

so that if $\quad T_g + T_a >> T_i$

then $\qquad T_b \sim |R|^2 (T_g + T_a)$. $\tag{5-1}$

It should be noted that the atmospheric noise temperature contribution T_a is on the order of few degrees K, and thus may be considered at these low frequencies negligible in comparison with T_g. The apparent brightness temperature can be viewed then as the power reflection coefficient multiplied by the large but variable galactic noise. Hence, it would be desirable if the data processing method did not have to rely on accurate, absolute temperature measurements.

One obvious approach to the problem is to measure both $T_g + T_a$, and T_b. Thus, T_b is measured with a downward looking antenna, and the temperature incident upon the ice layer from above, namely $T_g + T_a$, is measured with an upward looking antenna. As can be seen from Equation (5-1), the ratio of T_b to $T_g + T_a$ will be an approximation to the power reflection coefficient, i.e.

$$|R|^2 = (T_b - T_i)/(T_g + T_a - T_i) \simeq T_b/(T_g + T_a) \quad . \tag{5-2}$$

A slightly better approximation would be to assume that the unknown ice temperature T_i is 270° K, so that

$$|R|^2 \simeq (T_b - 270)/(T_g + T_a - 270) \quad . \tag{5-3}$$

A theoretical, or pre-calculated, power reflection coefficient curve can then be used as a training set for identification of each measured unknown ice thickness. Thus, the training

70

set for a single frequency realization is just a graph of $|R|^2$
vs thickness. For example, (see Figure 13) at 0.1 GHz, only a
small range of thicknesses (0cm -40cm) can be measured unambig-
uously. To extend the unambiguous range, two frequencies may
be used; the training set can then be represented as a plane
curve with ice layer thickness as a parameter. For example,
Figure 29 (a) is the locus of 199 two-dimensional vector tips
representing thicknesses from 1 to 100 cm, in 0.5 cm steps,
for two frequencies of 0.9 GHz and 0.11 GHz. By using two
frequencies, the unambiguous thickness measurement range is
now approximately 15 cm to 70 cm. To implement such a system,
one must then, at each of the two frequencies, measure the
brightness seen by an upward looking antenna and a downward
looking antenna, and use the up/down brightness ratios as
estimates of the reflection coefficients, these being the two
components of the measurement vector.
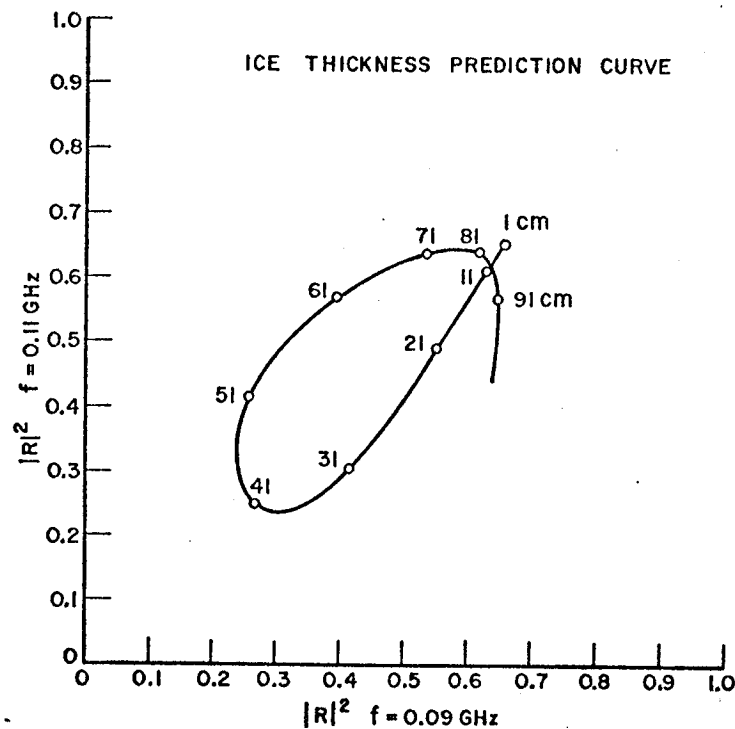
Figure 29 (a). Pre-computed power reflection coefficients at
two frequencies to be used as a training set
for ice thickness prediction.

71
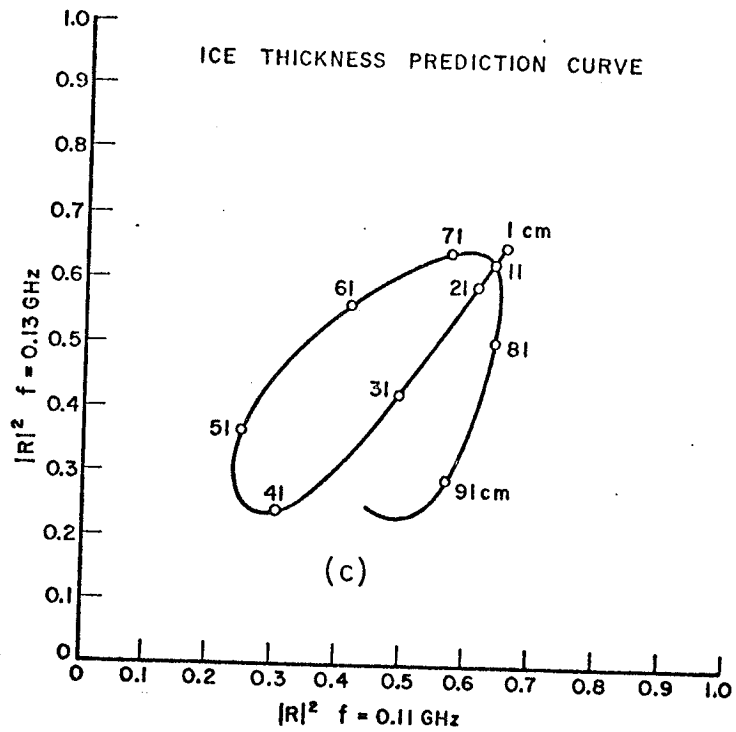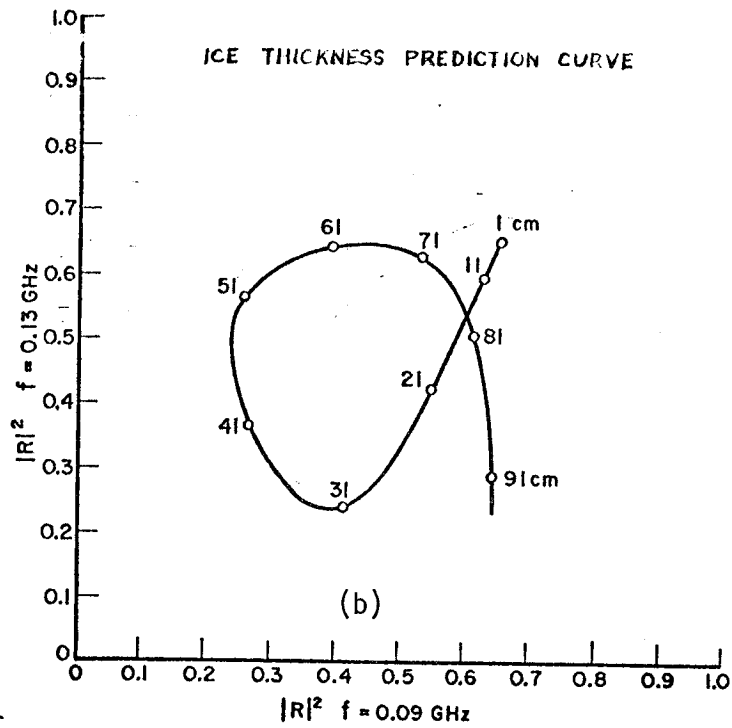
Figures 29 (b-c). Pre-computed power reflection coefficients at two frequencies to be used as a training set for ice thickness prediction.

72

The actual thickness estimate is accomplished using a minimum distance algorithm, Tou and Gonzales (1974), (often known as the nearest neighbor rule). The measurement vector from an unknown ice thickness is compared to each of the vectors in the training set to determine the best fit. The criterion for best fit is simply the minimum geometric distance between the measurement vector and each of the other vectors in the training set. Once the minimum distance has been found, the identification process is complete, and the measured ice thickness is assumed to be that of the vector in the training set which produced the best fit.

As mentioned above, even for frequencies as low as 0.09 GHz and 0.11 GHz an ambiguous crossover point exists in the training set. For example, (see Figure 29 (a)) a measurement vector from ice 10 cm thick could easily be interpreted as ice 84 cm thick. Clearly, the set of ambiguous thicknesses will depend on the measurement error. To reduce the ambiguity range, at the expense of system complexity, one must include data at a third frequency, thus, increasing the dimension of the measurement space from two to three. The locus, or training set, must now be plotted in a three dimensional space. The two dimensional locus (e.g. Figure 29 (a)) would then be the projection of this three dimensional curve onto a plane. Because the three dimensional locus is difficult to present (two projections of such a locus are shown in Figures 29 (b) and (c)) we give here only the results for some representative system realizations. A typical performance result for temperature measurements at three frequencies and for a galactic temperature of $T_g \doteq 20/f^{2.7}$ is shown in Figure 30. Depicted is the predicted vs actual ice thickness using the above outlined method with a 199 member training set and with the measured power reflection coefficient based on the approximation $|R|^2 = T_b/(T_g + T_a)$. The average error of 1.475 cm is the sum of deviations from the 45 degree line divided by the number of thicknesses. Clearly, apart from a small quantization error, the minimum distance algorithm should give almost perfect results if the exact expression, Equation (5-2), were used. However, the error curve shown in Figure 30 can be considered typical of the results that might be achieved with such a system for systematic errors of order of 300K° in measuring the upward and downward brightness temperature.

As pointed out before, this data processing method depends on having $T_g \gg T_i$. Thus, as the galactic noise temperature becomes smaller, the performance will deteriorate. The effect is shown in Figure 31, which repeats the "average error" calculation of Figure 30 for a range of galactic temperatures. When G has

73
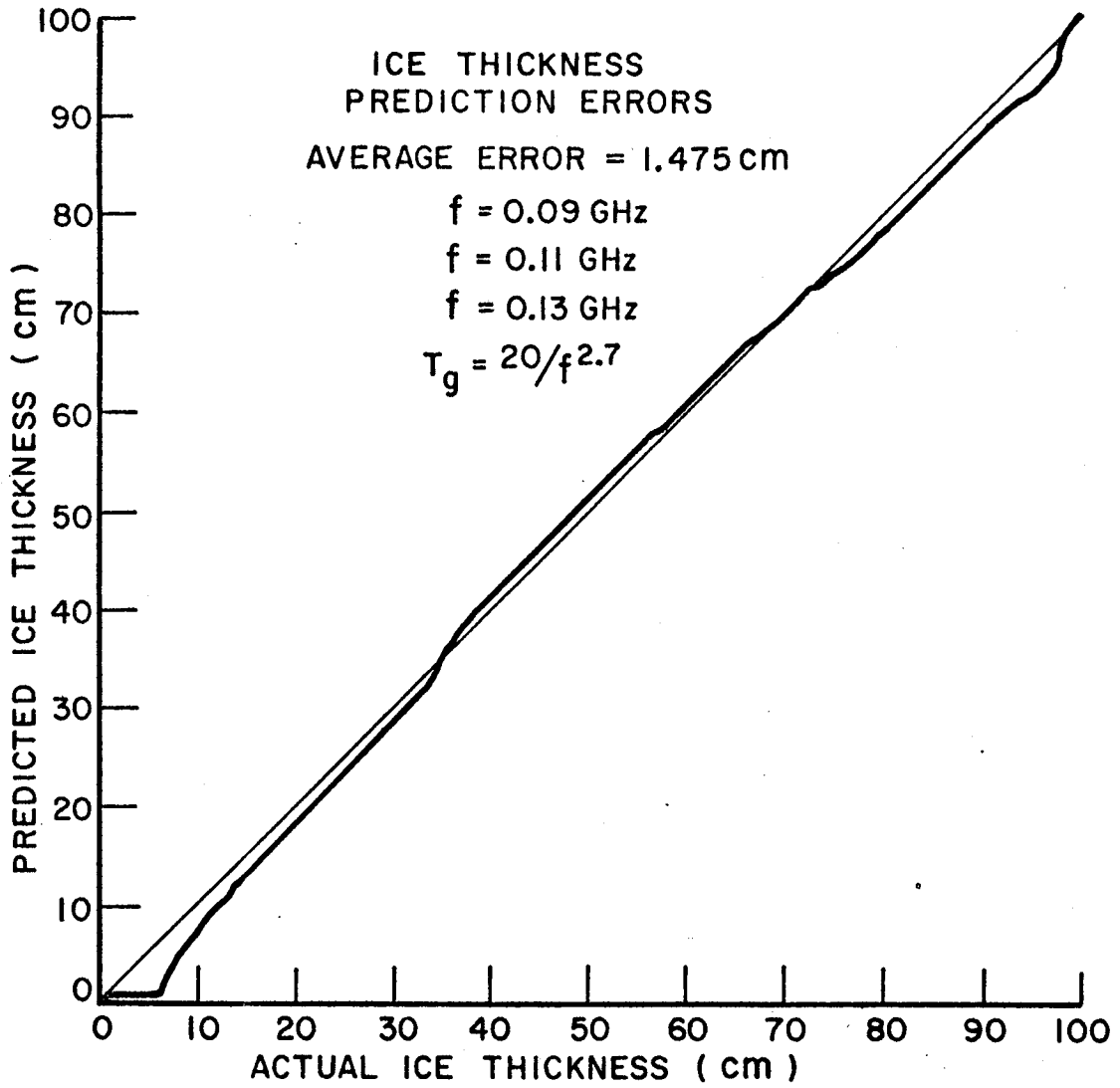
Figure 30. Ice thickness prediction errors using low frequency
two-antenna measurement system for galactic temperature
factor G=20.
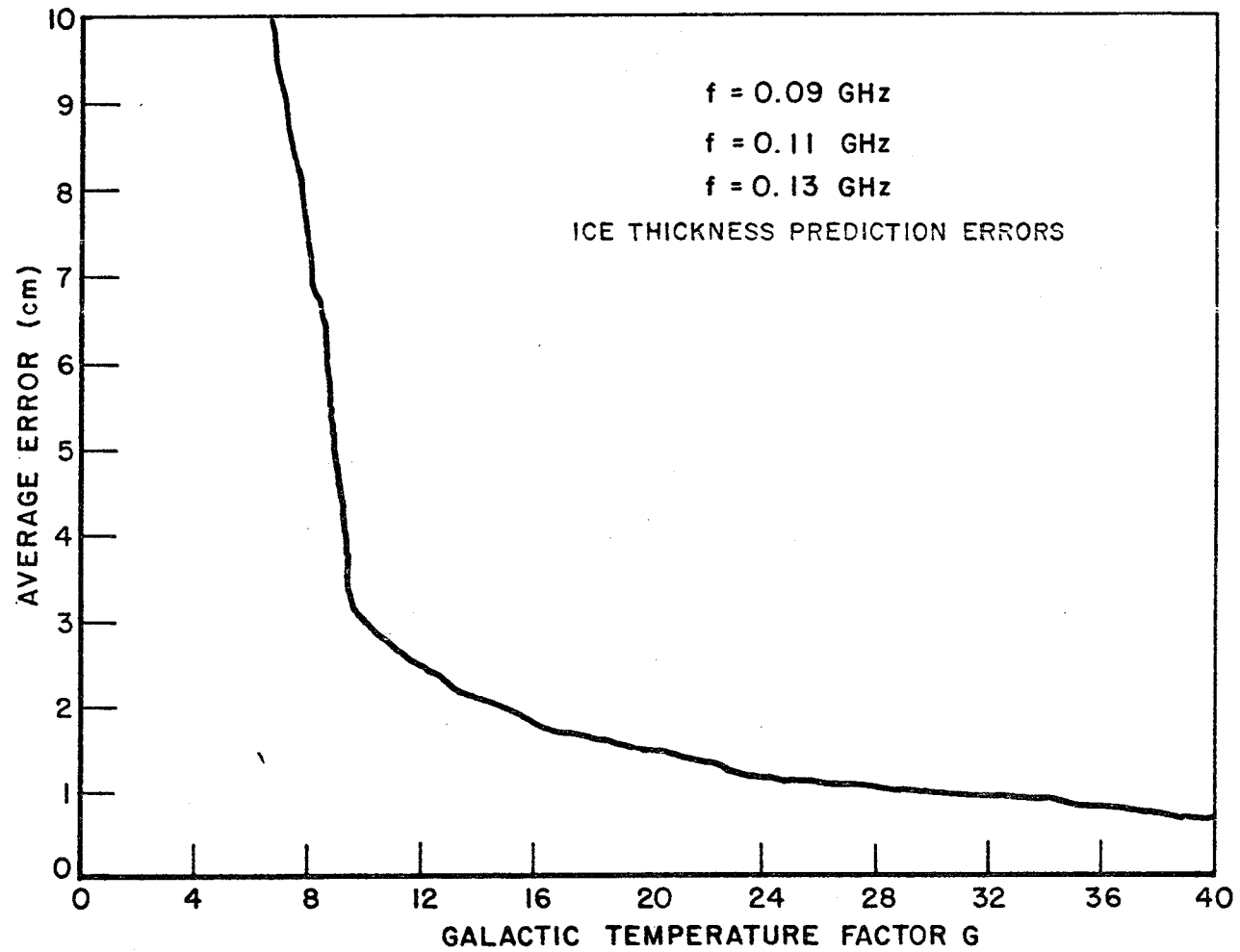
Figure 31. Ice thickness prediction errors using low frequency two-antenna measurement system as a function galactic temperature factor G.

decreased to about 10, this data processing method fails at frequencies near 0.1 GHz for the kind of measurement errors represented by the approximation in Equation (5-2). In practice, one would use the better approximation, i.e. assume $T_i = 270°$K, but would be subject to both random and systematic measurement errors. Furthermore, since the galactic temperature is a function of position in the sky, if the downward looking antenna is to scan, then so must the upward looking antenna. Clearly, a far more practical arrangement would be one which requires only a single downward looking antenna.

B. One Antenna System

If the airborne measurement system has only one downward looking antenna, then it is not possible to measure the galactic plus atmospheric contributions to the apparent brightness temperature explicitly. The effect of the unknown and variable galactic noise temperature can be minimized by a data processing approach that utilizes the brightness temperature ratio at a pair of frequencies as the component of the measurement vector. Thus, from three frequency channels, one may find two temperature ratios to obtain a two component measurement vector. Assuming again, that the frequency is low enough so that T_g is very large compared to T_i and T_a can be neglected, then the apparent brightness temperatures measured at three frequencies can be considered to be

$$T_b(f_1) \sim |R(f_1,d)|^2 \, G/f_1^{2.7} \tag{5-4}$$

$$T_b(f_2) \sim |R(f_2,d)|^2 \, G/f_2^{2.7} \tag{5-5}$$

$$T_b(f_3) \sim |R(f_3,d)|^2 \, G/f_3^{2.7} \tag{5-6}$$

where $|R(f,d)|^2$ is the power reflection coefficient at frequency f and the ice layer thickness d. Expressions for the power reflection coefficient at either polarization are given in Equation (4-7) and Equation (4-12). The two components of the measurement vector then become for example,

$$\frac{T_b(f_1)}{T_b(f_3)} \sim \frac{|R(f_1,d)|^2}{|R(f_3,d)|^2} \left(\frac{f_3}{f_1}\right)^{2.7} \tag{5-7}$$

and

$$\frac{T_b(f_2)}{T_b(f_3)} \sim \frac{|R(f_2,d)|^2}{|R(f_3,d)|^2} \left(\frac{f_3}{f_2}\right)^{2.7} . \qquad (5\text{-}8)$$

To the extent that $T_b \gg T_i \gg T_a$, the two numbers represented by these two equations are functions of ice layer thickness but not of the absolute value of the galactic noise temperature.

The invariance of the measured temperature ratios with changes in the galactic temperature can also be seen from a geometric consideration. If a plot is made of $T_b(f=0.09 \text{ GHz},d)$ vs $T_b(f=0.11 \text{ GHz},d)$ for example, for all ice thicknesses d, the curve will be similar in form to the curve of Figure 29 (a), since at low frequencies the apparent brightness temperature is approximately proportional to the power reflection coefficient. If the galactic temperature factor G is increased, both temperatures at each ice thickness would increase proportionally, and the shape of the curve would remain the same. Hence, the slope of any vector from the origin to any given ice thickness on the temperature curve would remain the same. The value of the slope is just given by Equation (5-7). This approximate invariance of the measured temperature noise ratios is the basis for the data processing method of this section.

Each of the vectors in the training set is constructed using a theoretical temperature ratio for each vector component. A general expression for the two-dimensional training vector as a function of ice layer thickness d is

$$\begin{bmatrix} S_1 \\ S_2 \end{bmatrix}$$

where

$$S_1 = \frac{(1 - |R(f_1,d)|^2)T_i + |R(f_1,d)|^2(T_g(G,f_1) + T_a(f_1))}{(1 - |R(f_3,d)|^2)T_i + |R(f_3,d)|^2(T_g(G,f_3) + T_a(f_3))}$$

$$(5\text{-}9)$$

and

77

$$S_2 = \frac{(1 - |R(f_2,d)|^2)T_i + |R(f_2,d)|^2(T_g(G,f_2) + T_a(f_2))}{(1 - |R(f_3,d)|^2)T_i + |R(f_3,d)|^2(T_g(G,f_3) + T_a(f_3))} \quad .$$

$$(5\text{-}10)$$

In the data processing method of the preceding section, the training set was formed using theoretical estimates of the power reflection coefficient. In this case, an assumed value of G must be incorporated in the training set. One such training set is shown in Figure 32. This, as before, is the locus of 199 vectors representing ice layer thickness from 1 cm to 100 cm in 0.5 cm increments. One component of each vector is given
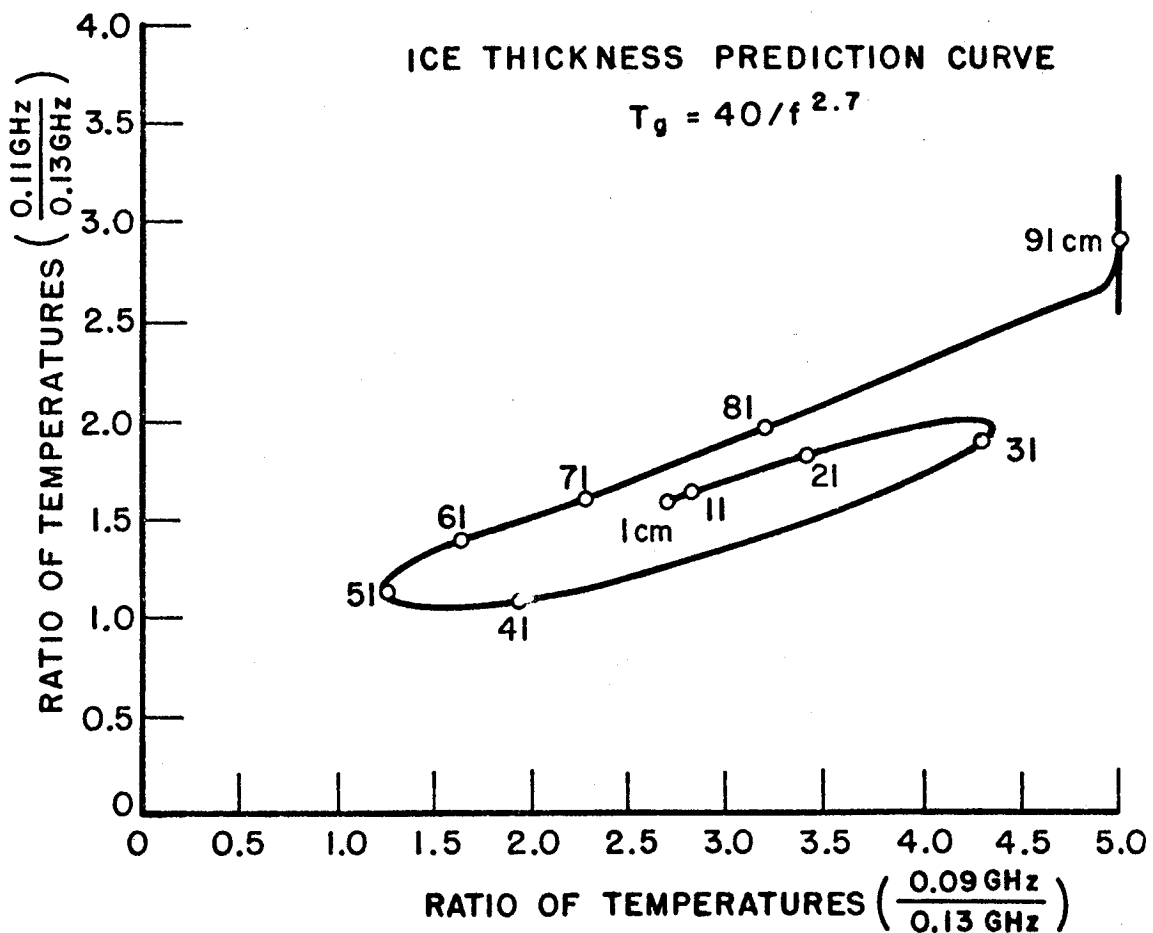
Figure 32. Ratios of pre-computed apparent brightness temperatures to be used as a training set for ice thickness prediction.

by S_1, the other component by S_2. Here the maximum possible
galactic noise (G=40) has been used for calculating the vectors
of the training set. The measurements are simulated by computing
an "observed" brightness temperature using a G different from
the one used in calculating the training set. The measurement
vectors are then constructed in the same way as the training set
vectors. The remainder of the data processing uses the minimum-
distance algorithm as outlined before. Once a two-dimensional
measurement vector is formed from three temperature measurements,
the measurement vector is compared to each of the 199 vectors
in the training set to find the best fit, the criterion again
being the minimum geometric distance between the measurement
vector and each of the training set vectors.

If the apparent brightness temperature measurements are
made in an environment having the same galactic temperature as
assumed in the construction of the training set, the performance
of this data processing method should be errorless, in principle
If, on the other hand, the actual galactic noise temperature
differs from that assumed in the training set, the performance
of the data processing method will deteriorate. For example,
if the training set of Figure 32, which was constructed assuming
the maximum galactic noise (G=40), is used to identify measure-
ment vectors that have been made in an environment having an
actual galactic noise temperature $T_g=20/f^{2.7}$ i.e., G=20, the
performance results are shown in Figure 33. The average error
of 0.832 cm is, as before, the sum of the deviations of the
predicted thickness curve from the 45 degree line divided by
the total number of thicknesses (199).

It is clear that the closer the galactic noise factor G
used in construction of the training set is to the G assumed
to be in the measurement environment, the better will be the
performance of this data processing method. This variation in
performance is shown in Figure 34. Plotted here are the average
errors in predicted thickness for training sets (constructed with
G = 40, = 30, =20) as a function of the actual galactic temper-
ature.

Comparing Figure 31 and Figure 34, it can be seen that both
methods are comparable in performance, but the latter method has
the advantage of requiring only one antenna. In both methods,
there is no need for accurate absolute temperature measurements
since calibration errors have only a small effect on the bright-
ness ratios used to form the measurement vector. Both methods,
however, do depend upon the galactic noise temperature being much
larger than the physical temperature of the ice, and the performance
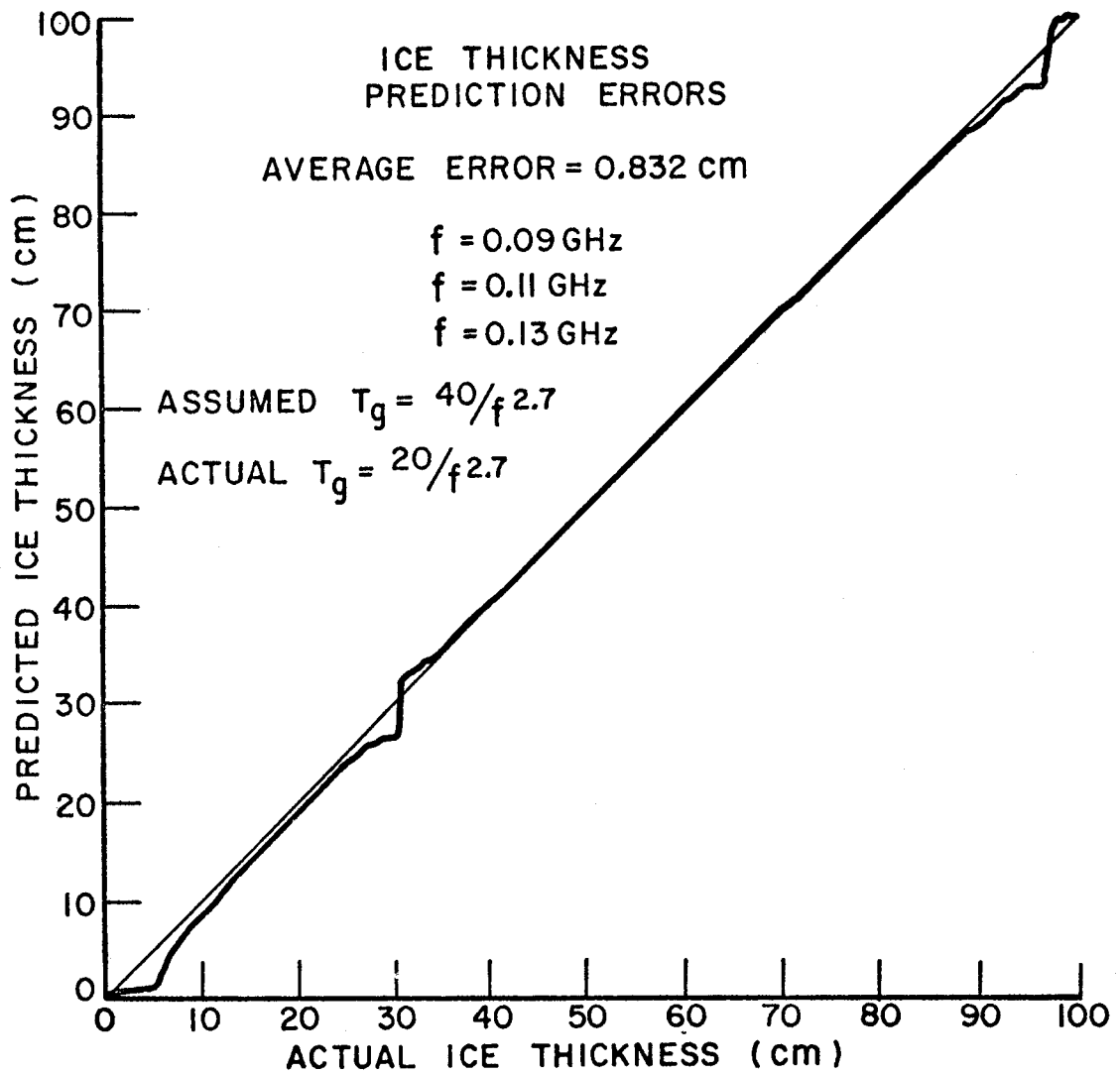
Figure 33. Ice thickness prediction errors using low frequency
one-antenna measurement system; training set calculated
using G = 40, "measurements" made in an environment
having G = 20.
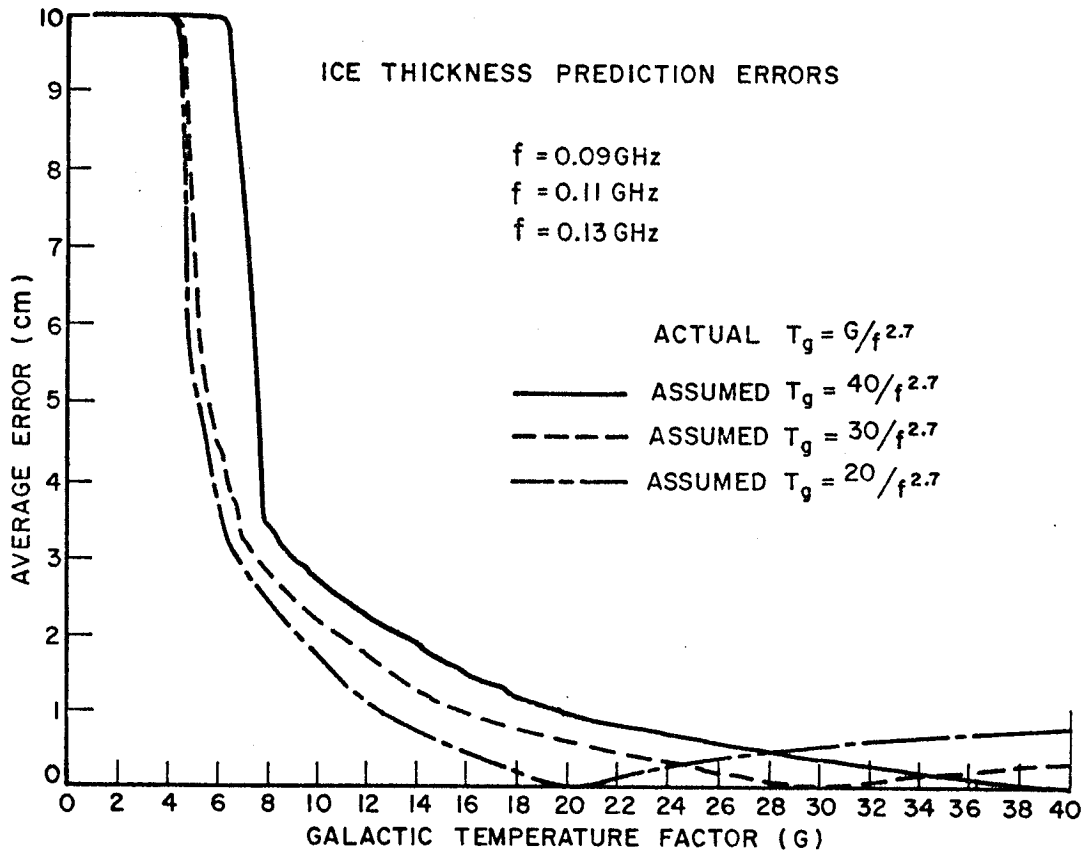
Figure 34. Ice thickness prediction errors using low frequency
one-antenna measurement system; training sets calculated
using G = 40, G = 30, G = 20, "measurements" made in
environment having all possible values of G ($2 \leq G \leq 40$).

of either method deteriorates rapidly if the galactic temperature
factor G decreases below 10 for frequencies around 0.1 GHz.
The design of a suitable airborne antenna for frequencies this
low is a formidable problem which can be greatly alleviated by
going to higher frequencies. At such frequencies (Say f > 300 MHz),
the galactic noise temperature becomes very small, and the apparent
brightness temperature is dominated by the emission from the water -
ice layer system.

2. High Frequency Measurements

It was shown in the preceding section that ice up to a meter
thick could be measured in principle with two or three frequencies
in the 100 MHz region. At these frequencies, however, one must
accommodate a difficult antenna design and a variable cosmic noise
level. Both of these drawbacks are circumvented by going to higher
frequencies (up to 1.0 GHz). This section will be concerned with
data processing methods for temperature measurements made at these
higher frequencies.

A. Minimum - Distance Pattern Classification

From Figure 6 it is seen that for frequencies on the order
of 0.1 GHz the power reflection coefficient, and hence the apparent
brightness temperature, experiences approximately one periodic
oscillation over the span of ice layer thicknesses ranging from 1
cm to 100 cm. If the power reflection coefficient of the frequencies
on the order of 1.0 GHz was plotted in the manner of Figure 29 (a),
it is clear that one would obtain a Lissajous type figure with many
crossover points, giving rise to many ambiguities. Use of such a
training set for identifying two or three dimensional measurement
vectors would not be feasible. It was noted earlier, however, that
the addition of more dimensions to the measurement space tends to
"untie" the intersections in the training set. To be investigated
here, are the number of frequencies required for a satisfactory
thickness estimate consistent with a realistic measurement error,
the size of the frequency sample span, the frequency sample dis-
tribution within the span, and the location of the sample span
within the frequency spectrum.

The training sets are calculated using the theoretical model
for the apparent brightness temperature, i.e. Equation (3-1).
The minimum value of the galactic temperature (G=2) has been
assumed in the training set calculations. (At frequencies of 1.0
GHz or higher, the galactic noise makes an insignificant con-
tribution to the brightness temperature of the ice).

82

In order to simulate systematic errors in the measuring system due to ignorance of such parameters as the actual ice temperature, the exact complex dielectric constant of ice, the effects of small scale surface roughness, uncorrected instrument drift etc., a constant temperature error, ΔT was added to the theoretical temperatures at every frequency. The measurement vectors were then constructed from these "corrupted" theoretical temperature values. The multi-dimensional training set vector is then

$$\begin{bmatrix} S_1 \\ S_2 \\ \cdot \\ \cdot \\ \cdot \\ S_n \end{bmatrix} \qquad (5-11)$$

where the brightness temperature S_k for frequencies f_k is

$$S_k = (1. - |R(f_k,d)|^2)T_i + |R(f_k,d)|^2(T_g(G,f_k) + T_a(f_k)) \quad .$$

$$(5-12)$$

An arbitrary measurement vector is then represented by

$$\begin{bmatrix} M_1 \\ M_2 \\ \cdot \\ \cdot \\ \cdot \\ M_n \end{bmatrix} \qquad (5-13)$$

where

$$M_k = S_k + \Delta T \quad . \qquad (5-14)$$

The minimum distance algorithm is applied just as in the data processing methods of the low frequency measurement section. Each of 199 measurement vectors representing the ice thickness of interest is compared to each of the 199 vectors in the

TABLE 4

Minimum-Distance Pattern Classifiction
(5 K° Constant Temperature Error)

Frequency (GHz)										Average ice Thickness Error (cm)
1.00	1.09									29.198
1.00	1.05	1.09								5.269
1.00	1.03	1.06	1.09							2.003
1.00	1.02	1.04	1.06	1.09						1.962
1.00	1.01	1.02	1.04	1.06	1.09					2.045
1.00	1.01	1.02	1.03	1.04	1.06	1.09				2.289
1.00	1.01	1.02	1.03	1.04	1.05	1.06	1.09			2.289
1.00	1.01	1.02	1.03	1.04	1.05	1.06	1.07	1.09		2.442
1.00	1.01	1.02	1.03	1.04	1.05	1.06	1.07	1.08	1.09	2.402
1.00	1.18									30.073
1.00	1.10	1.18								9.178
1.00	1.06	1.12	1.18							2.875
1.00	1.04	1.08	1.12	1.18						0.148
1.00	1.02	1.04	1.08	1.12	1.18					0.221
1.00	1.02	1.04	1.06	1.08	1.12	1.18				0.181
1.00	1.02	1.04	1.06	1.08	1.10	1.12	1.18			0.148
1.00	1.02	1.04	1.06	1.08	1.10	1.12	1.14	1.18		0.083
1.00	1.02	1.04	1.06	1.08	1.10	1.12	1.14	1.16	1.18	0.113
1.00	1.36									30.957
1.00	1.20	1.36								10.372
1.00	1.12	1.24	1.36							3.178
1.00	1.08	1.16	1.24	1.36						0.246
1.00	1.04	1.08	1.16	1.24	1.36					0.000
1.00	1.04	1.08	1.12	1.16	1.24	1.36				0.000
1.00	1.04	1.08	1.12	1.16	1.20	1.24	1.36			0.000
1.00	1.04	1.08	1.12	1.16	1.20	1.24	1.28	1.36		0.000
1.00	1.04	1.08	1.12	1.16	1.20	1.24	1.28	1.32	1.36	0.000
1.00	1.63									29.186
1.00	1.35	1.63								9.221
1.00	1.21	1.42	1.63							3.877
1.00	1.14	1.28	1.42	1.63						0.786
1.00	1.07	1.14	1.28	1.42	1.63					0.000
1.00	1.07	1.14	1.21	1.28	1.42	1.63				0.000
1.00	1.07	1.14	1.21	1.28	1.35	1.42	1.63			0.000
1.00	1.07	1.14	1.21	1.28	1.35	1.42	1.49	1.63		0.000
1.00	1.07	1.14	1.21	1.28	1.35	1.42	1.49	1.56	1.63	0.000

TABLE 4 (continued)

Frequency (GHz)										Average ice Thickness Error (cm)
1.00	1.90									23.950
1.00	1.50	1.90								12.090
1.00	1.30	1.60	1.90							4.955
1.00	1.20	1.40	1.60	1.90						3.628
1.00	1.10	1.20	1.40	1.60	1.90					2.580
1.00	1.10	1.20	1.30	1.40	1.60	1.90				1.987
1.00	1.10	1.20	1.30	1.40	1.50	1.60	1.90			1.834
1.00	1.10	1.20	1.30	1.40	1.50	1.60	1.70	1.90		1.834
1.00	1.10	1.20	1.30	1.40	1.50	1.60	1.70	1.80	1.90	1.849

TABLE 5

Minimum-Distance Pattern Classification
(5 K° Constant Temperature Error)

Frequency (GHz)										Average ice Thickness Error (cm)
3.00	3.09									28.151
3.00	3.05	3.09								4.995
3.00	3.03	3.06	3.09							2.899
3.00	3.02	3.04	3.06	3.09						3.148
3.00	3.01	3.02	3.04	3.06	3.09					3.425
3.00	3.01	3.02	3.03	3.04	3.06	3.09				3.452
3.00	3.01	3.02	3.03	3.04	3.05	3.06	3.09			3.480
3.00	3.01	3.02	3.03	3.04	3.05	3.06	3.07	3.09		3.342
3.00	3.01	3.02	3.02	3.04	3.05	3.06	3.07	3.08	3.09	3.286
3.00	3.18									28.749
3.00	3.10	3.18								10.754
3.00	3.06	3.12	3.18							8.706
3.00	3.04	3.08	3.12	3.18						0.138
3.00	3.02	3.04	3.08	3.12	3.18					0.221
3.00	3.02	3.04	3.06	3.08	3.12	3.18				0.206
3.00	3.02	3.04	3.06	3.08	3.10	3.12	3.18			0.178
3.00	3.02	3.04	3.06	3.08	3.10	3.12	3.14	3.18		0.095
3.00	3.02	3.04	3.06	3.08	3.10	3.12	3.14	3.16	3.18	0.083
3.00	3.36									24.771
3.00	3.20	3.36								10.209
3.00	3.12	3.24	3.36							10.530
3.00	3.08	3.16	3.24	3.36						0.050
3.00	3.04	3.08	3.16	3.24	3.36					0.013
3.00	3.04	3.08	3.12	3.16	3.24	3.36				0.013
3.00	3.04	3.08	3.12	3.16	3.20	3.24	3.36			0.013
3.00	3.04	3.08	3.12	3.16	3.20	3.24	3.28	3.36		0.013
3.00	3.04	3.08	3.12	3.16	3.20	3.24	3.28	3.32	3.36	0.050
3.00	3.63									33.844
3.00	3.35	3.63								15.013
3.00	3.21	3.42	3.63							4.352
3.00	3.14	3.28	3.42	3.63						0.372
3.00	3.07	3.14	3.28	3.42	3.63					0.307
3.00	3.07	3.14	3.21	3.28	3.42	3.63				0.402
3.00	3.07	3.14	3.21	3.28	3.35	3.42	3.63			0.000
3.00	3.07	3.14	3.21	3.28	3.35	3.42	3.49	3.63		0.025
3.00	3.07	3.14	3.21	3.28	3.35	3.42	3.49	3.56	3.63	0.000

TABLE 5 (continued)

Frequency (GHz)										Average ice Thickness Error (cm)
3.00	3.90									28.407
3.00	3.50	3.90								10.822
3.00	3.30	3.60	3.90							11.538
3.00	3.20	3.40	3.60	3.90						0.997
3.00	3.10	3.20	3.40	3.60	3.90					0.435
3.00	3.10	3.20	3.30	3.40	3.60	3.90				0.435
3.00	3.10	3.20	3.30	3.40	3.50	3.60	3.90			0.435
3.00	3.10	3.20	3.30	3.40	3.50	3.60	3.70	3.90		0.435
3.00	3.10	3.20	3.30	3.40	3.50	3.60	3.70	3.80	3.90	0.435

training set to yield a performance graph similar in form to Figures 28, 30, 33. In this case, only the average ice thickness prediction errors are tabulated here. The results are shown in Table 4 and Table 5. As can be seen from the tables, temperature measurements for an assumed constant temperature error of 5K° at five or more frequencies spanning approximately 0.5 GHz provide good results. A slight deterioration in performance is seen as the sample span is moved to higher frequencies. This is to be expected since the vector locus in the training set has an increasing number of twists, turns, and overlaps.

The calculations, whose results are shown in Table 4 and Table 5, were made assuming a constant measurement error ΔT of 5 K°. As this error increases, it can be expected that the average ice thickness prediction error will also increase. This rate of increase for two different sets of measurements is shown in Table 6. The average ice thickness prediction errors are given for increasing uniform positive errors, increasing uniform negative errors, and increasing errors that alternate in sign from one measurement vector component to another for only the nine frequency measurement set. From these results, it can be seen that the performance in the face of increasing measurement errors is much better for the nine frequency system than for the system that utilizes five temperature measurements in the identification process.

TABLE 6

Minimum-Distance Pattern Classification

Variable Temperature Measurement Errors For A Five Frequency And Nine Frequency System (Normal Incidence)

Measurement	Average Ice Thickness (Error in cm)		
Error ΔT(°K)	2.00(.06)2.24 GHz	2.00(.03)2.24 GHz	
		ΔT	$\Delta T(-1)^i$*
0.0	0.000	0.000	0.000
2.0	0.000	0.000	0.000
4.0	0.040	0.020	0.000
6.0	0.417	0.299	0.000
8.0	1.497	0.580	0.000
10.0	2.643	0.882	0.020
15.0	5.399	1.709	0.630
20.0	9.020	2.633	1.040

* Constant temperature error alternating in sign for each component frequency.

TABLE 6 (continued)

Error $\Delta T(°K)$	2.00(.06)2.24 GHz	2.00(.03)2.24 GHz	
		ΔT	$\Delta T(-1)^{i}$*
-2.0	0.000	0.000	0.000
-4.0	0.040	0.020	0.000
-6.0	0.437	0.281	0.000
-8.0	1.560	0.603	0.000
-10.0	2.872	0.899	0.020
-15.0	6.158	1.641	0.640
-20.0	8.962	2.332	1.060

Clearly, when the errors in ΔT are systematic (of uniform sign for all of the measurement vector components), the predicted thickness errors are considerably larger than when the ΔT errors alternate in sign from one measurement vector component to another since the effects then tend to cancel.

Calculations were also performed to test the performance of this data processing method for various aspect angles and both polarizations. Typical results are shown in Table 7. It was shown earlier in Figure 12, that the power reflection coefficient for vertical polarization at the Brewster Angle shows no dependence on the ice layer thickness so that the identification method fails completely. This is shown clearly in Table 7.

89

TABLE 7

Minimum-Distance Pattern Classification

5 K° Constant Temperature Measurement Error (8 Frequencies)
Variable Angle of Incidence

f = 1.80(.07)2.29 GHz

Aspect Angle	Average Ice Thickness (Error in cm)	
	H.P.	V.P.
0°	0.000	0.000
5°	0.000	0.000
10°	0.000	0.000
15°	1.045	1.201
20°	0.618	1.101
25°	0.000	0.000
30°	0.000	0.000
45°	0.000	0.910
60°	0.000	43.543
75°	0.000	0.003

The data processing approach just described is a simple, brute-force approach which depends on accurate, absolute measurements of the apparent brightness temperature. Thus, it is not well adapted to take into account small deviations in the apparent brightness temperature which may arise for example, from variations in the relative complex dielectric constant of the ice or variations in ice thickness. In the next section, we consider the construction of an alternate training set which will permit a minimum distance algorithm to be applied to ice models of unknown loss tangent, thickness distribution, etc.

B. Fourier Series Fit

It may be seen (from Figure 8, for example) that the reflection coefficient (which controls the brightness at the higher frequencies) is almost a periodic function of frequency for any given ice thickness. Thus the reflection coefficient, or the brightness temperature may be written as a Fourier series in frequency, e.g. at normal incidence

$$T_b(d) = A_0 + \sum_1^\infty A_n \cos n2\pi\tau f + \sum_1^\infty B_n \sin n2\pi\tau f \qquad (5\text{-}15)$$

where the "period" is $1/\tau$ with $\tau = 2d\sqrt{\epsilon_i}/c$. (In fact, τ is the two way propagation time of an impulse through

the ice layer, and the A_i are related to the reflection coefficients for the air-ice and ice-water boundaries. See Chapter II and the Appendix .) The brightness temperature may then be characterized by the parameter τ and the Fourier coefficients A_n. If the brightness were measured at enough frequencies to satisfy the sampling theorem for the thickest ice to be encountered, then the parameter could be unambiguously determined. If, however, fewer frequencies are utilized, then some ambiguities may exist in the estimate of τ with corresponding errors in the estimated thickness.

In the system considered here, the measurement vector is again a set of brighness temperatures on a span of frequencies The thickness estimate is made by assuming a value of thickness, and thus τ, and using the known coefficients A_n to compute the corresponding brightness temperatures, so as to obtain an estimated of the measurement vector for the assumed thickness. The procedure is repeated for all thicknesses (1 cm - 100 cm) and the estimate thickness is taken as that for which the estimated vector is at a minimum distance from the measured vector. The advantage of this procedure is that the effects of varying lossiness or of varying ice thickness can be accommodated by changing the Fourier coefficients. In comparison to the procedures of the next chapter, the method requires considerably more computation. (That is, for each measurement, one might need up to 100 computations of brightness; in practice, one would utilize algorithms to restrict the number of trial thicknesses to a few in the neighborhood of the last thickness estimate, except for initial or ice boundary points). The memory requirements are much less, however, since only a few coefficinets need be stored.

In the calculations reported here, the Fourier coefficients were determined by numerical harmonic analysis of curves such as those in Figure 9 at frequencies high enough that the galactic noise contribution could be considered negligible. Analyzed were curves representing aspect angles of 0°, 15°, and 30° for horizontal polarization and ice layer thicknesses of 10 cm, 50 cm, and 90 cm. The results of the harmonic analysis are given in Table 8. The power reflection coefficient itself is approximately a cosine function, but since the apparent brightness temperature is proportional to $(1 - |R|^2)$, the period of the temperature waveform to be analyzed was defined from one minimum to the next. At frequencies around 1 GHz or higher, the temperature curves are very much like true periodic functions, but not exactly, since, though, the galactic and atmospheric noise contribution is very small compared to the physical temperature of ice, it is not zero. For this reason, the two minimum points on the

apparent brightness temperature curve for defining the period to be analyzed, could not be selected exactly, thus causing small errors in the computed harmonic amplitudes. The B's in Table 8 are the amplitudes of the sine functions in the Fourier series representation and for lossless ice they all should be in principle zero. In Table 8 it can also be seen that the amplitudes of the "dc" term and the first harmonic tend to increase with increasing ice thickness. This is due to the fact that the ice model has small but non zero loss. Only if the ice layer were completely lossless, would the apparent brightness temperature harmonic amplitudes be independent of thickness. The coefficients A_n for the three different thicknesses were averaged, and the B_n were discarded to give the results of Table 9.

TABLE 8

Apparent Brightness Temperature Harmonic Analysis Results*

$$(A_n, B_n \text{ in } °K)$$

$\theta = 0°$	A_0	A_1	A_2	A_3	A_4
d=10 cm	144.53	-52.61	10.18	-1.91	0.39
d=50 cm	145.33	-52.86	10.25	-1.94	0.39
d=90 cm	146.49	-52.98	10.10	-1.92	0.37
$\theta = 15°$					
d=10 cm	142.96	-54.29	11.07	-2.15	0.47
d=50 cm	143.88	-54.57	11.08	-2.19	0.46
d=90 cm	146.50	-54.29	9.62	-1.98	0.24
$\theta = 30°$					
d=10 cm	138.81	-59.57	13.64	-3.04	0.72
d=50 cm	140.31	-59.78	13.15	-3.04	0.62
d=90 cm	140.73	-60.04	13.66	-3.06	0.71

*Based on the ice model of Chapter III, i.e. $\varepsilon_i = 3.21 - j.0009/f$.

TABLE 8 (continued)

θ=0°	B_1	B_2	B_3	B_4
d=10 cm	1.71	-0.31	0.31	0.08
d=50 cm	0.50	-0.09	0.09	0.02
d=90 cm	0.56	-0.16	0.08	0.00
θ=15°				
d=10 cm	2.42	-0.63	0.41	0.04
d=50 cm	0.44	-0.78	0.09	0.02
d=90 cm	-5.56	2.04	-0.61	0.13
θ=30°				
d=10 cm	2.75	-0.91	0.53	-0.01
d=50 cm	3.56	-1.48	0.57	-0.12
d=90 cm	0.81	-0.31	0.14	-0.02

TABLE 9

Averaged Apparent Brightness Temperature Fourier Series Coefficients

	A_0	A_1	A_2	A_3	A_4
θ=0°	145.45	-52.82	10.17	-1.92	0.38
θ=15°	144.44	-54.38	10.59	-2.11	0.39
θ=30°	139.95	-59.80	13.48	-3.02	0.68

Then τ is iterated over values corresponding to ice thickness from 1 cm to 100 cm for each measurement vector, and the minimum-distance criterion of the previous sections is applied at each step to the measurement vector and to the training set vector produced by the Fourier series model. The computation time can be reduced, as mentioned above, by assuming that the iteration of τ can be confined to some region bracketing the thickness of the preceding prediction.

This method was applied to a number of different frequencies, three different scan angles, and different constant temperature errors (both positive and negative) up to 12 K°. The results are shown in Figures 35 (a) to (f) and 36 (a) to (f). For each scan

93
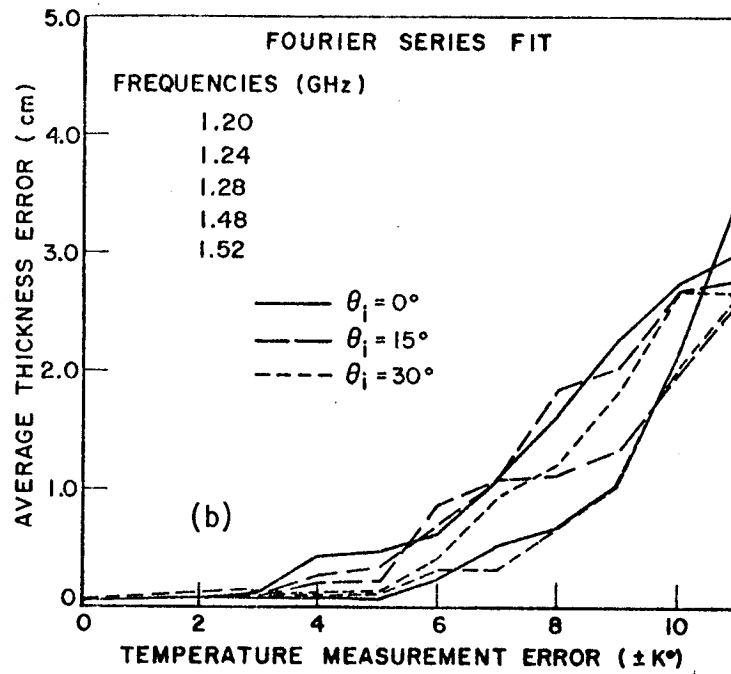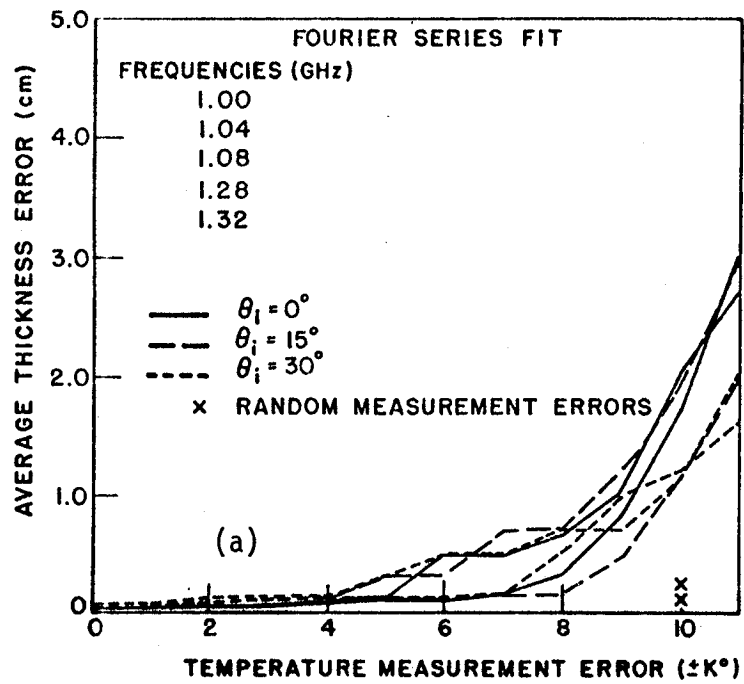
Figures 35 (a-b). Ice thickness prediction errors as a function of measurement errors, using five frequencies.
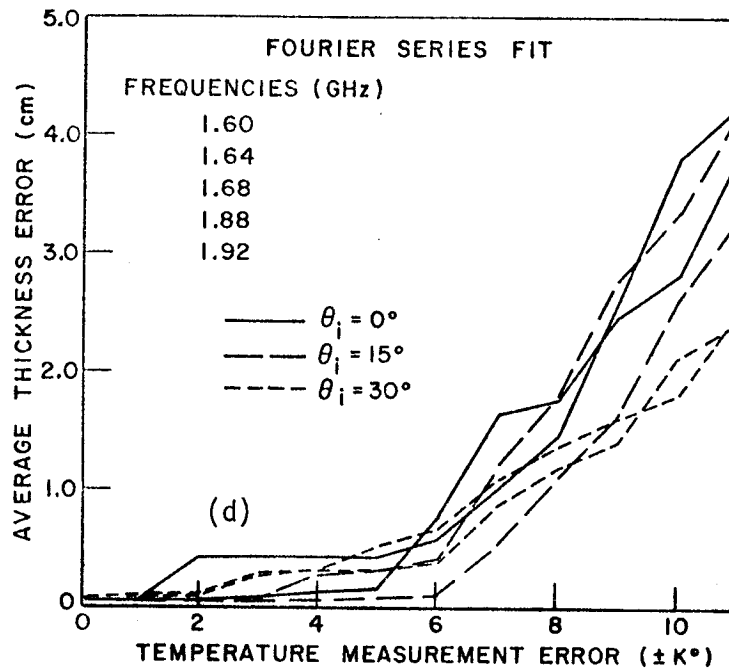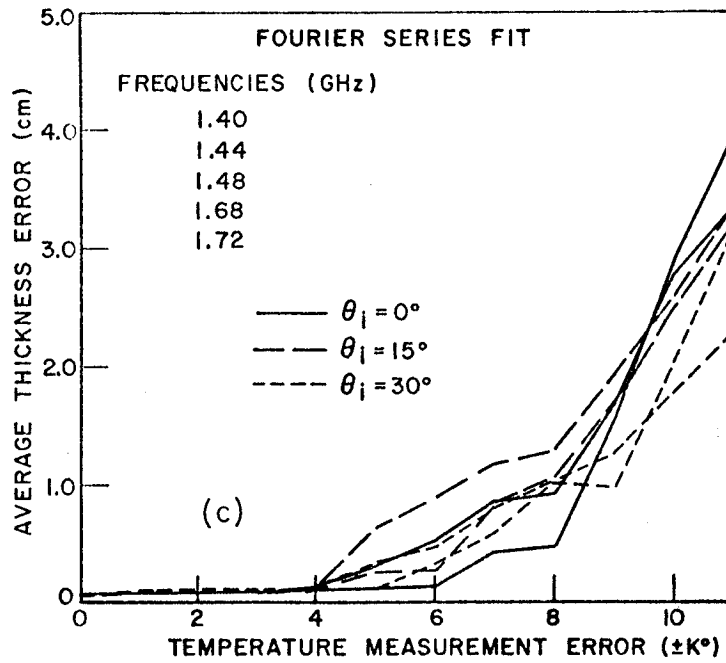
Figures 35 (c-d). Ice thickness prediction errors as a function of measurement errors, using five frequencies.

95
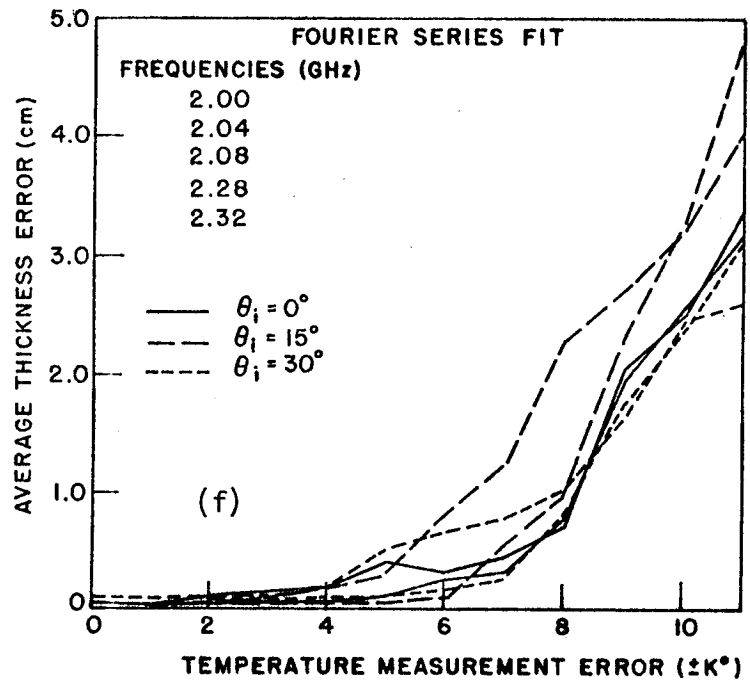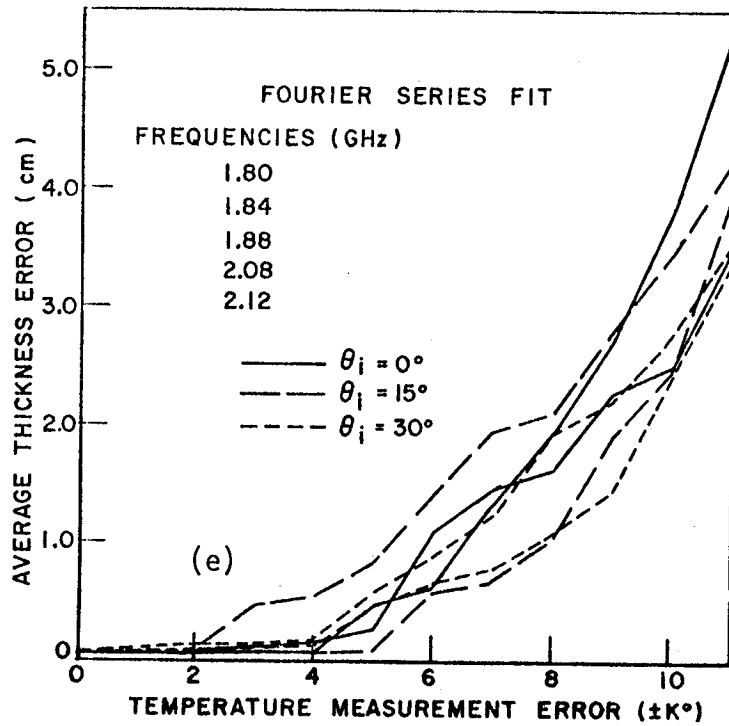
Figures 35 (e-f). Ice thickness prediction errors as a function of measurement errors, using five frequencies.
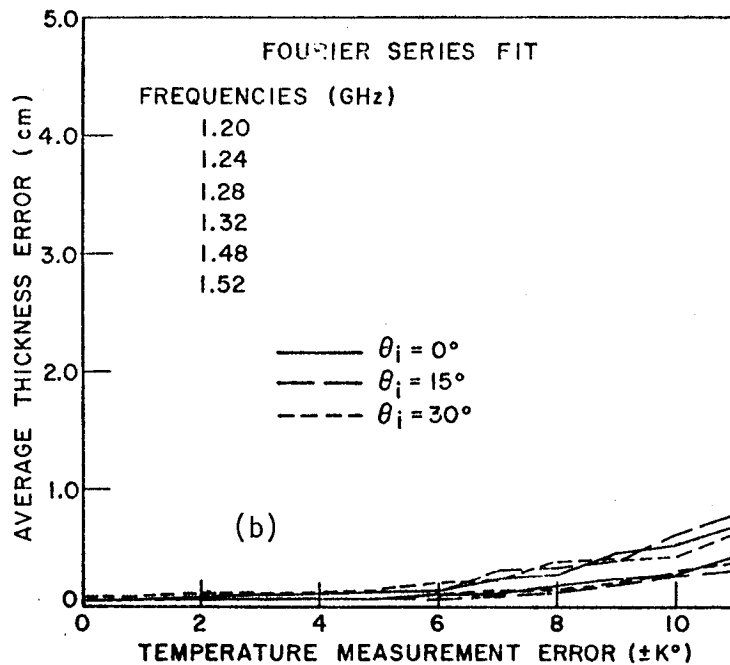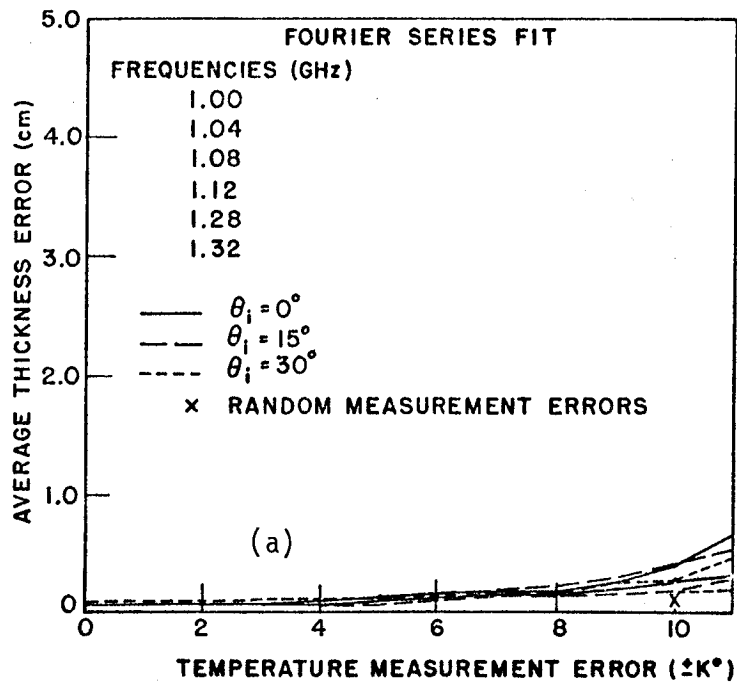
Figures 36 (a-b). Ice thickness prediction errors as
a function of measurement errors,
using six frequencies.
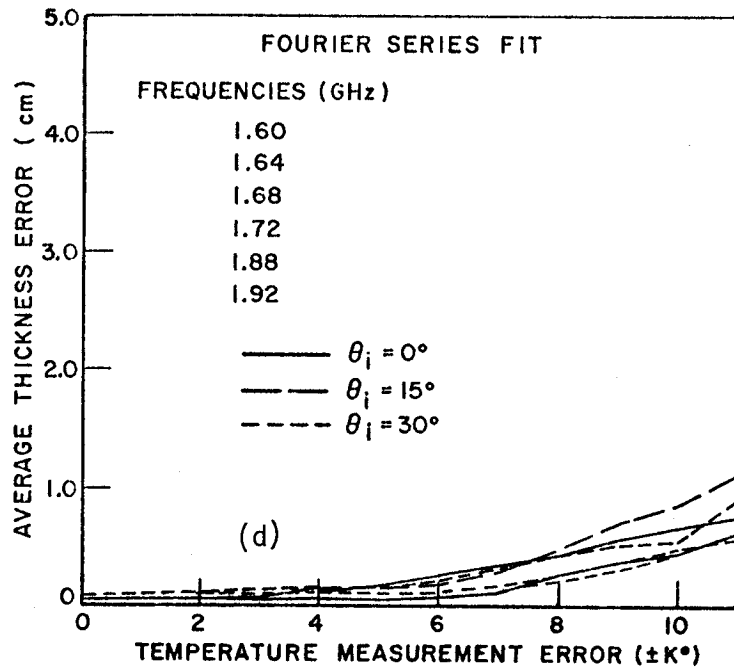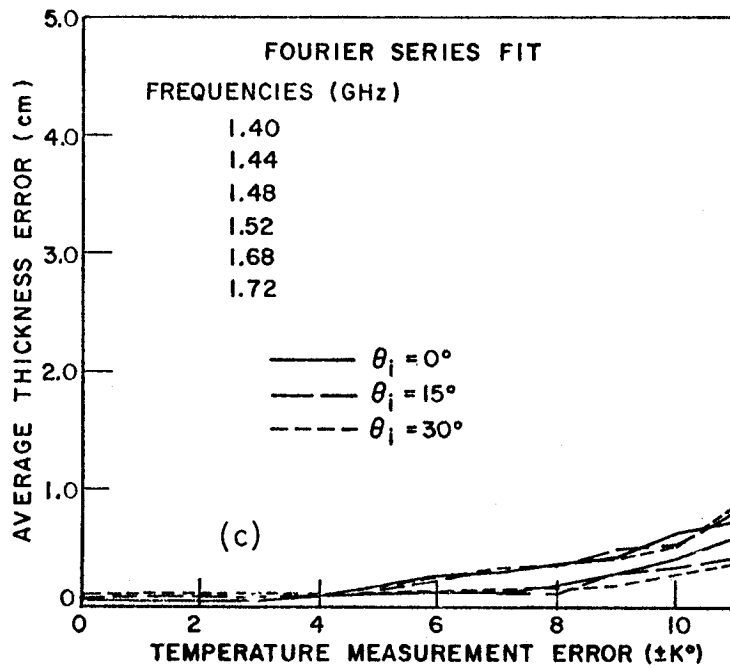
Figures 36 (c-d). Ice thickness prediction errors as a function of measurement errors, using six frequencies.
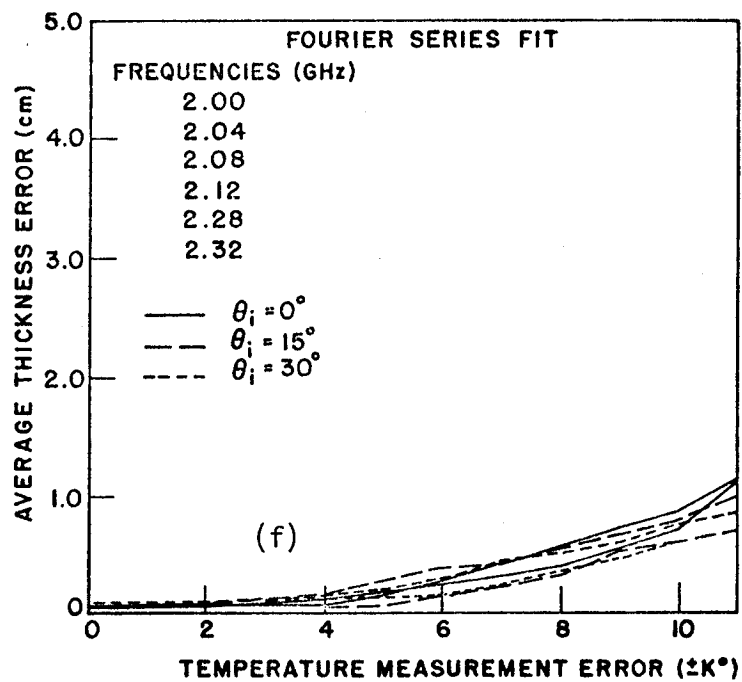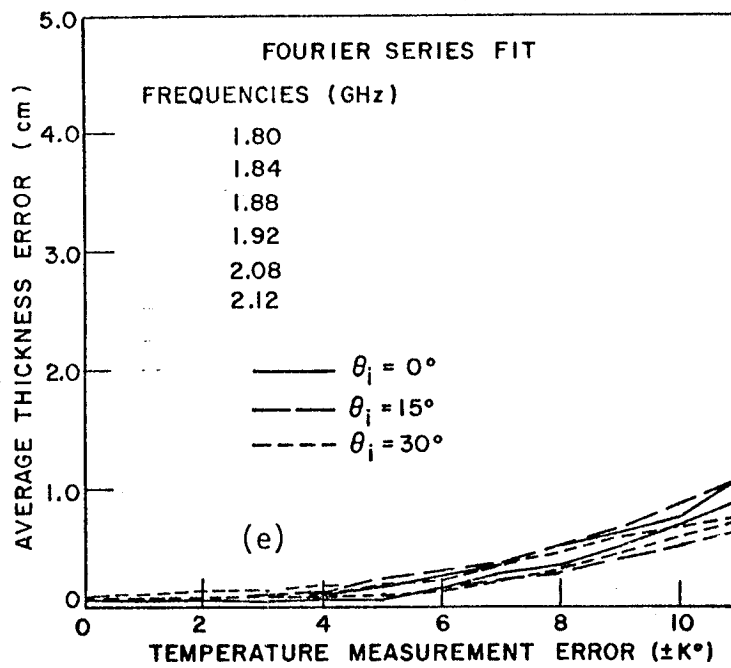
Figures 36 (e-f). Ice thickness prediction errors as a function of measurement errors, using six frequencies.

angle there are two curves. One corresponds to constant positive measurement errors, the other to constant negative measurement errors. The trends in this set of figures are similar to those of the preceding section. If the measurement errors are large (say $10K°$, or more) then the average thickness errors can be reduced by using additional frequencies, as can be seen by comparing Figure 35 (a) and 36 (a), for example. Comparison of Figure 35 (a) with Figure 35 (f) shows that as a given frequency sample set is moved up in frequency, the ice thickness errors increase. If the error ΔT of Equation (5-14) is random with uniform probability distribution between $-10K°$ and $+10K°$ instead of systematic, then the ice thickness errors are greatly reduced, as shown by the location of the X's in Figures 35 (a) and 36 (a). In general, the performance of this data processing method is quite similar to the one of the preceding section, as it should be, since the minimum criterion is the same. The advantage of the method is the ability to iterate over different ice types or thickness distributions by changing the value of the Fourier coefficients. For example, if the ice is multi-layered, the "dc" level remains about the same, but the amplitudes of the remaining harmonics are reduced. On the other hand, (see Figure 27 (b)), one observes that the increased loss due to inclusions in the ice causes the "dc" level to increase and the amplitudes of the harmonics to decrease.

Since such variations in the apparent brightness temperature can easily be accounted for by changing the coefficients A_n, the method can process data from ice with thickness variations on the order of five centimeters, or from ice that has some loss; by iterating over the Fourier coefficients as well as τ, the computation time, however, for the case of very lossy ice (~ 4 db/m) together with large multiple ice thicknesses ($\sim \pm 5$ cm) becomes excessive.

The two high frequency data processing methods presented in this chapter depend heavily upon accurate, absolute apparent brightness temperature measurements. For this reason, they would not be suitable for measuring ice that has high loss and/or large multiple thicknesses, since both conditions cause the apparent brightness temperature to vary considerably. More sophisticated methods are needed to cope with the worst case possibilities in ice conditions. The next chapter presents two such methods.

CHAPTER VI

DATA PROCESSING FOR LOSSY MULTI-THICKNESS ICE

0.   Introduction

If the systems requirement is to measure smooth, clear ice, then the results of the previous chapter show that it is quite feasible to do so with five or six frequencies around 1 GHz or even slightly higher. If however, the measurements must be made over ice which might have inclusions or was of variable thickness, such as that commonly found on the Great Lakes, then the frequency range has to be chosen lower, and more complete data processing methods must be used.

As to the choice of frequency span, consider for example Figures 26 (a) and (b). If there were ± 5 cm multi-thickness present, the apparent brightness temperature would show no dependence on frequency or ice layer thickness at frequencies around 0.75 GHz. Thus, the frequency samples have to be chosen below 0.7 GHz. The upper frequency limit then is set by the multi-layering. The lower limit is set by the distortions in the apparent brightness temperature due to the increasing galactic temperature contribution. For $T_g = 2/f^{2.7}$, the lower limit appears to be about .3 GHz. The assumption of somewhat higher galactic temperatures would increase the lower frequency limit to 0.4 GHz or 0.5 GHz. This then (say 0.3 GHz to 0.75 GHz) is the approximate frequency span available for measurement of lossy, variable thickness ice.

As to the data processing system, the minimum-distance algorithms of the previous chapter were brute force methods that depended on a comparison of accurate absolute measurements of the apparent brightness temperature with a specific training set. Thus, they could not process temperature measurements from ice with losses or multi-layers. Unless such conditions were known in advance, the Fourier Series method could be adapted to handle unknown ice conditions but required much computation time since the training set vectors had to be recomputed for each measurement. This suggests that the Minimum-Distance method should have its training set expanded to range over all expected loss and variable thickness conditions. The memory requirement would be increased, but the computation time would be small, since no recomputation of the training set vectors would be necessary.

101

1. Minimum-Distance Pattern Classification

From the foregoing discussion, it is clear that to measure the thickness of lossy, multi-layered ice, the apparent brightness temperature measurements have to be made at frequencies lower than those considered in the previous chapter. In order to evaluate typical system performances at these lower frequencies, a number of the previous calculations were repeated, still assuming good ice of uniform thickness for the measurement vectors. The constant temperature error ΔT was taken to be $10°K$. The minimum-distance algorithm was used as before. The results of these calculations are shown in Table 10. It can be seen that five temperature measurements at unequally spaced frequencies spanning 0.5 GHz to 0.8 GHz will give acceptable results for constant temperature measurement errors of $10K°$. It has been shown, however, that the variation in the apparent brightness temperature due to losses in the ice or multi-layers can be much greater than $10K°$.

TABLE 10

Average Thickness Errors For Five Frequency System

Minimum Distance Pattern Classification
(10°K Constant Temperature Error, Training Set And
Measurement Set Based on Low Loss Ice of Constant Thickness)

Frequency (GHz)											Average ice Thickness Error (cm)
.50	.51	.52	.53	.54	.55	.56	.57	.58	.59	.60	
X	X	X	X	X							9.925
	X	X	X	X	X						10.563
					X	X	X	X	X		11.045
						X	X	X	X	X	10.661
			X	X	X	X	X				10.690
X		X		X		X		X			7.075
		X		X		X		X		X	7.219
X		X			X			X		X	4.091
X	X				X				X	X	4.907
X				X	X	X				X	6.372
X			X		X		X			X	4.766

Frequency (GHz)											Average ice Thickness Error (cm)
.50	.52	.54	.56	.58	.60	.62	.64	.66	.68	.70	
X	X	X	X	X							7.075
	X	X	X	X	X						7.219
					X	X	X	X	X		7.932
						X	X	X	X	X	7.085
			X	X	X	X	X				7.543
X		X		X		X		X			1.236
		X		X		X		X		X	1.035
X		X			X			X		X	1.050
X	X				X				X	X	2.354
X				X	X	X				X	2.166
X			X		X		X			X	1.420

Frequency (GHz)											Average ice Thickness Error (cm)
.50	.53	.56	.59	.62	.65	.68	.71	.74	.77	.80	
X	X	X	X	X							2.317
	X	X	X	X	X						2.962
					X	X	X	X	X		2.998
						X	X	X	X	X	3.322
			X	X	X	X	X				2.606
X		X		X		X		X			1.219
		X		X		X		X		X	1.216
X		X			X			X		X	1.015
X	X				X				X	X	1.372
X				X	X	X				X	1.196
X			X		X		X			X	0.779

TABLE 10 (continued)

Frequency (GHz)

.50	.54	.58	.62	.66	.70	.74	.78	.82	.86	.90	Average ice Thickness Error (cm)
	x	x	x	x							1.236
	x	x	x	x	x						1.035
x											1.621
		x	x	x	x	x					2.073
		x		x	x	x	x	x			1.096
x											11.472
				x	x	x	x	x		x	10.239
				x	x	x		x		x	2.694
	x			x			x			x	1.952
x			x		x		x		x	x	2.362
x					x		x			x	1.194

Frequency (GHz)

.50	.55	.60	.65	.70	.75	.80	.85	.90	.95	1.00	Average ice Thickness Error (cm)
	x	x	x	x							3.400
	x	x	x	x	x						3.040
x											3.163
		x	x	x	x	x					4.101
		x		x	x	x	x	x			2.799
x											21.156
				x	x	x	x	x		x	21.932
				x	x	x		x		x	8.216
	x			x			x			x	4.822
x			x		x		x		x	x	6.648
x					x		x			x	5.890

A more realistic simulation of system performance, in which the training vectors were based on good ice of constant thickness, and the "experimental" results were based on good ice of variable thickness, is shown in Table 11. For this case, six frequencies were required for reasonably good results. The case of a constant $10K°$ measurement error and ice of uniform thickness has been included for comparison purposes. It can be seen that the addition of the sixth frequency helps to reduce the average error in predicted ice thickness. Note that the thickness variations have been assumed to lie on top of the basic ice layer in this set of calculations. Thus, if a measurement vector is constructed from the apparent brightness temperature for a 70 cm ice layer with 5 cm multi-layers on top, the predicted thickness should be the average of all the layers, i.e. 72.5 cm, or 2.5 cm more than the basic ice layer thickness. (This can be seen in the average thickness predictions in Table 11 when an average ice thickness prediction "error" of 0.5 cm is expected for the 1.0 cm multi-layering, etc..) It is clear that six frequencies can be chosen to give good performance for up to 5 cm of multi-layering, and it is suggestive for system design that best results are usually obtained when the total span of frequencies is as large as possible with the frequencies irregularly (rather than uniformly) spaced. The method fails (with six frequencies) for 10 cm multi-layering. If in addition, the effects of realistic loss tangents were incorporated into the measurement vectors, the performance would deteriorate even more.

The Minimum-Distance method of data processing can be extended to accommodate some of the problems caused by ice of variable loss or thickness by enlarging the training set in the memory. This training set enlargement has been shown schematically in Figure 37, which depicts an array of 9 training sets for three different loss tangents and three different thickness variations ($\pm$ 1 cm to $\pm$ 4 cm). The training set now has 900 six-dimensional vectors, assuming a six frequency system. (In order to minimize storage requirements for the computations to follow, each training set is based on 100 rather than 199 thicknesses in the interval 0 to 100 cm. Clear ice is modeled by ε_i = 3.20 - j.001/f, where f is in GHz. More lossy ice, such as that measured by Vickers (1975), is represented by ε_i = 3.10 - j.04/f and ε_i = 3.00 - j.08/f, corresponding to attenuation of about 1 db/m and 4 db/m respectively.)

If the measurements were taken from one of the nine types of ice in the training set without temperature error, then a perfect fit could be found for each measurement vector. A realistic test of this data processing procedure would be to assume that the ice to be measured was different from any of the

TABLE 11

Average Thickness Errors For Six Frequency System

Minimum Distance Pattern Classification
(Training Set Based on Low Loss Ice-Constant Thickness.
Measurement Set Based on Low Loss Ice-Variable Thickness.)

Frequency (GHz)											Average Ice Thickness Error (cm)			
.50	.51	.52	.53	.54	.55	.56	.57	.58	.59	.60	10 K°	1 cm	5 cm	10 cm
x	x	x	x	x	x						9.621	0.495	10.530	30.294
		x	x	x	x	x	x				9.646	0.495	11.859	30.749
					x	x	x	x	x	x	8.872	0.495	12.568	32.239
x	x	x						x	x	x	6.553	0.495	5.508	32.367
x	x			x	x				x	x	4.819	0.495	4.131	25.997
x		x		x		x		x		x	4.613	0.495	3.766	35.231
x	x	x			x			x		x	4.704	0.495	4.168	34.869

.50	.52	.54	.56	.58	.60	.62	.64	.66	.68	.70	10 K°	1 cm	5 cm	10 cm
x	x	x	x	x	x						4.613	0.495	3.766	35.231
		x	x	x	x	x	x				4.560	0.495	4.794	35.970
					x	x	x	x	x	x	5.025	0.495	5.905	36.525
x	x	x						x	x	x	0.930	0.495	4.178	30.033
x	x			x	x				x	x	0.606	0.495	2.731	34.442
x		x		x		x		x		x	0.422	0.495	2.601	33.239
x	x	x			x			x		x	0.558	0.495	2.550	36.626

TABLE 11 (continued)

107

Frequency (GHz)											Average Ice Thickness Error (cm)			
.50	.53	.56	.59	.62	.65	.68	.71	.74	.77	.80	10 K°	1 cm	5 cm	10 cm
X	X	X	X	X	X						1.178	0.495	2.967	35.460
	X	X	X	X	X	X	X				1.294	0.495	3.691	37.166
				X	X	X	X	X	X	X	1.608	0.495	4.764	35.153
X	X	X						X	X	X	1.146	0.495	4.977	37.457
X	X			X	X				X	X	0.862	0.495	3.033	37.854
X		X		X		X		X		X	0.812	0.495	6.678	23.038
X	X	X			X			X		X	0.101	0.495	2.950	36.412

.50	.54	.58	.62	.66	.70	.74	.78	.82	.86	.90	10 K°	1 cm	5 cm	10 cm
X	X	X	X	X	X						0.422	0.495	2.601	33.237
	X	X	X	X	X	X	X				0.495	0.495	3.626	37.894
				X	X	X	X	X	X	X	0.525	0.495	6.113	38.279
X	X	X						X	X	X	0.407	0.495	4.739	36.945
X	X			X	X				X	X	0.106	0.495	4.420	32.168
X		X		X		X		X		X	7.975	0.495	13.143	22.010
X	X	X			X			X		X	0.131	0.495	3.623	21.839

.50	.55	.60	.65	.70	.75	.80	.85	.90	.95	1.00	10 K°	1 cm	5 cm	10 cm
X	X	X	X	X	X						2.259	0.505	4.000	32.075
	X	X	X	X	X	X	X				1.947	0.505	5.560	35.314
				X	X	X	X	X	X	X	2.068	0.575	9.465	35.804
X	X	X						X	X	X	2.274	0.756	8.405	23.063
X	X			X	X				X	X	2.641	0.505	9.827	28.412
X		X		X		X		X		X	19.892	0.932	23.796	26.942
X	X	X			X			X		X	3.437	0.585	4.286	32.580

ϵ_i
$3.20 - j.001/f$

ϵ_i
$3.10 - j.04/f$

ϵ_i
$3.00 - j.08/f$

2 cm
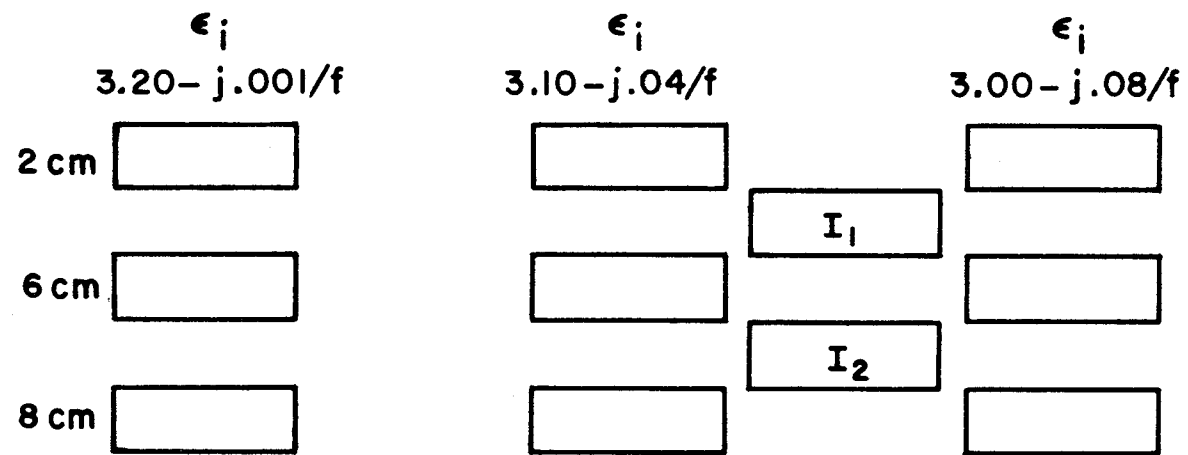
6 cm

8 cm

I_1

I_2

Figure 37.   Enlarged training set used for ice of variable loss
            and thickness.

nine types in the memory and the measurements were then corrupted by some temperature error ΔT.

In the example considered here, the measurement vectors are assumed to come from ice represented by $\varepsilon_i = 3.05 - j.06/f$ with a variable thickness of $\pm$ 2 cm. In Figure 37, this type of ice would be located by the matrix I_j. When arbitrary constant temperature errors were added, it was found that errors appeared in the predicted ice thickness in a random fashion depending on the size of the constant temperature error. These random errors in the predicted ice thickness which occur when there is a systematic measurement error, can be minimized by "randomizing" them. The procedure is to add six different temperature errors ($\pm$ 10K°, $\pm$ 15K°, $\pm$ 20K°) to each measurement vector, make the six corresponding ice thickness predictions, and then take a "vote" among the six different predicted ice thicknesses. By choosing the prediction closest to the average of the six predictions, this method discards, rather than smoothes out, spurious errors, and a typical result is shown in Figure 38.
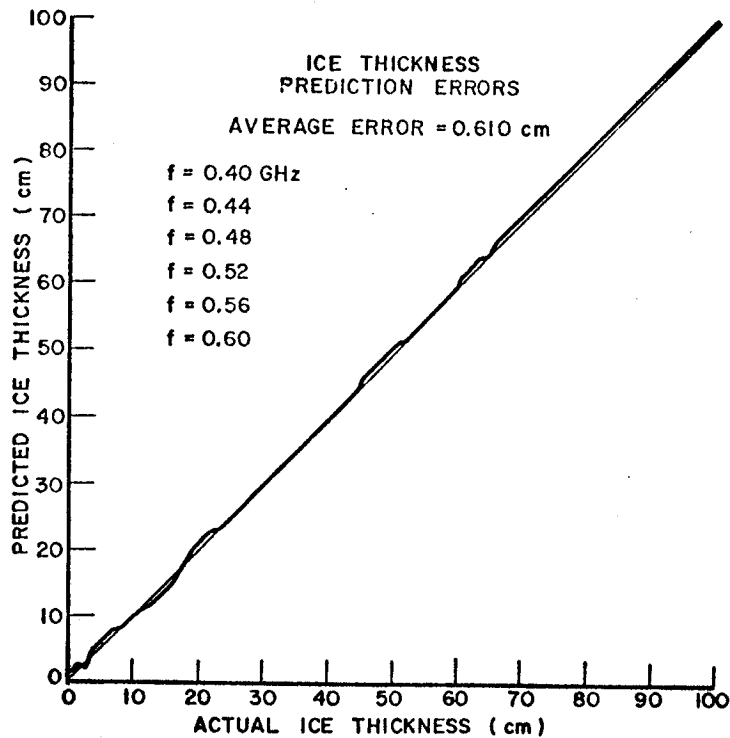
ICE THICKNESS
PREDICTION ERRORS

AVERAGE ERROR = 0.610 cm

f = 0.40 GHz
f = 0.44
f = 0.48
f = 0.52
f = 0.56
f = 0.60

Figure 38. Ice thickness errors using minimum-distance algorithm with expanded training set.

109

This method of data processing obviously requires more storage and computation time but has the advantage of providing some information about the lossiness of the ice and large scale thickness variations.

The existence of constant (i.e. systematic) temperature errors of more than ± 20K° produces a significant deterioration in system performance. The reason, again, is that one is attempting to match absolute brightness chosen from a cosinusoidal variation of brightness with thickness in which the average ("dc") level and the amplitude depend on the thickness variations and the losses in the ice. It would thus be desirable to develop a method of data processing which would depend on the relative brightness in the several frequency channels rather than the absolute brightness temperature.

2. Temperature Quantization

The minimum-distance method of the preceding section can handle systematic temperature errors on the order of ± 15K°, even in the presence of brightness due to changes in the ice properties, but fails for larger errors. To develop a data processing method that is independent of constant measurement errors, one may exploit the fact that the periodicities, and thus the relative levels, of the brightness vs frequency curves are not much affected by losses or multiple thickness effects.

To implement such a system, one must again measure the brightness at a number of different frequencies. At each pair of frequencies, the ice will characterize the fact that the brightness at one frequency is larger, smaller, or equal to the brightness at the other frequency. The result of this decision, or quantization, may now be represented by a ternary number (e.g. "less than" = 0; "greater than" = 1; "equal to" = 2). If n different frequencies are utilized, $n(n-1)/2$ such comparisons may be made, and the "measurement vector" will thus be a sequence of $n(n-1)/2$ ternary numbers. The training sets (one set for each type of ice, i.e. 9 sets for example of Figure 37) will each consist of, say, 100 such sequences, one for each possible thickness between 1 cm and 100 cm. The criterion for a best fit between the measurement vector and a member of the training set is based on the number of matches (rather than some minimum distance) in the two ternary sequences.

In practice, two modifications are needed to successfully implement this scheme. In the first place, to accommodate random errors and to maximize the information content of the sequence, the criterion for "equality" must be modifed to include a "dead-

band" ΔT_a such that temperatures T_1, T_2 are considered "equal" if $|T_1 - T_2| < \Delta T_a/2$. Clearly, as ΔT_a is increased, the number of 2's in the characterizing sequence will increase from almost none to almost all. Secondly, it was found that, in order to minimize the effect of adventitious matches, it was desirable to impose a more stringent criterion for a match. In the algorithm adopted here, a match is considered <u>valid</u> only if the thickness derived from the two best matches are within 2 cm of each other.

In the actual implementation of the procedure, seven frequencies, representing 21 comparisons, were found to give good results. The search for a valid thickness estimate is begun by assuming a particular ΔT_a (in the example of Table 11, the assumed value was $\Delta T_a = 10°K$). The measurement vector based on this ΔT_a is then compared with the training set (based on the same ΔT_a) for one type of ice. If a "valid" match is found, the thickness is taken to be the average thickness of the two best matches. If a valid match is not found, the procedure is repeated for $\Delta T_a = 5°K$, then (if necessary) for $\Delta T_a = 15°K$, and finally (if necessary) for $\Delta T = 2°K$. This procedure either yields a thickness prediction or it does not.

The entire process is repeated for each of the 9 ice types, so that one obtains up to 9 thickness estimates. The final estimate of thickness is made by taking a "vote" i.e. by choosing the thickness most often represented among the nine results.

To illustrate the effectiveness of this system, it was tested for the ice type represented in Figure 37 by matrix I_2 ($\varepsilon = 3.05 - j.06/f$, with thickness variation of ± 3.5 cm). The results are illustrated in Figure 39, which shows the average thickness error. As can be seen from the figure, the random appearance of incorrect thickness prediction has been practically eliminated by the use of the voting procedure.

Although the data storage requirement is rather large (9 x 4800 21 digit ternary numbers for 4 levels of ΔT_a and a 3x3 ice type array), the data processing consists only of simple digit by digit comparisons. Because systematic errors (introduced, for example, by changes in the cosmic background or by calibration drift in the equipment) do not effect this temperature quantization procedure, it appears to be the most useful of those considered.
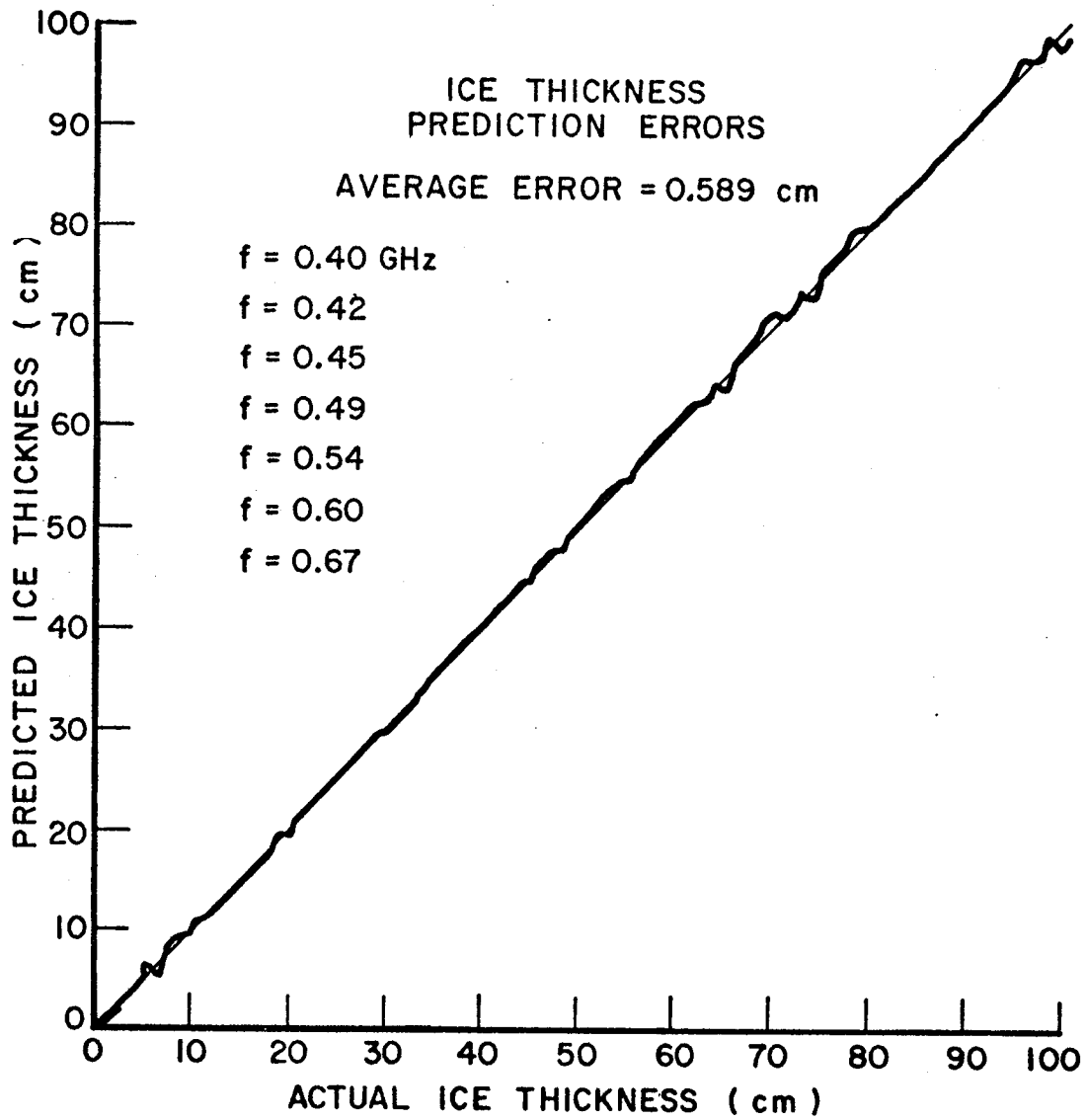
Figure 39. Ice thickness prediction errors using temperature
quantization method with expanded training set.

CHAPTER VII

SEA ICE THICKNESS MEASUREMENT

0. Introduction

There is now considerable interest in the ability to measure the thickness of sea ice. In part, this interest has been generated by results of recent climate models which indicate that the distribution and the amount of sea ice has an important influence on world climate, and in part, because such information is necessary for successful surface and submarine navigation in the polar areas. Many different approaches have been taken towards solving the sea ice thickness measurement problem. They include radar scatterometry, Parashar (1974), side-looking airborne radar, Rouse (1969), radar utilizing holographic principles, Iizuka (1971), satellite IR data analysis, LeSchack (1975), inference of thickness distribution from large scale geophysical properties, Thorndike (1975), and measurement of microwave emissions from aircraft and satellites, Strong (1970), Adey (1972), Gloersen (1972), Wilheit (1972), Campbell (1974), Gloersen (1974), Meeks (1974), Tuiri (1974), Gloersen (1975), Tiuri (1975). Some of these methods and a laser profilometer were combined in a comprehensive measurement program during the passage of the oil tanker Manhattan, Biache (1971). As for qualitative systems, it should be noted that radiometric methods have been used successfully for some time to detect icebergs in the ocean, Ladely (1967), Sperry (1967). A number of both active and passive microwave systems have successfully distinguished between different ice categories (first year, multi-year) without being able to provide quantitative thickness data. The radar system described by Iizuka (1971) can measure sea ice thickness up to 4 cm with 9% accuracy. The radiometric systems at 765 MHz of Adey (1972) and at 600 MHz of Tiuri (1974), (1975) have shown a direct, but qualitative relationship between the apparent brightness temperature and sea ice thickness. It is now clear that the limited quantitative success of most of these systems is due primarily to the complex nature of salt water ice in the natural state.

Since we have shown, in the previous chapters, that it is feasible not only to measure but to map the thickness of fresh water ice layers using radiometric methods, it is natural to applying the same methods to sea ice. Because the electrical properties of sea ice are significantly different from those of fresh water ice, we first review the extensive literature on this subject, before estimating system performance.

1. Literature Review

The primary difference between salt water ice and fresh water ice is the presence of brine which has been trapped in the salt water ice by the freezing pockets. The size, number, and orientation of these pockets are the major source of variability in the properties of sea ice. Furthermore, the brine pockets are not stationary, Kingery (1963). Brine drainage occurs under the influence of gravity through interconnected channels in the ice, and the brine pockets themselves diffuse through the ice toward the warm side (i.e., the bottom of the sea ice layer) under the influence of a temperature gradient. Thus, through these two different mechanisms, the salinity profile of a layer of sea ice will change considerably over a period of time. It is this presence, or absence, of brine in sea ice which makes it possible to distinguish new ice from old ice radiometrically. The higher brine content in the new ice tends to make it more lossy, hence more emissive, thus giving it a higher apparent brightness temperature in the microwave frequencies. An extensive discussion of the radiometric properties of sea ice at X-Band and above has been given by Poe (1972).

The amount of brine entrapped by the freezing process is a function of the rate of freezing. Sea water suddenly exposed to temperatues of -40°C may entrap enough brine to give a 2% salinity, Pounder (1965). By way of comparison, sea water has 3.5% salinity. Usually, young ice has surface salinities of .8% to 1.0%, Bennington (1963). The orientation of the brine inclusions with respect to the incident field is also very important. It has been found that the loss factor changes by as much as a factor of four, depending on the relative orientations of the brine inclusions and the electric field, Sackinger (1972). Sea ice anisotropy has also been measured by Campbell (1974) using a short pulse radar system. Thus, the electrical properties of salt water ice are a function of how fast the ice was frozen, how long it has been frozen, what temperature gradients it has experienced, and the physical orientation of the brine pockets with respect to the electric field. An additional variable is the physical temperature of ice at the time of measurement. This, in part, may explain the great variation in reported loss measurements of salt water ice. Furthermore, most of the results to date come from laboratory measurements made on artificial sea ice water, and it is possible that the laboratory-grown ice does not represent accurately sea ice in the natural state because of slightly different brine distributions.

To illustrate the great range of loss values possible, some of the results reported in the literature, Cook (1960), Iglesias (1967), Addison (1969), Gudmandsen (1971), Hoekstra (1971), Iizuka (1971) are listed in Table 12.

TABLE 12

SALT WATER ICE PROPERTIES

f(GHz)	db/m	Ref	°C	Salinity %
.10	26.	Addison (1969)	-12.5	0.512
.10	4.1	Addison (1969)	-33.	0.512
.10	23.	Addison (1969)	-15.	1.25
.10	7.7	Addison (1969)	-35.	1.25
.10	20.	Addison (1969)	-15.	1.58
.10	7.1	Addison (1969)	-35.	1.58
.10	23.	Cook (1960)	-10.	0.70
.10	0.75	Cook (1960)	-40.	0.70
.10	10.	Cook (1960)	-10.	0.35
.10	0.77	Cook (1960)	-40.	0.35
.45	.62	Gudmandsen (1971)	-20.	0.2
.45	55.0	Gudmandsen (1971)	-20.	0.4
.50	108.	Hoekstra (1971)	-10.	0.8
1.00	135.	Hoekstra (1971)	-10.	0.8
1.00	2.01	Iglesias (1967)	-1.	0.002
1.00	0.06	Iglesias (1967)	-60.	0.002
2.00	129.	Hoekstra (1971)	-10.	0.8
10.00	120.	Gudmandsen (1971)	-20.	0.4

These losses are reported in many forms, e.g. nepers/m, db/m, loss tangent, imaginary part of the complex dielectric constant; so for ease of comparison, all the results have been converted to db/m. In some cases, an assumption had to be made regarding the real part of the complex dielectric constant. It is clear from the table that there is a very large variation in the reported results, but that in general the losses are significantly higher than those found for fresh water ice.

Another complication in the salt water/salt ice system is the nature of the boundary between the water and the ice layer. In fresh water this boundary usually is well defined. In laboratory experiments on salt water freezing, it has been found that icicles grow downward from the ice layer into the water, Palosuo (1963). These icicles tend to form an impedance matching layer between the ice and the water. Thus, the oscillations in the apparent brightness temperature due to interference between the two boundaries would be further reduced. Other complications, such as small and large scale roughness on the top surface and air inclusions and cracks in the ice layer make quantitative interpretation of apparent brightness temperatures of sea ice even more difficult.

2.   Apparent Brightness Temperature Calculations

Because of the large attenuation likely to be encountered in sea ice, one would expect that the ripples in the apparent brightness temperature would be highly damped, and the brightness temperature would increase assymptotically to some value given by the product of the ice emissivity and the physical temperature of the ice. A number of calculations have been made using the apparent brightness model developed previously with representative values of attenuation for the ice and assuming a salinity of 35 ppt for the underlying sea water.

Note that, for the frequency ranges considered here (0.1 GHz to 2.0 GHz), the complex dielectric constant of fresh water does not change much, whereas, for typical sea water (salinity $\sim$ 35 ppt), the imaginary part of the complex dielectric constant increases rapidly at low frequencies due to the ionic conductivity of the dissolved salts. (See Figures 40 (a) and 40 (b)). Representative values of the dielectric constant and the power reflection coefficient of fresh and salt water are given in Table 13.

TABLE 13

REFLECTION COEFFICIENT OF FRESH AND SALT WATER

	s=0 ppt		s=35 ppt	
	ε_w	$\|R\|^2$	ε_w	$\|R\|^2$
f=0.1GHz	87.7-j0.9	0.651	75.6-j523.2	0.877
f=1.0GHz	86.7-j9.1	0.651	74.8-j59.7	0.679

116
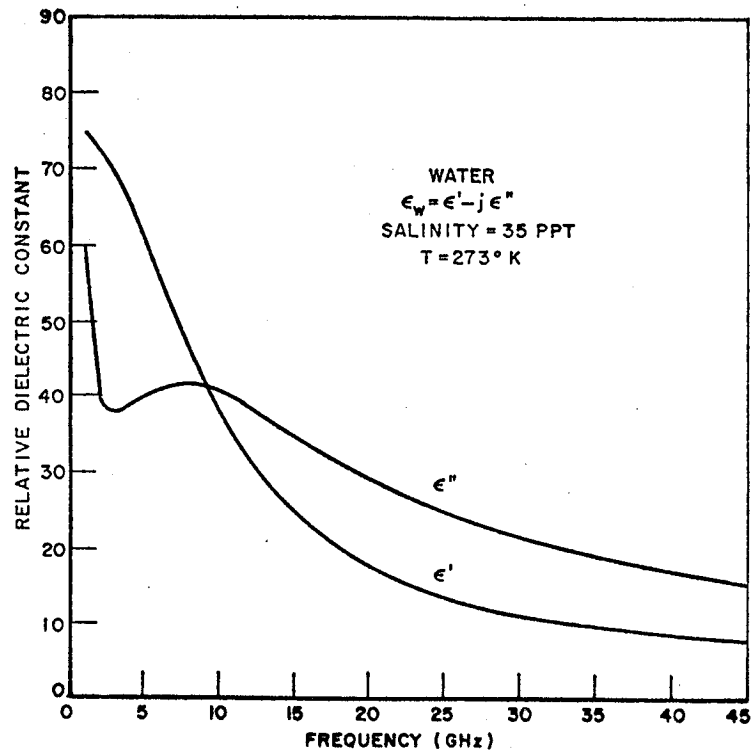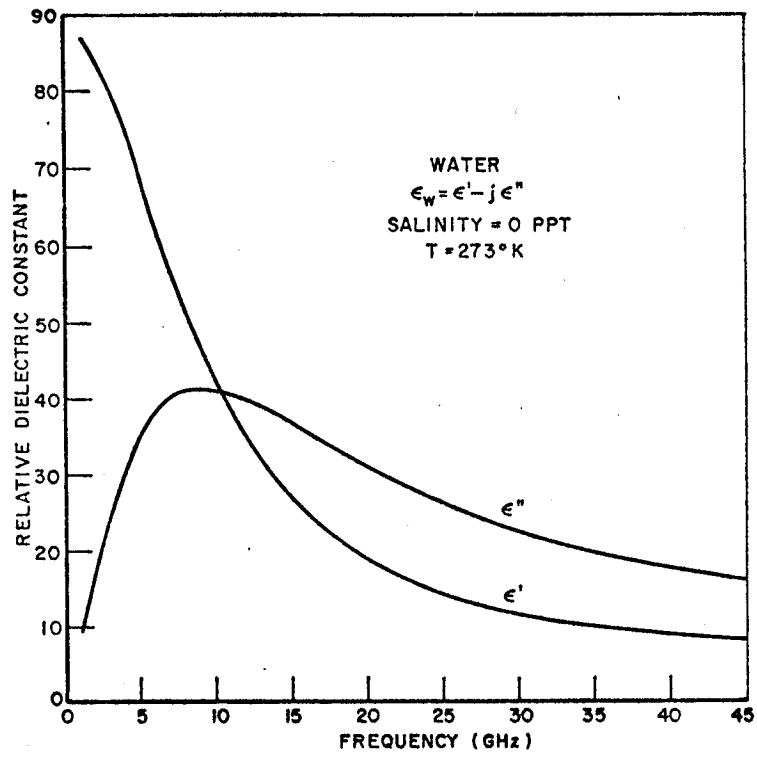
Figures 40 (a-b). Relative complex dielectric constant of fresh and salt water.

117

The power reflection coefficient as a function of ice thickness, with ice attenuation as parameter, is shown in Figures 41 (a), (b), (c), (d), and (e). The corresponding apparent brightness temperatures are shown in Figures 42 (a), (b), (c), (d), and (e). From this set of figures, it can be seen that if the ice has an attenuation of approximately 8 db/m or less, the temperature quantization method of data processing could be utilized to measure ice thickness up to a meter. If the attenuation is more than 32 db/m for example, only ice layers less than 10 cm to 20 cm thick could be success-fully measured by any data processing method that relied on estimates of the period of oscillation of the brightness. In practice, the tolerable attenuations are even less, since actual sea ice would probably exhibit considerable surface texture, some variability in thickness, and an ill-defined transition layer between the ice and the water. All three of these conditions tend to smooth out the ripples in the apparent brightness temperature.
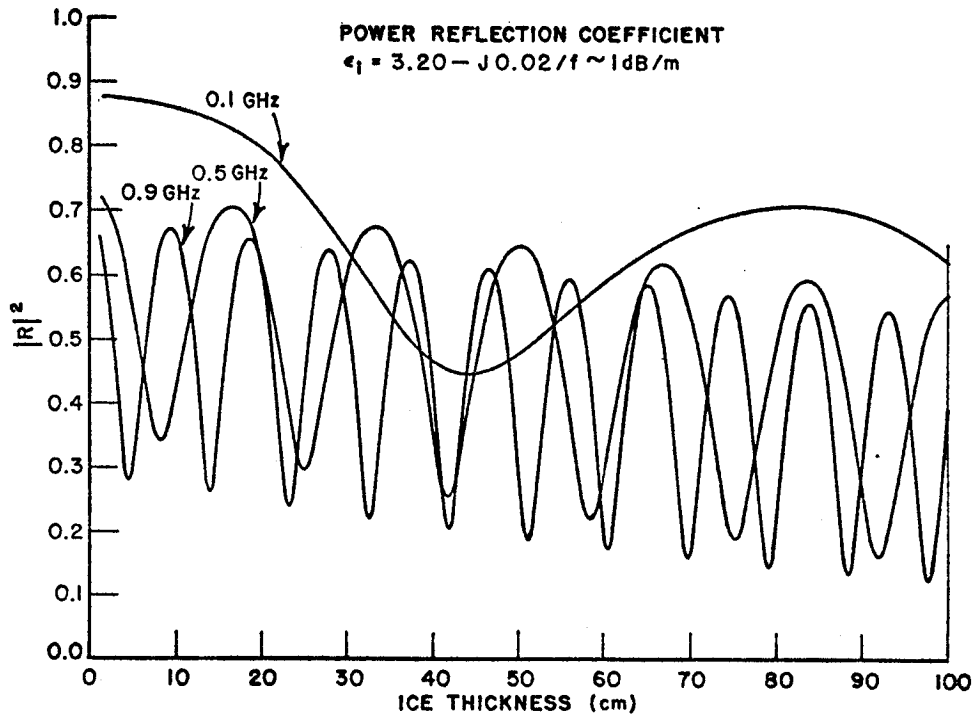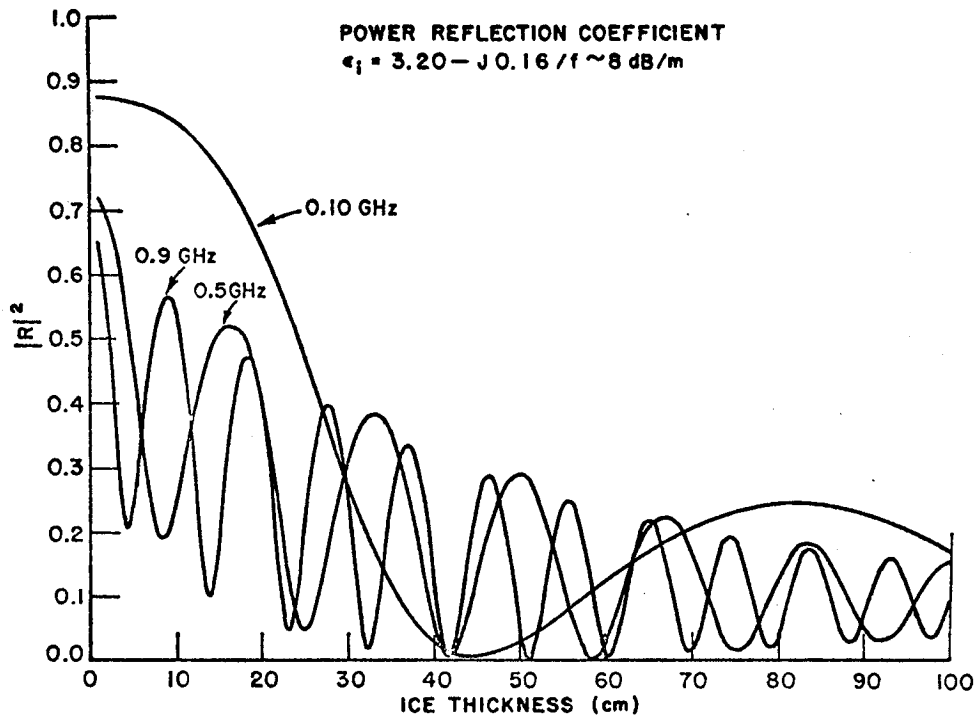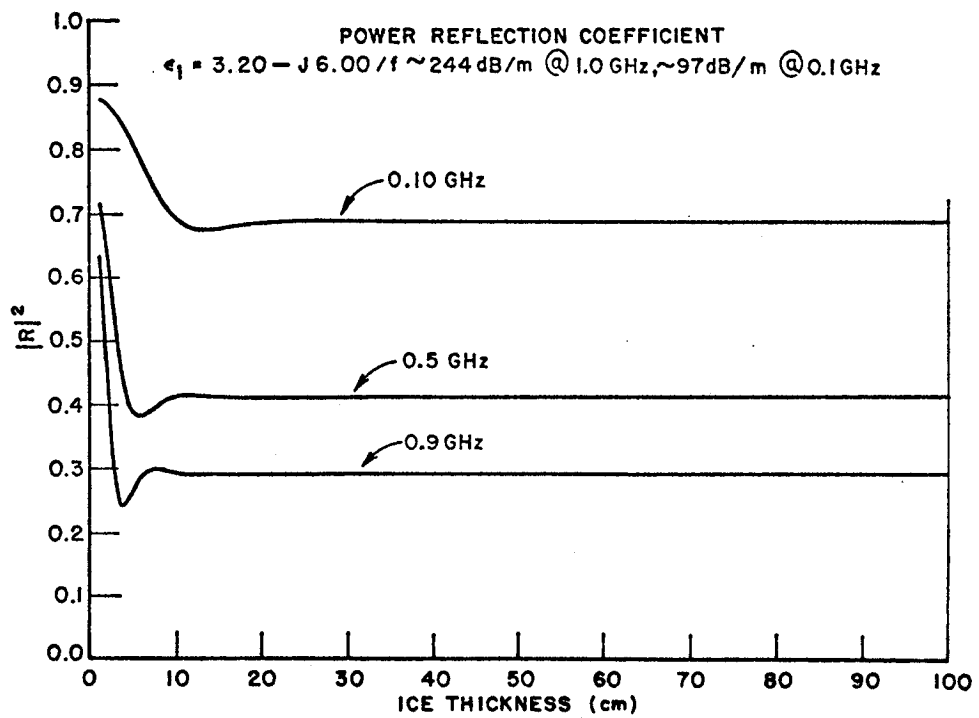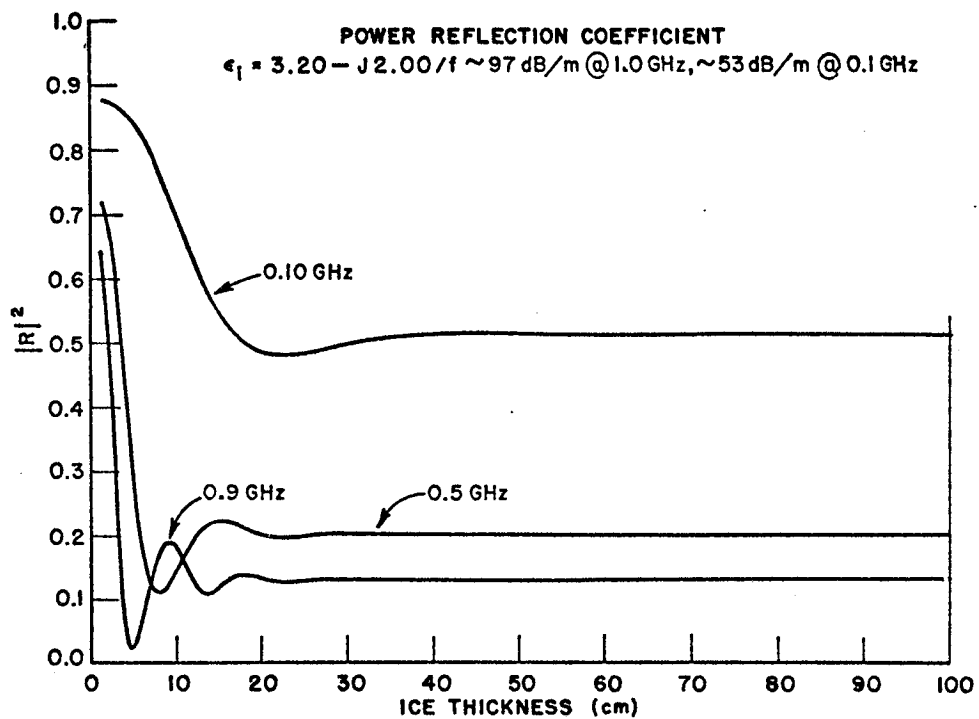

Figure 41 (a). Power reflection coefficient as a function of ice thickness and ice loss. Salinity of water = 35 ppt.
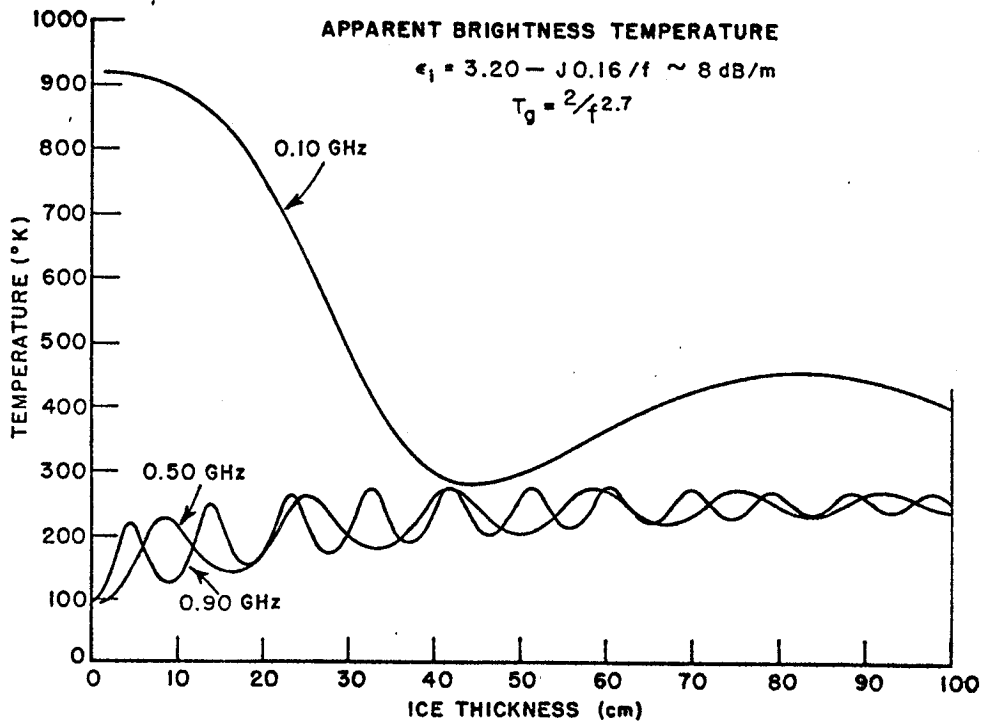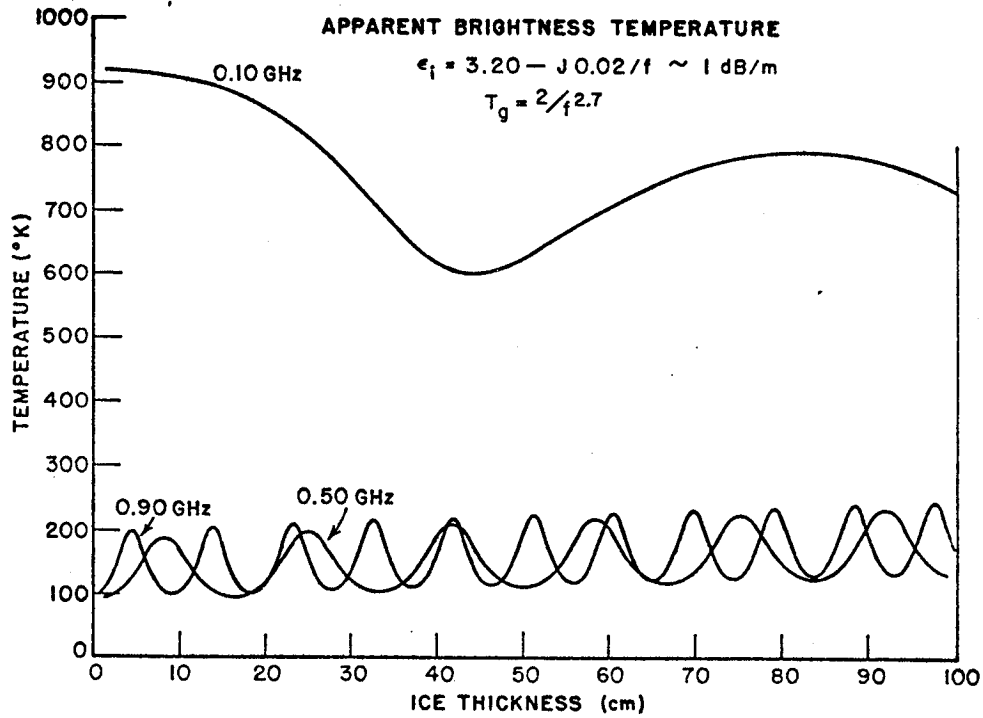
118
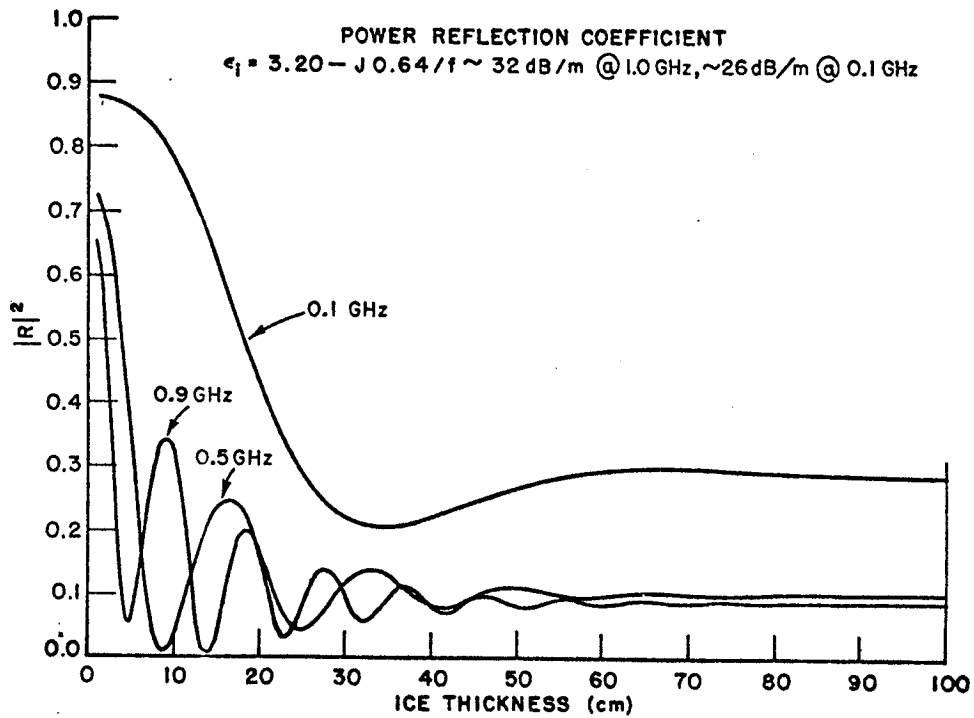
Figures 41 (b-c). Power reflection coefficient as a function of ice thickness and ice loss. Salinity of water = 35 ppt.

POWER REFLECTION COEFFICIENT
$\epsilon_1 = 3.20 - J2.00/f \sim 97\,dB/m$ @ 1.0 GHz, $\sim 53\,dB/m$ @ 0.1 GHz

0.10 GHz

0.9 GHz   0.5 GHz

$|R|^2$ (vertical axis)

ICE THICKNESS (cm) (horizontal axis)

POWER REFLECTION COEFFICIENT
$\epsilon_1 = 3.20 - J6.00/f \sim 244\,dB/m$ @ 1.0 GHz, $\sim 97\,dB/m$ @ 0.1 GHz

0.10 GHz

0.5 GHz

0.9 GHz

$|R|^2$ (vertical axis)

ICE THICKNESS (cm) (horizontal axis)

Figures 41 (d-e). Power reflection coefficient as a function of ice
thickness and ice loss. Salinity of water = 35 ppt.

120

Figures 42 (a-b). Apparent brightness temperature as a function of ice thickness and ice loss. Salinity of water = 35 ppt.
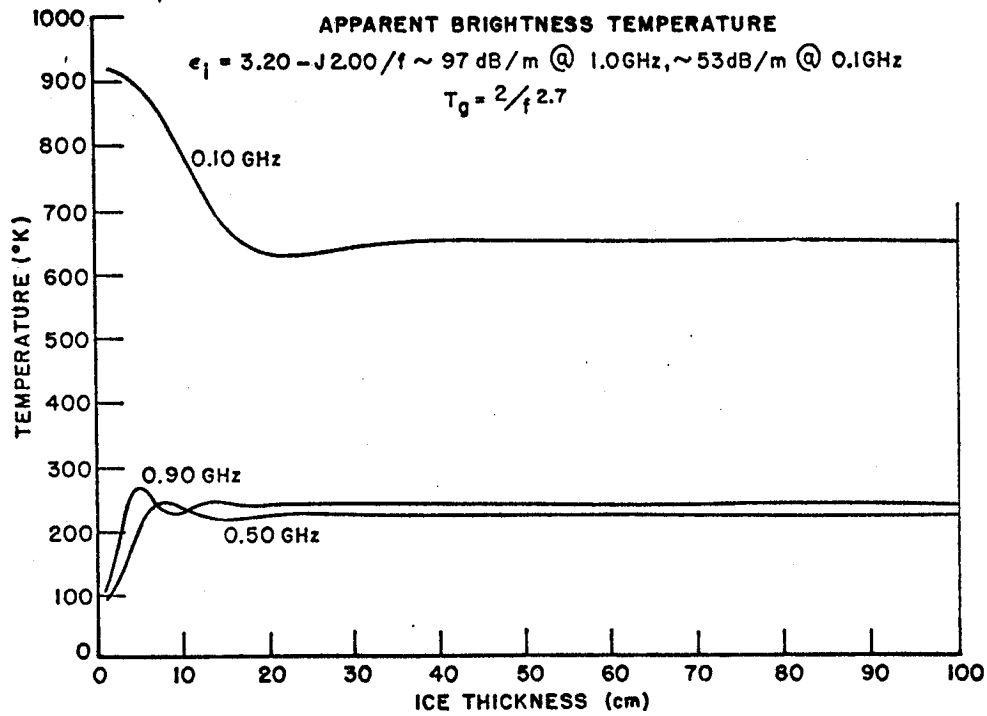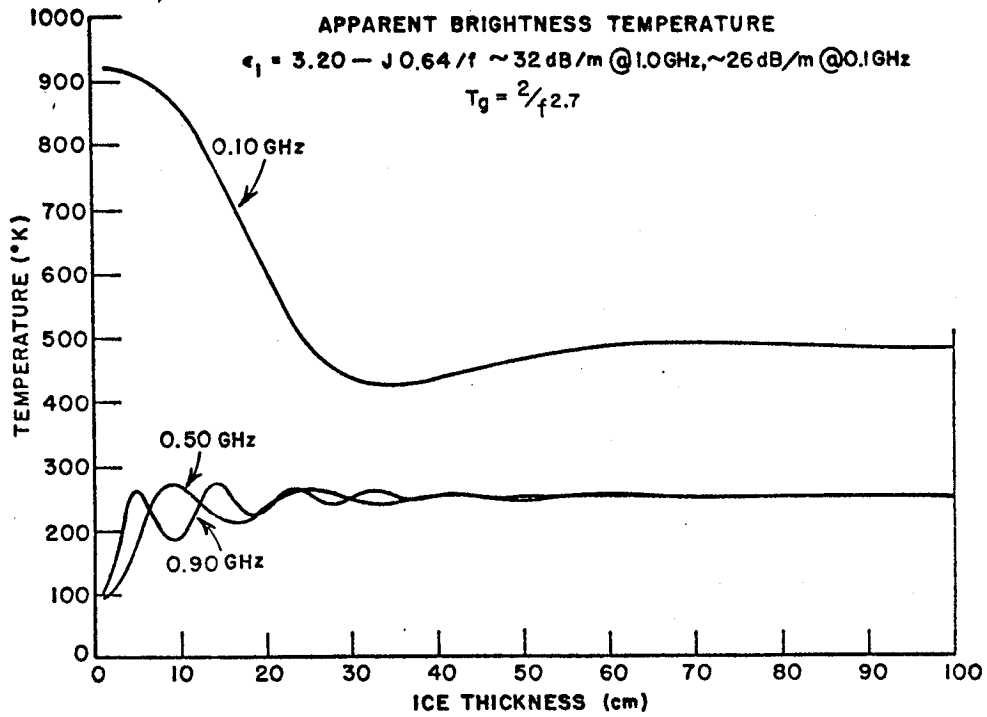
Figures 42 (c-d). Apparent brightness temperature as a function of
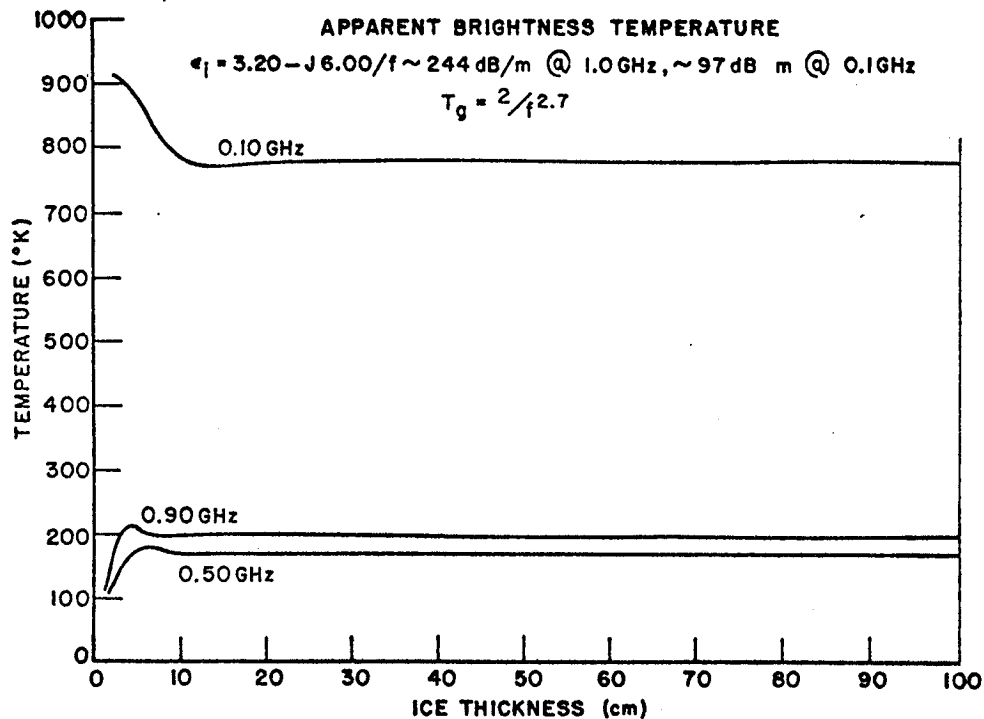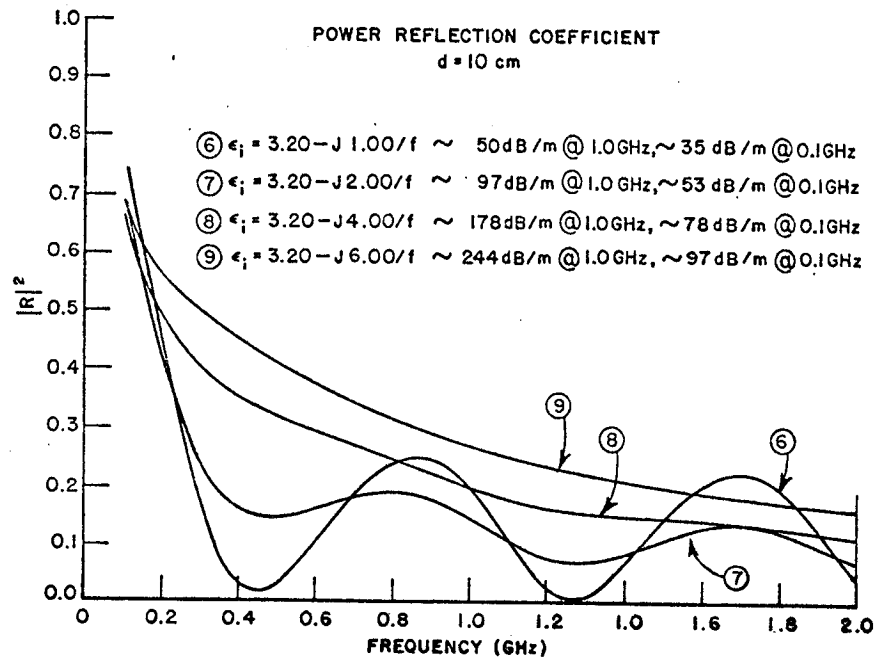ice thickness and ice loss. Salinity of water
= 35 ppt.

122

APPARENT BRIGHTNESS TEMPERATURE

$\epsilon_i = 3.20 - j\,6.00/f \sim 244\,dB/m$ @ $1.0\,GHz, \sim 97\,dB$ m @ $0.1\,GHz$

$T_g = {}^2\!/_f{}^{2.7}$

Figure 42 (e). Apparent brightness temperature as a function of ice thickness and ice loss. Salinity of water = 35 ppt.
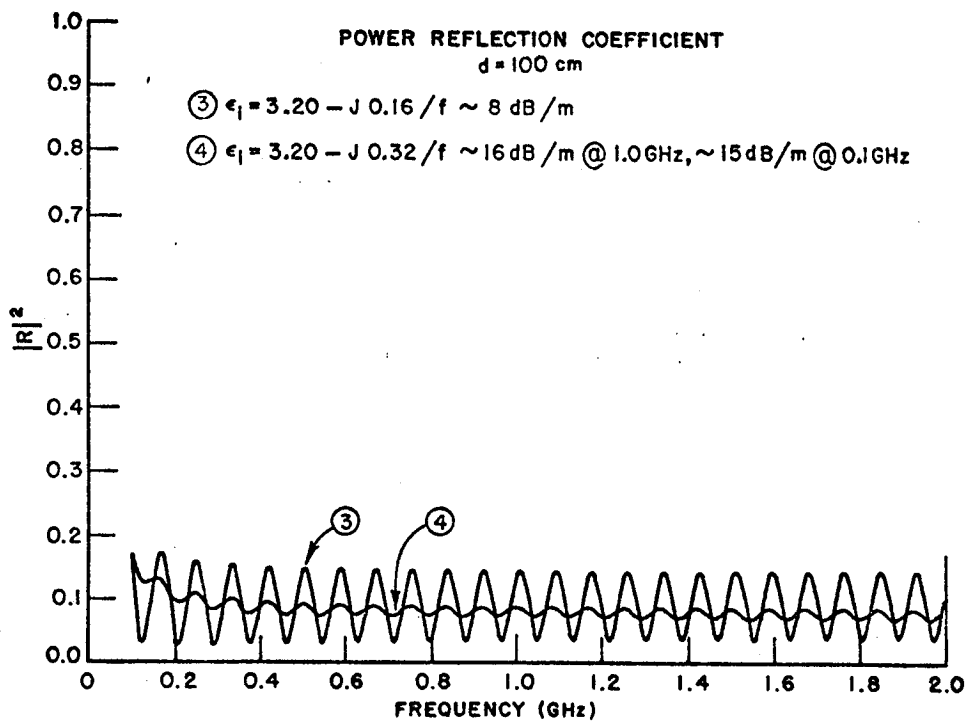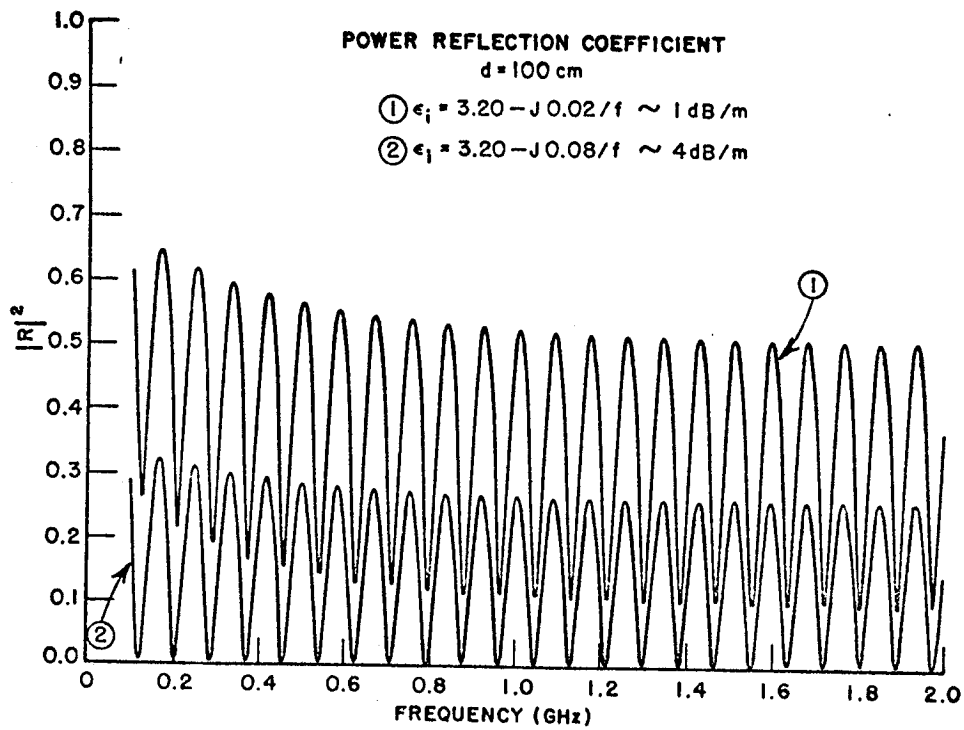
The change in the power reflection coefficient (as a function of frequency) with increasing attenuation is shown in Figures 43 (a) and (b) for a 10 cm ice layer and in Figures 44 (a), (b), and (c) for a 100 cm ice layer. The apparent brightness temperatures corresponding to these power reflection coefficients are shown in Figures 45 (a) and (b) and 46 (a), (b), and (c). This set of figures offers further evidence that no more than 8 db/m attenuation can be tolerated if ice thicknesses up to a meter are to be measured by the methods considered here.

For very high loss, the apparent brightness temperature changes almost monotonically from that for sea water to that for thick ice. Thus, if the attenuation were known to be high, a measurement of brightness temperature at one or two frequencies would provide a fairly good estimate of thickness directly. However, once the total attenuation through the layer (i.e. the product of attenuation and thickness) reaches 15 db or so, the thickness has almost no influence on the reflection coefficient. Thus, the brightness which is then determined by the

dielectric properties and physical temperature of the ice, not its thickness. Thus, the single frequency systems (Tiuri (1975), Adey (1972)) in the 600 MHz - 800 MHz show the expected relation between increasing brightness and increasing thickness, but can only provide qualitative estimates of the actual thickness.
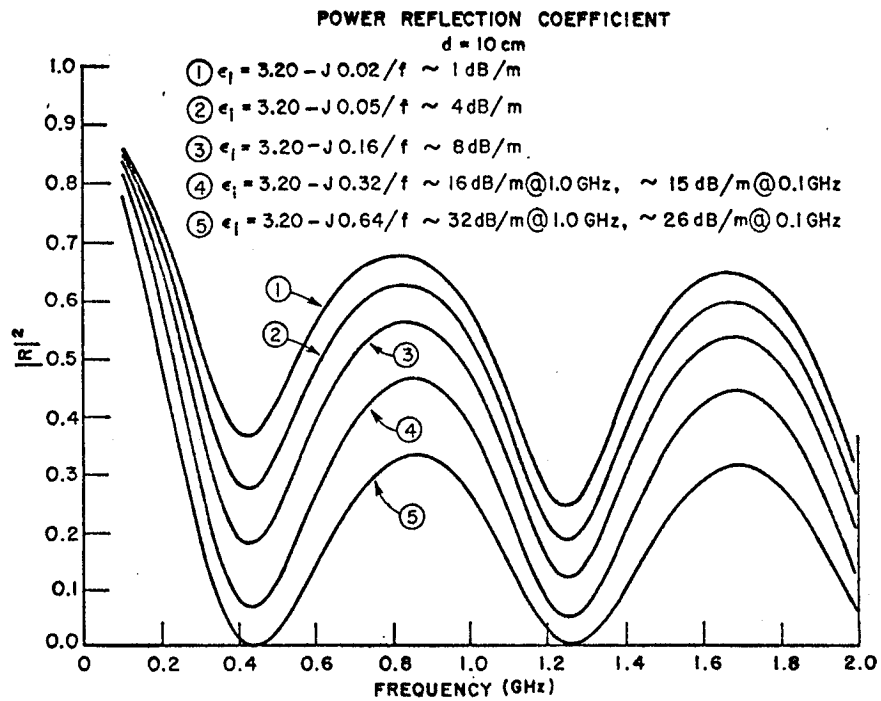
Figures 43 (a-b). Power reflection coefficient as a function of frequency and ice loss. Ice Thickness = 10 cm, water salinity = 35 ppt.

125

Figures 44 (a-b). Power reflection coefficient as a function of frequency and ice loss. Ice thickness = 100 cm, water salinity = 35 ppt.
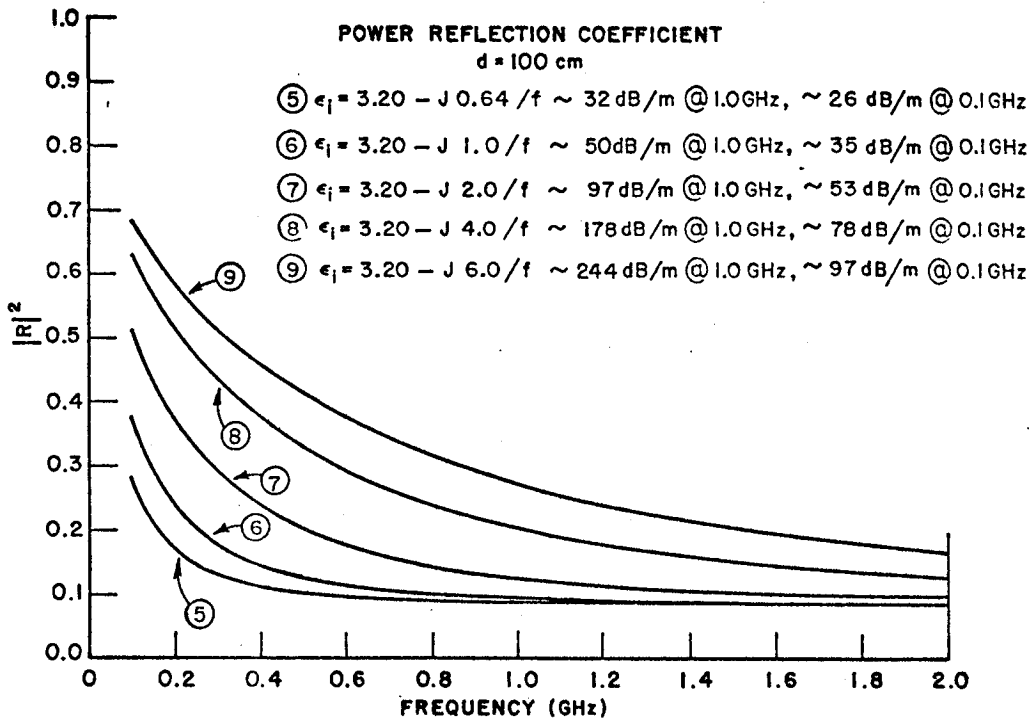
126

POWER REFLECTION COEFFICIENT
d = 100 cm

⑤ ϵ_i = 3.20 − J 0.64 /f ~ 32 dB/m @ 1.0 GHz, ~ 26 dB/m @ 0.1 GHz

⑥ ϵ_i = 3.20 − J 1.0/f ~ 50 dB/m @ 1.0 GHz, ~ 35 dB/m @ 0.1 GHz

⑦ ϵ_i = 3.20 − J 2.0/f ~ 97 dB/m @ 1.0 GHz, ~ 53 dB/m @ 0.1 GHz

⑧ ϵ_i = 3.20 − J 4.0/f ~ 178 dB/m @ 1.0 GHz, ~ 78 dB/m @ 0.1 GHz

⑨ ϵ_i = 3.20 − J 6.0/f ~ 244 dB/m @ 1.0 GHz, ~ 97 dB/m @ 0.1 GHz

Figure 44 (c). Power reflection coefficient as a function of frequency and ice loss. Ice thickness = 100 cm, water salinity = 35 ppt.

APPARENT BRIGHTNESS TEMPERATURE
$T_g = 2/f^{2.7}$
d = 10 cm

① ϵ_i = 3.20 − J 0.02/f ~ 1 dB/m

② ϵ_i = 3.20 − J 0.08/f ~ 4 dB/m

③ ϵ_i = 3.20 − J 0.16/f ~ 8 dB/m

④ ϵ_i = 3.20 − J 0.32/f ~ 16 dB/m @ 1.0 GHz, ~ 15 dB/m @ 0.1 GHz

⑤ ϵ_i = 3.20 − J 0.64/f ~ 32 dB/m @ 1.0 GHz, ~ 26 dB/m @ 0.1 GHz

Figure 45 (a). Apparent brightness temperature as a function of frequency and ice loss. Ice thickness = 10 cm, water salinity = 35 ppt.
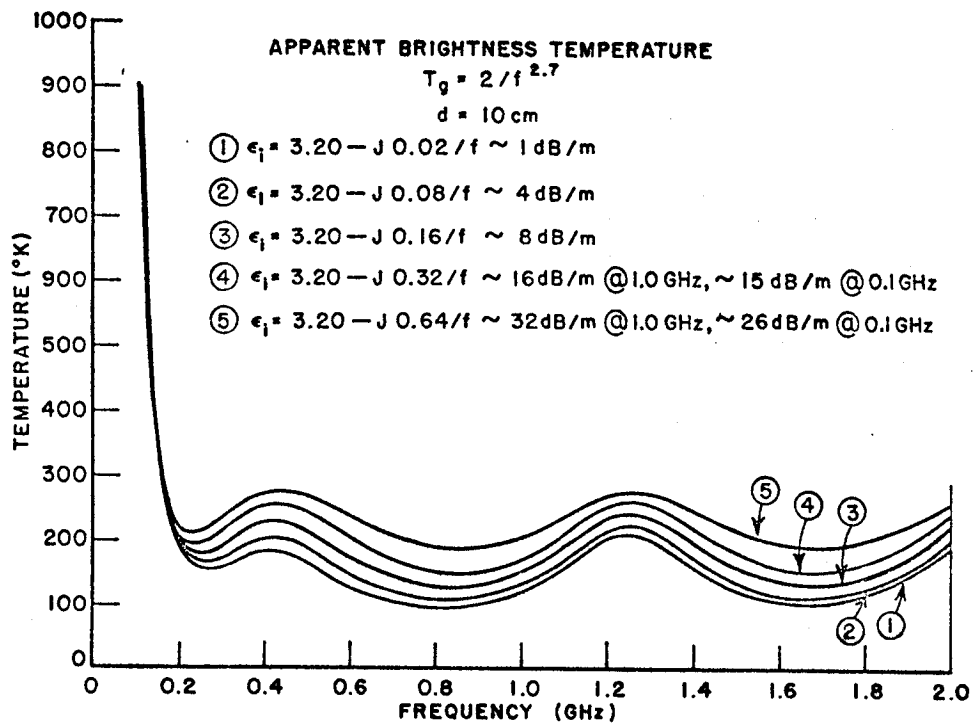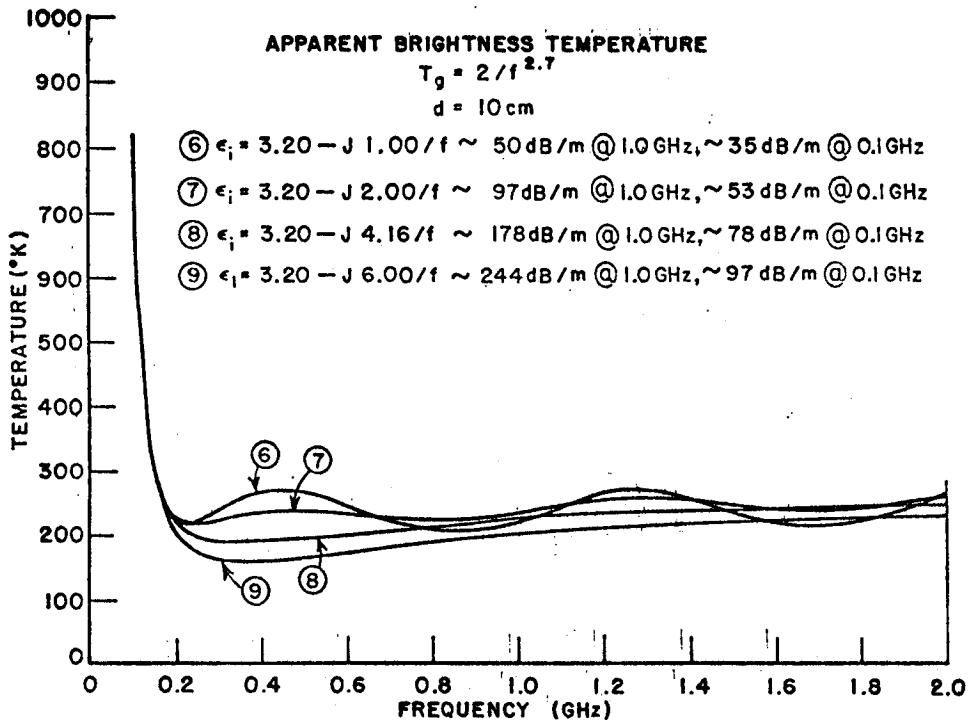
127

Figure 45 (b). Apparent brightness temperature as a function of frequency and ice loss. Ice thickness = 10 cm, water salinity = 35 ppt.

Figure 46 (a). Apparent brightness temperature as a function of frequency and ice loss. Ice thickness = 100 cm, water salinity = 35 ppt.
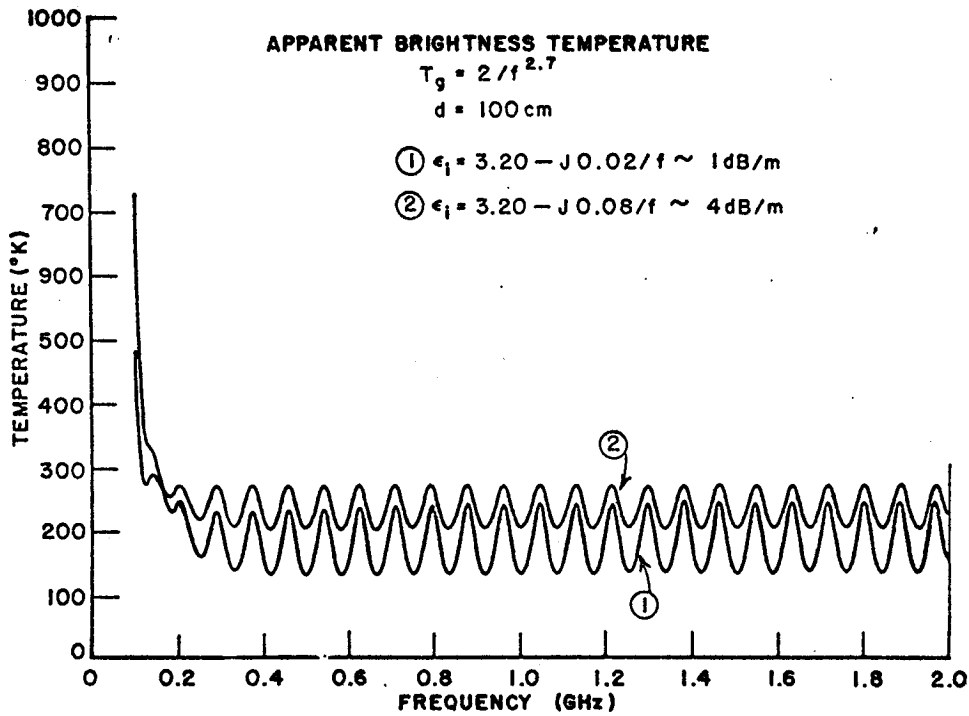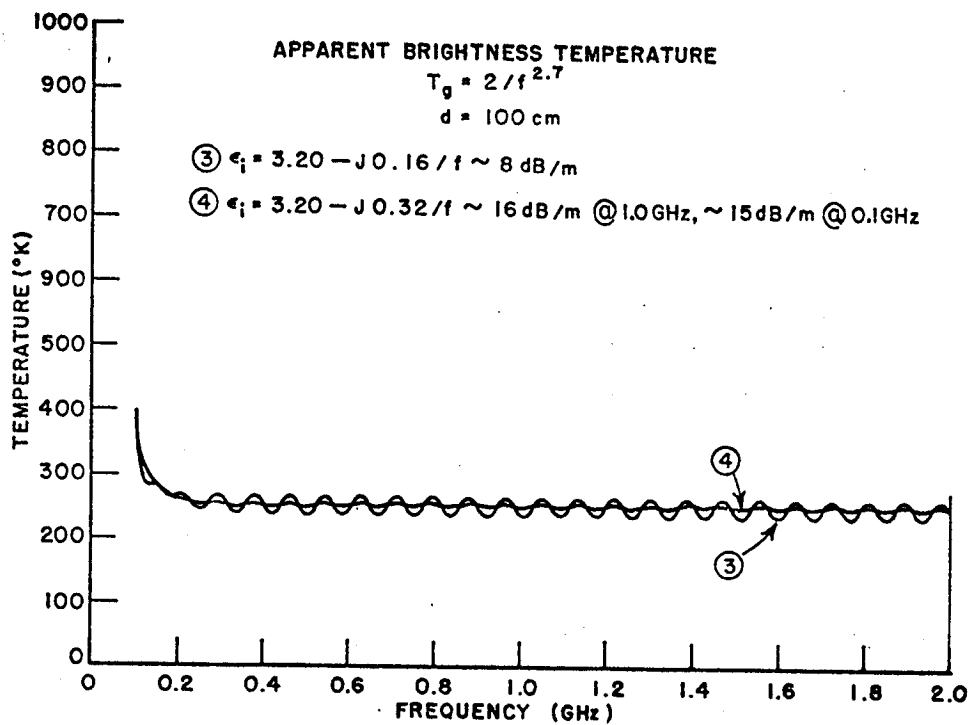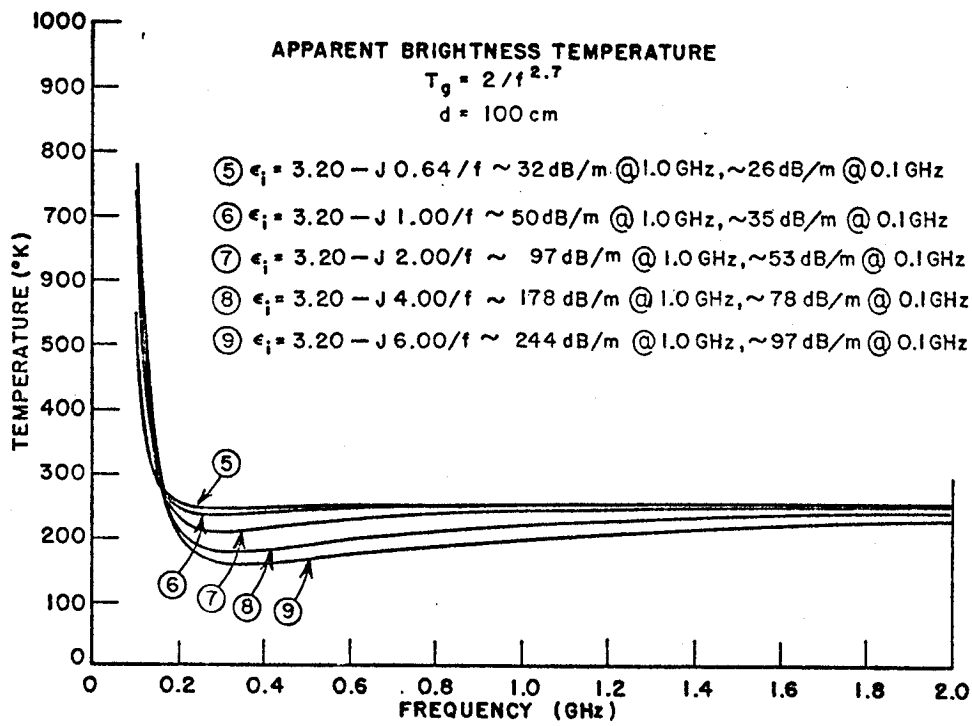
128

Figures 46 (b-c). Apparent brightness temperature as a function of frequency and ice loss. Ice thickness = 100 cm, water salinity = 35 ppt.

129

CHAPTER VIII

SYSTEM CONSIDERATIONS

0. Introduction

The preceding results show that it is feasible to measure fresh water ice thickness if brightness measurements at a sufficient number of frequencies are available. It remains to investigate the practicality of such a system from the standpoint of the required receiver sensitivity, as determined by the integration times, bandwidths, and receiver noise figures. For a mapping system, one must also consider the effects of aircraft height and velocity as they affect the scanning process. It will be shown that a range of multichannel radiometer configurations within the current state-of-the art in radiometer hardware will satisfy the performance requirements for a feasible mapping system.

1. Bandwidth

All the data processing schemes considered thus far have assumed a zero bandwidth. A radiometer, however, receives power proportional to the bandwidth, and therefore the effect of a finite bandwidth must be taken into consideration. Figure 47. shows the apparent brightness temperature as seen by radiometers at 1 GHz center frequency but with varying bandwidths. This calculation was performed by averaging the apparent brightness temperatures of a number of frequencies distributed about a center frequency, in this case 1 GHz. Thus the calculation simulates the effect of an ideal bandpass filter. The effect of other types of bandpass filter shapes is considered by Popov (1976).

As the bandwidth is further increased, the apparent brightness temperature becomes modulated by the function $\sin (d \, \Delta\beta)/ (d \, \Delta\beta)$. Thus, the effect of finite bandwidth is similar to that due to multiple thickness but poses much less of a problem in practice, because the bandwidths are small. It can be seen from Figure 47. that a 10 MHz bandwidth, for example, would have a negligible effect on the apparent brightness temperature. If larger bandwidths are required to improve the sensitivity or reduce the integration time, then the smoothing effect has to be allowed for in the data processing scheme.

2. Receiver Sensitivity for Scanning Systems

The sensitivity of a radiometer is closely related to the bandwidth. A well known expression, Kraus (1966), for the minimum detectable temperature ΔT is
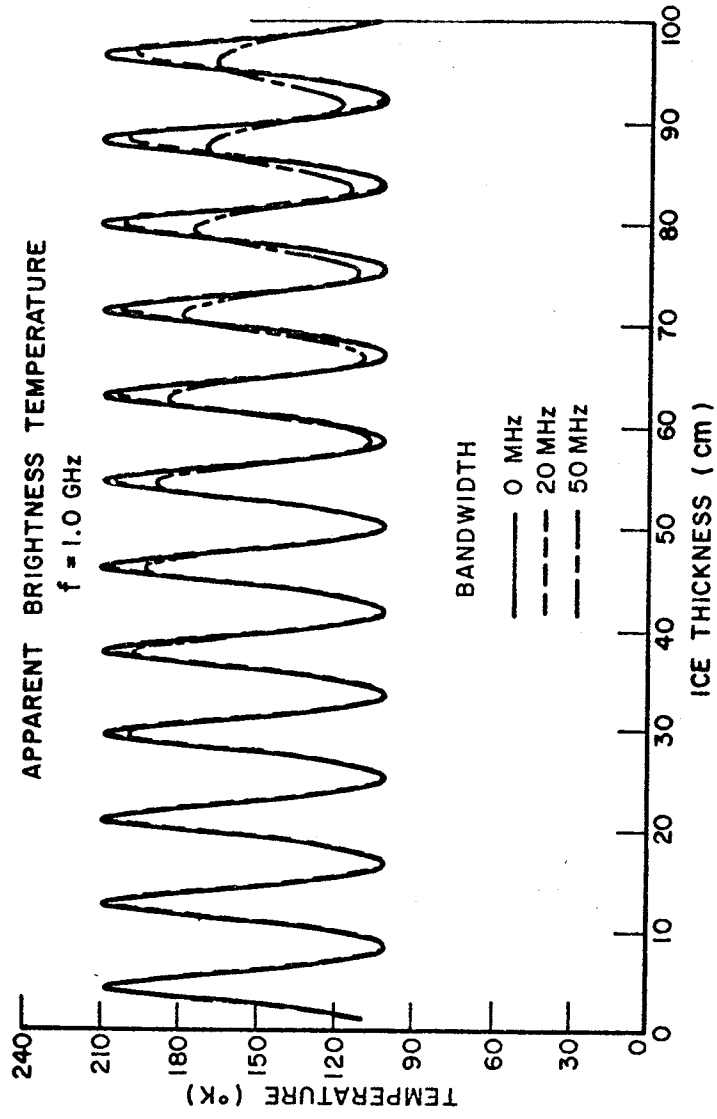
Figure 47.   The effect of finite bandwidth on the apparent brightness temperature.

131

$$\Delta T = \frac{K \, T_{sys}}{\sqrt{\Delta f \, \tau}} \qquad (8\text{-}1)$$

where

$$T_{sys} = 290. \, (F - 1) + T_{ant} \qquad (8\text{-}2)$$

K is the system constant

F is the receiver noise figure

T_{ant} is the antenna temperature

Δf is the receiver bandwidth

τ is the integration time.

The system constant K depends on the nature of the system. A Dicke receiver with square wave modulation and a narrow band video amplifier, has $K = 2.22$, for example; a total-power receiver has $K = 1.0$, Kraus (1966). A representative plot of the sensitivity as a function of the integration time for a total-power receiver is given in Figure 48. A noise figure of 4 and antenna temperatures of 100° K and 200° K have been assumed in the figure. In practice, Dicke receivers are usually employed since they greatly reduce the gain instabilities inherent in the total-power receiver, but even if the T of Figure 48. is increased by a factor of two, the sensitivity is still quite adequate in terms of the kinds of temperature errors (5°K - 10°K) which have been assumed in the thickness prediction studies of Chapter V and VI.

In a practical mapping system, the available integration times are determined by the flight velocity and system geometry. In a thickness profiling (not scanning) mode, the integration time is just the time required to fly over the antenna footprint on the ground. A brief consideration of typical aircraft velocity and altitudes shows that for any practical beamwidth, the available integration time is adequate to meet a sensitivity requirement of a few °K. The implementation of a scanning system presents a design conflict however. Good ground resolution requires that the antenna beamwidth be small, which in turn requires that the scan rate be high. High scan rates imply short integration times causing the minimum detectable temperature ΔT to increase. Consider a system in which the aircraft flies at an altitude h, with velocity v, antenna beamwidth θ_B, and a scan angle θ_s (Figure 49). If the axis of rotation is tilted ϕ_d degrees from the vertical, it is easy to show that
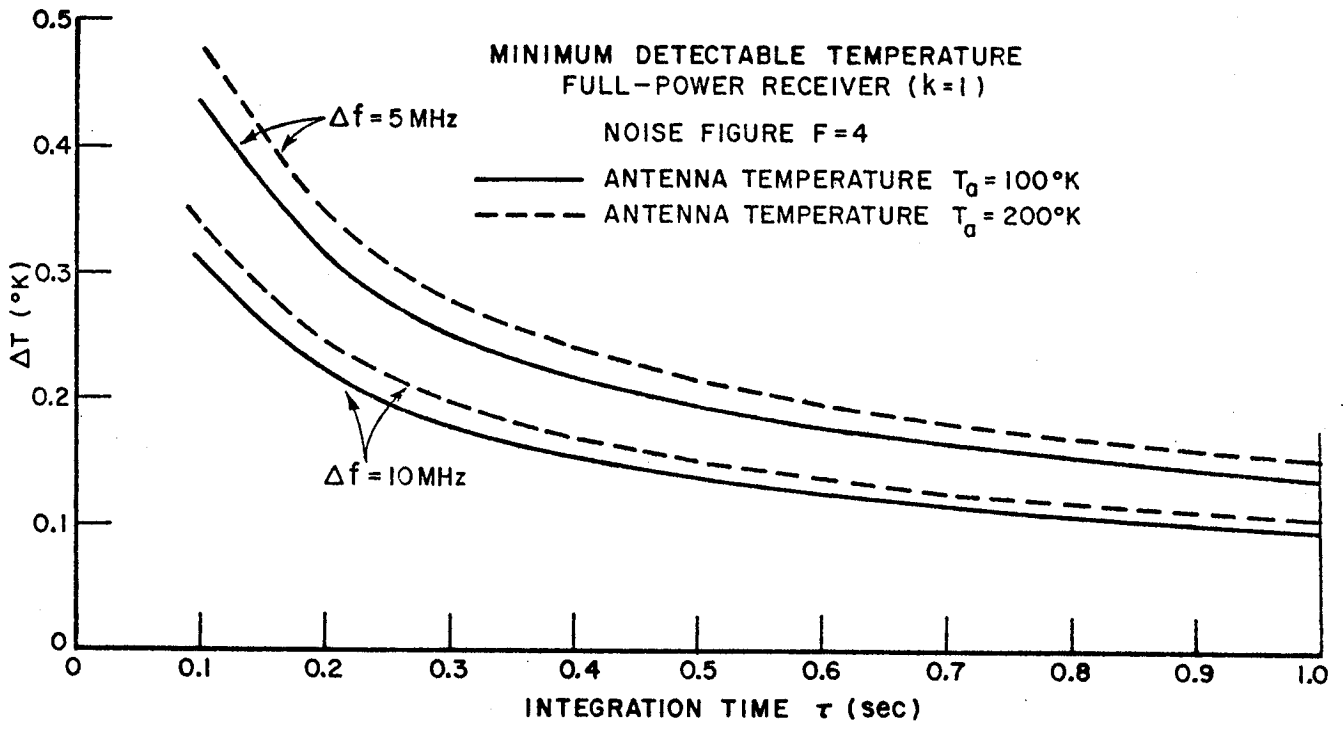
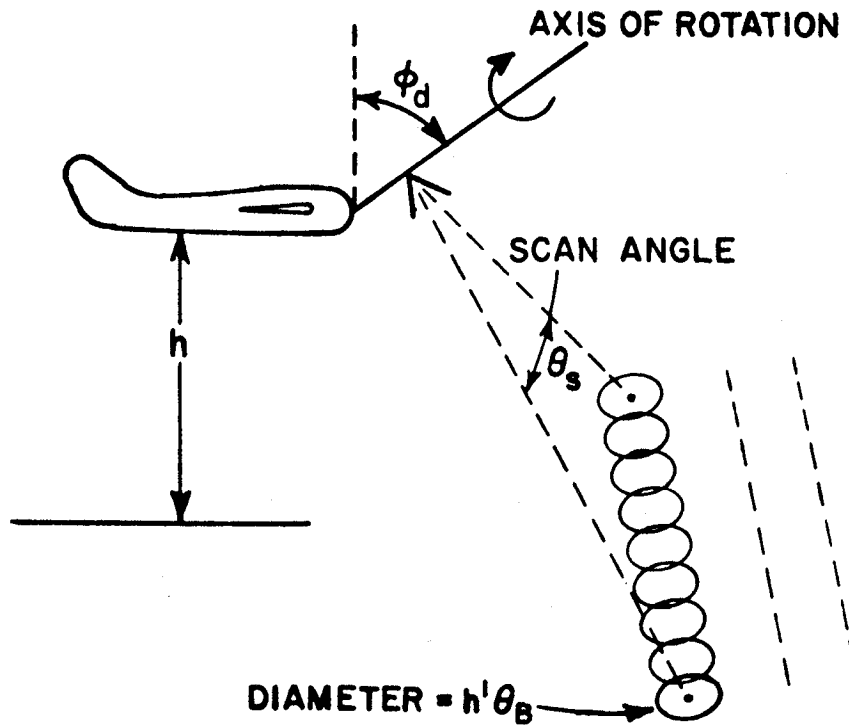Figure 48. Receiver sensitivity as a function of bandwidth and integration time.

Figure 49. Scanning geometry.

133

$$\theta_B = \frac{K \, T_{sys}}{\Delta T} \sqrt{\frac{v \, \theta_s \, \sin \phi_d}{h \, \Delta f}} \quad . \qquad (8\text{-}3)$$

This is an expression for the antenna beamwidth compatible with the specified receiver sensitivity ΔT. This beamwidth has been calculated as a function of velocity/height ratio and plotted in Figure 50. for representative values of noise figure, bandwidth, and receiver sensitivity. The calculations have assumed $K = 2.22$, $\theta_s = 60°$, $\phi_d = 90°$, and $T_a = 200°K$. As an example of a typical flight system, consider an aircraft flying 100 mph, at 2000 feet with a v/h ratio of 0.073 $\sec^{-1}$. If the system noise figure is 4 and bandwidth is 10 MHz, then $\theta_B = 10°$ for $\Delta T = 1°K$ and $\theta_B = 2°$ for $\Delta T = 5°K$. Since the results of the previous
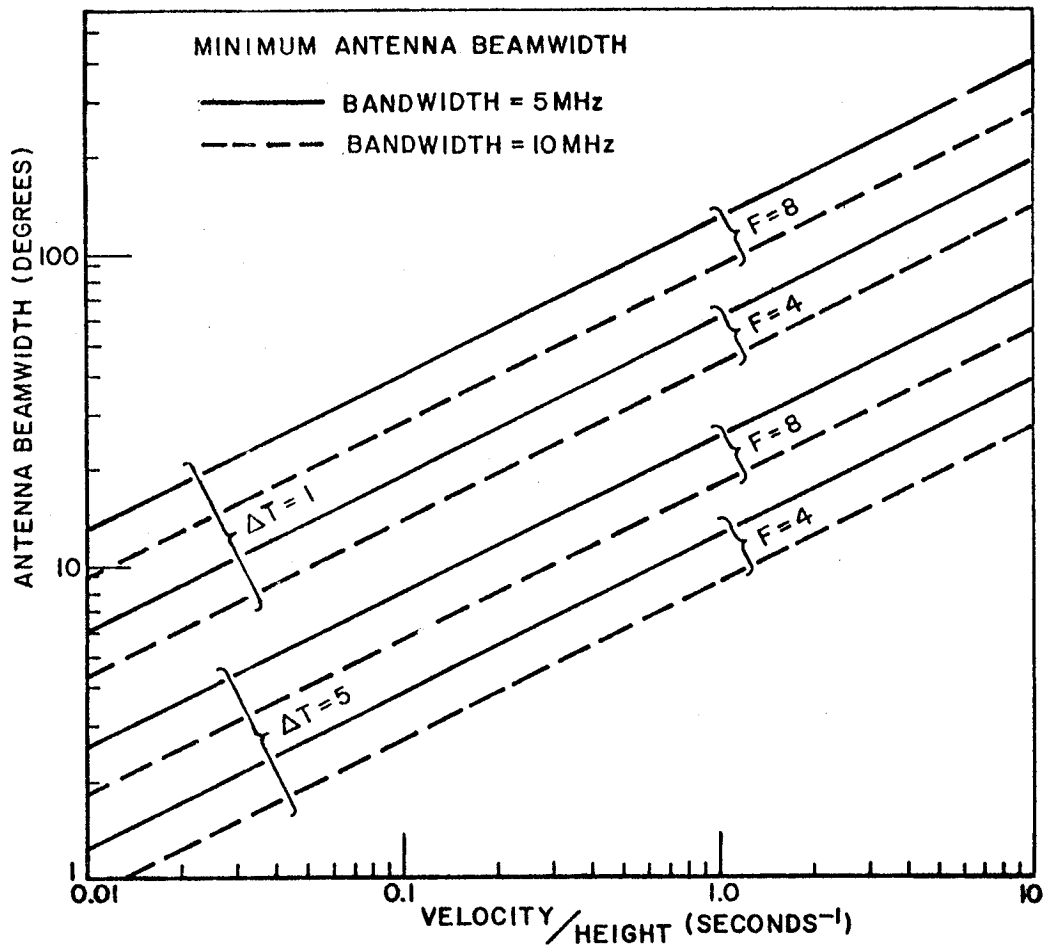

Figure 50. Required beamwidth as a function of velocity/height ratio. Curves are calculated assuming $K = 2.22$, $\theta_s = 60°$, $\phi_d = 90°$, and $T_a = 200°K$.

sections indicate that the proposed data processing systems can operate effectively with errors of the order of 5°K, it appears that for many systems of interest a beam scanning design can be implemented. For more severe operational requirements (e.g. very high speed platforms or significantly narrower beamwidths), it may be necessary to use multiple beam systems to achieve the desired sensitivity.

3. Receiver Configuration

From the discussion of data processing methods, it is clear that five, six, seven, or more frequencies are needed to predict the ice thickness. Furthermore, since the radiometer will be airborne, it is important to keep the integration time for each thickness measurement to a minimum. These two requirements dictate a parallel integration configuration, one example of which is shown in Figure 51. in which all channels are simultaneously in operation. The choice of actual system implementation (e. g. whether to achieve channel separation in the r.f. section by using multiple local oscillators or by using i.f. amplifiers of different frequencies) will depend primarily on the availability of hardware, image rejection considerations, etc..

MULTI−FREQUENCY RADIOMETER
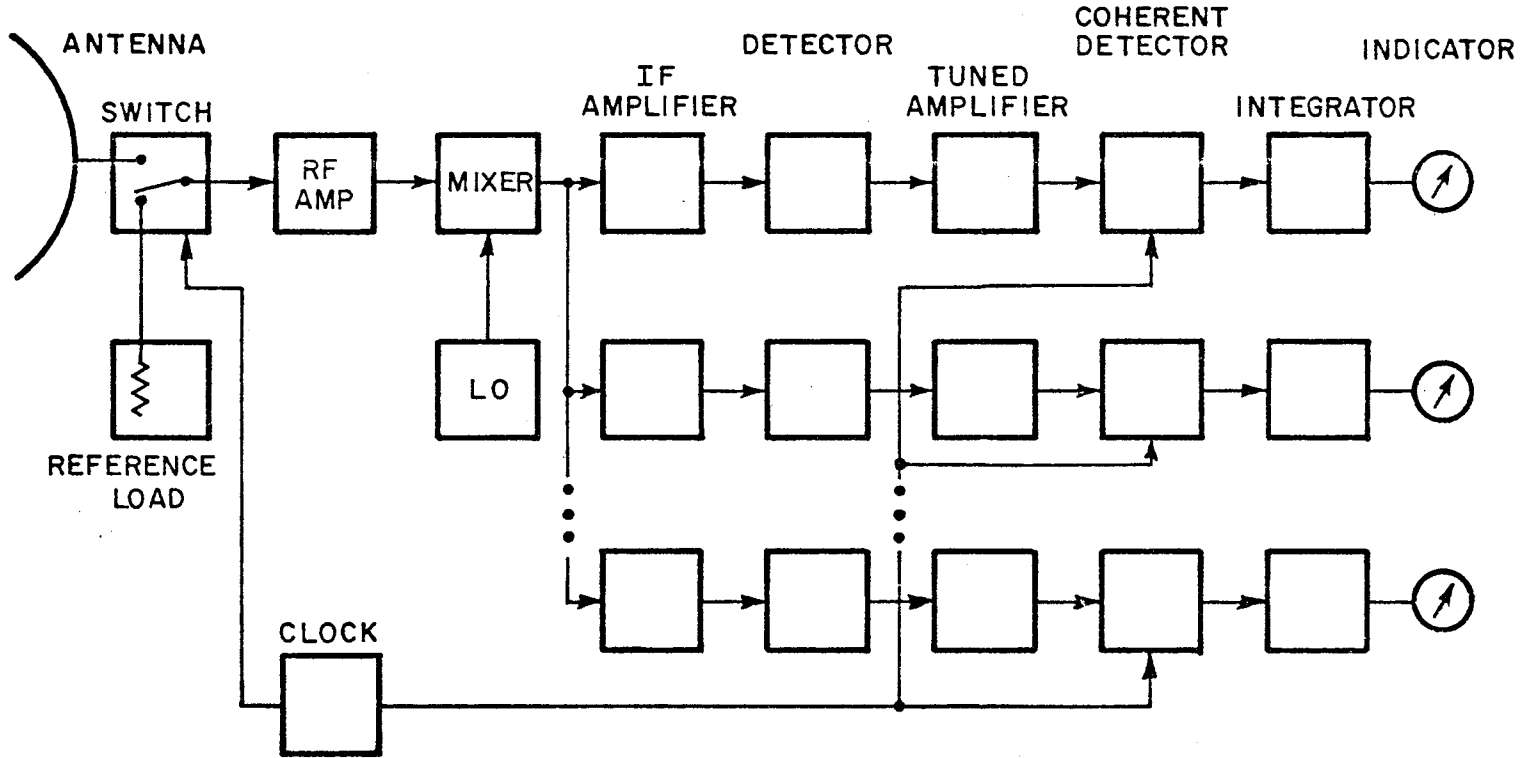
Figure 51. One possible configuration of a multichannel radiometer.

IX. CONCLUSIONS

This study presents the basic calculations from which the feasibility of a microwave radiometer system for mapping the thickness of a lake ice may be evaluated. The study is based on the well established principle that the reflection coefficient of an ice layer over water depends upon the thickness of the ice and the frequency of observation. The major emphasis in this study has been the development of mapping systems for the quantitative determination of ice thickness under realistic conditions.

An analytical model for the apparent brightness temperature as a function of ice thickness has been developed and elaborated to include such variables as galactic and atmospheric noise temperatures, aspect angle, polarization, temperature gradients in the ice, and the presence of transition layers above and below the ice. Look angles between 0° (normal incidence) and about 55° were found to give satisfactory performances; circular or 45° linear polarization gave the best results at the larger look angles. The effect of temperature gradient on the apparent brightness temperature was found to be negligible. A snow layer on top of the ice was found to act as a matching layer or an absorber depending primarily on the moisture content of the snow; a few centimeters of dry snow could be easily tolerated for most of the systems considered here. A slush or a water layer on top of the ice changes the reflection coefficient radically. Water layers more than a few mm thick were found to degrade severely the operation of any measurement system. Small scale first surface roughness was found to change the apparent brightness temperature by only a few degrees, and thus, would present no problem to thickness measuring systems. The presence of a range of ice layer thicknesses within the antenna footprint was found to place an upper limit on the usable frequency. A 10 cm variation in ice thickness, for example, limited usable frequencies to below 0.7 GHz. The presence of air bubbles in the ice layer, which tend to make the ice more lossy, was found not to degrade the thickness estimates, at least for the range of attenuation typical of fresh water ice.

The second objective of the study was the development of effective data processing methods. Two methods were developed to predict the ice layer thickness from brightness temperature measurements: the minimum-distance fit, and ternary temperature quantization. It has been found that the thickness of ice layers up to a meter can be estimated with reasonable accuracy using as few as three frequencies, but they must lie below 100 MHz, and the data processing methods must take into account the variations in galactic noise temperature. In addition, the design of an airborne antenna at such low frequencies is a formidable problem. At

137

higher frequencies (1.0 GHz or more), the antenna design problem is much more tractable, but as many as six unevenly spaced frequencies, spanning approximately .5 GHz, are needed to obtain accurate estimates of the thickness of clear uniform ice up to a meter thick. If the ice becomes lossy due to air bubbles and is of non-uniform thickness, then seven frequencies in the span .4 GHz - .7 GHz are required for the minimum-distance method. The temperature quantization method provides   performance comparable to the minimum-distance method but has the advantage that it is less sensitive to systematic temperature errors.

A brief system study has been performed to evaluate the required receiver design for an airborne scanning system. The effects of antenna beamwidth, scanning rate, bandwidth, system noise figure, and integration time were considered for typical vehicle velocity/altitude ratios. No problems are anticipated in meeting the receiver sensitivity requirements with state-of-the-art components. Thus, it has been shown that a multichannel microwave radiometer can be used to map the thickness of lake ice, subject to certain reasonable constraints upon the thickness variations and losses in the ice layer.

The feasibility of using a similar system to estimate the thickness of sea ice was also investigated. Reported loss values for sea ice are large and highly variable, depending on the state and history of the ice. Calculations show that the apparent brightness temperature is a function of sea ice layer thickness only for very thin layers (a few tens of centimeters). Radiometric methods, thus, can distinguish new ice from old ice since the brine in the old ice has partially drained out, but do not appear to be feasible for quantitative measurements of thickness of the order of a meter, unless the ice to be measured is of exceptionally low loss.

APPENDIX

Brightness Temperature From Impulse Response

It is well known from Fourier transform theory that a periodic spectral response corresponds to a set of impulse functions in the time domain and vice versa. Consider for example, the Fourier transform of two impulses in the time domain of arbitrary relative magnitudes, one at t=0, the other delayed in time by some constant τ, i.e.

$$F(j\omega) = \mathscr{F}[\delta(t) + A\delta(t-\tau)] = 1.0 + Ae^{-j\omega\tau} \quad . \quad (A-1)$$

The square of the magnitude of the function in the frequency domain is

$$|F(j\omega)|^2 = 1.0 + A^2 + 2A\cos\omega\tau \quad . \quad (A-2)$$

The argument of the cosine function can be rewritten as

$$|F(j\omega)|^2 = 1.0 + A^2 + 2A\cos\frac{2\pi f}{F} \quad , \quad (A-3)$$

the period F of this function in the frequency domain is just equal to the inverse of the time delay τ in the time domain.

This concept can be extended to consider the impulse response of the ice layer. For example, in Figure 14. is shown the impulse response of a layer 100 cm thick. This function in the time domain can be written as

$$f(t) = A_0\delta(t) + A_1\delta(t-\tau) + A_2\delta(t-2\tau) + A_3(t-3\tau) \quad ,$$

$$(A-4)$$

where the A's are the amplitudes of the impulses and τ is the spacing between successive impulses. In Figure 14., τ is approximately 12 nanoseconds. The impulse response of the ice layer is a transient containing theoretically infinitely many impulses of decreasing amplitude and alternating sign. This infinitely long train of impulses has been approximated by the first four in Equation (A-4). A Fourier transform of f(t) then is

$$[f(t)] = F(j\omega) = A_0 + A_1 e^{-j\omega\tau} + A_2 e^{-j\omega 2\tau} + A_3 e^{-j\omega 3\tau}$$

$$(A-5)$$

and with same triganometric manipulation it can be shown that

$$|F(j\omega)|^2 = A_0{}^2 + A_1{}^2 + A_2{}^2 + A_3{}^2 + 2(A_0 A_1 + A_1 A_2 + A_2 A_3)\cos\omega\tau +$$

$$2(A_0 A_2 + A_1 A_3)\cos\omega 2\tau + 2(A_0 A_3)\cos\omega 3\tau \quad .$$

$$(A-6)$$

If the amplitude values shown in Figure 14. are read off the plot and substituted into the above equation, the square of the magnitude of the transform becomes

$$|F(j\omega)|^2 = 0.46 + 0.21\cos\omega\tau - 0.04\cos\omega 2\tau + 0.01\cos\omega 3\tau \quad .$$

$$(A-7)$$

But this is just an approximate description of the power reflection coefficient for the 100 cm thickness shown in Figure 8. In this particular example, the time delay τ, in Figure 14., is approximately 12 nanoseconds, whose inverse, equal to .08 GHz, is the period of oscillation of the power reflection coefficient in Figure 8. corresponding to the 100 cm ice layer.

If $|F(j\omega)|^2$ is subtracted from unity and multiplied by 273, the physical temperature of ice in degrees Kelvin, then an approximate expression for the apparent brightness temperature is produced to the extent that the galactic and atmospheric contributions may be neglected, i.e.

$$T_b \sim (1. - |F(j\omega)|^2)\ 273 \quad . \qquad (A-8)$$

$$T_b \sim 147. - 57.\cos\omega\tau + 11.\cos\omega 2\tau - 3.\cos\omega 3\tau$$

$$(A-9)$$

This is a description of the apparent brightness temperature curve of Figure 9. for frequencies where the galactic contribution has

become negligible. The 100 cm thickness curve corresponds to $\tau = 12$ nanoseconds, the 10 cm thickness curve to $\tau = 1.2$ nanoseconds. Furthermore, the time delay τ is just the two-way propagation time through the ice layer, and therefore directly proportional to the ice layer thickness.

REFERENCES

Addison, J. R., "Electrical Properties of Saline Ice," Journal of Applied Physics, vol. 40, no. 8, July 1969, pp. 3105-3114.

Adey, A. W., et al., "Theory and Field Tests of a UHF Radiometer for Determining Sea Ice Thickness," CRC Technical Note No. 637, January 1972, Communications Research Centre, Department of Communications, Ottawa, Canada.

Adey, A. W., and Reed, G. N., "UHF Radiometer for Remote Sensing of Ships, Sea Ice, Icebergs and the Northern Environment," Canadian Aeronautics and Space Journal, vol. 19, no. 10, December 1973, pp. 528-529.

Basharinov, A. E., Gurvitch, A. S., and Igorov, S. T., "Features of Microwave Passive Remote Sensing," Proceedings of the Seventh International Symposium on Remote Sensing of Environment, Institute of Science and Technology, University of Michigan, Ann Arbor, May 1971, pp. 119-123.

Bennington, K. O., "Some Chemical Composition Studies on Arctic Sea Ice," in Ice and Snow Properties, Processes, and Applications, edited by W. D. Kingery, Cambridge, M.I.T. Press, 1963, pp. 237-247.

Biache, A., Bay, C. A., and Bradie, R., "Remote Sensing of the ArcticIce Environment," Proceedings of the Seventh International Symposium on Remote Sensing of Environment, Institute of Science and Technology, University of Michigan, Ann Arbor, May 1971, pp. 523-561.

Blinn, J. C., Conel, J. E., and Quade, J. G., "Microwave Emission from Geological Materials: Observations of Interference Effects," Journal of Geophysical Research, vol. 77, no. 23, August 1972, pp. 4366-4378.

Campbell, K. J., and Orange, A. S., "A Continuous Profile of Sea Ice and Freshwater Ice Thickness by Impulse Radar," The Polar Record, vol. 17, no. 106, 1974, pp. 31-41.

Campbell, K. J., and Orange, A. S., "The Electrical Anisotropy of Sea Ice in the Horizontal Plane," Journal of Geophysical Research, vol. 79, no. 33, November 1974, pp. 5059-5063.

Campbell, W. J., et al., "Dynamics and Morphology of Beaufort Sea Ice Determined from Satellites, Aircraft, and Drifting Stations," COSPAR Approaches to Earth Survey Problems Through Use of Space Techniques, Berlin, Akademie-Verlag, 1974, pp. 311-327.

Catoe, C. W., et al., "Preliminary Results from Aircraft Flight
     Tests of Electrically Scanning Microwave Radiometer," NASA
     Report X-622-67-352, GSFC, August 1967.

Chang, N. J., and Vickers, R. S., "A Comparative Study of Designs
     for High-Altitude Ice-Thickness Profiling Radars," SRI Project
     4090, January 1976, Stanford Research Institute, Menlo Park
     California.

Cook, J. C., "RF Electrical Properties of Salty Ice and Frozen
     Earth," Journal of Geophysical Research, vol. 65, no. 6,
     June 1960, pp. 1767-1771.

Cooper, D. W., Mueller, R. A., and Schertler, R. J., "Remote
     Profiling of Lake Ice Using an S-Band Short-Pulse Radar
     Aboard an All-Terrain Vehicle," Radio Science vol. 11,
     no. 4, 1976, p. 375.

Cumming, W. A., "The Dielectric Properties of Ice and Snow at
     3.2 Centimeters," Journal of Applied Physics. vol. 23, no.
     7, July 1952, pp. 768-773.

Edgerton, A. T., et al., "Microwave Emission Characteristics of
     Natural Materials," Aerojet General Report 9016R-8, February
     1971, Astia No. 720388.

England, A. W., and Johnson, G. R., "Microwave Brightness Spectra
     of Layered Media," to be published in Journal of Geophysical
     Research.

Evans, S., "Dielectric Properties of Snow and Ice," Journal of
     Glaciology, vol. 5, no. 42, 1965, pp. 773-792.

Gloersen, P., et al., "Microwave Signatures of First-Year and
     Multiyear Sea Ice," Report X-652-72-312, August 1972,
     Goddard Space Flight Center, Greenbelt.

Gloersen, P., et al., "Microwave Maps of the Polar Ice of the
     Earth," Bulletin of the American Meteorological Society,
     vol. 55, no. 12, December 1974, pp. 1442-1448.

Gloersen, P., et al., "Beaufort Sea Ice Zones by Means of
     Microwave Imagery," Report X-910-75-80, April 1975,
     Goddard Space Flight Center, Greenbelt.

Gudmandsen, P., "Electromagnetic Probing of Ice," in Electro-
     magnetic Probing in Geophysics, edited by J. R. Wait,
     Boulder, Golem Press, 1971, pp. 321-348.

143

Harrison, C. H., "Radio Echo Sounding of Horizontal Layers
    in Ice," Journal of Glaciology, vol. 12, no. 66, 1973,
    pp. 383-397.

Hasted, J. B., The Dielectric Properties of Water, vol. 3, Wiley
    1961.

Hoekstra, P., and Cappillino, P., "Dielectric Properties of Sea
    and Sodium Chloride Ice at UHF and Microwave Frequencies,"
    Journal of Geophysical Research, vol. 76, no. 20, July 1971,
    pp. 4922-4931.

Hoekstra, P., and Spanogle, D., "Backscatter from Snow and Ice
    Surfaces at Near Incident Angles," IEEE Trans. on Antennas
    and Propagation, vol. AP-20, no. 6, November 1972, pp. 788-790.

Hogg, D. C., and Semplak, R. A., "Effect of Rain and Water Vapor
    on Sky Noise at Centimeter Wavelengths," BSTJ, XL, 1331,
    September 1961.

Hollinger, J. P., and Manella, R. A., "Measurements of the Distri-
    bution and Volume of Sea Surface Oil Spills Using Multi-
    frequency Microwave Radiometry," NRL Report 7512, June 1973.

Iglesias, J., and Westphal, B., "Supplementary Dielectric Constant
    and Loss Measurements on High Temperature Materials," Report
    No. AD650230, January 1967, Laboratory for Insulation Research,
    Massachusetts Institute of Technology, Cambridge.

Iizuka, K., Nguyen, V. K., and Ogura, H., "Review of the Electrical
    Properties of Ice and HISS Down-Looking Radar for Measuring
    Ice Thickness," Canadian Aeronautics and Space Journal,
    December 1971, pp. 429-430.

Iizuka, K., and Nguyen, V. K., "Electrical Properties of Sea Ice,"
    Canadian Aeronautics and Space Journal, December 1971, pp.
    1728-1729.

Jean, B. R., Richerson, J. A., and Rouse, J. W., "Experimental
    Microwave Measurements of Controlled Surfaces," Proceedings
    of the Seventh International Symposium on Remote Sensing
    of Environment, Institute of Science and Technology,
    University of Michigan, Ann Arbor, May 1971, pp. 1847-1859.

Kennedy, J. M., and Sakamoto, R. T., "Passive Microwave
    Determinations of Snow Wetness Factors," Proceedings of the
    Fourth Symposium on Remote Sensing of Environment, Institute
    of Science and Technology, University of Michigan, Ann Arbor,
    April 1966, pp. 161-171.

Kingery, W. D., and Goodman, W. H., "Brine Migration in Salt Ice," in Ice and Snow Properties, Processes and Applications, edited by W. D. Kingery, Cambridge, M.I.T. Press, 1963, pp. 232-236.

Klein, L. A., and Swift, C. T., private communication.

Ko, H. C., "The Distribution of Cosmic Background Radiation," Proceedings of the I.R.E., vol. 46, January 1958, pp. 208-215.

Kraus, J. D., Radio Astronomy, New York, McGraw Hill, 1966, p. 258.

Ladely, A. E., "Radiometry for Ice Detection," The Engineers Digest (USCG), No. 154, 1967, pp. 34-38.

Landecker, T. L., and Wielebinski, R., "The Galactic Metre Wave Radiation, A Two-Frequency Survey Between Declinations +25° and -25° and the Preparation of a Map of the Whole Sky," Aust. J. Phys. Astrophys. Suppl., no. 16, 1970, pp. 1-30.

Larrowe, B. T., "Lake Ice Surveillance via Airborne Radar: Some Experimental Results," Proceedings of the Seventh International Symposium on Remote Sensing of Environment, Institute of Science and Technology, University of Michigan, Ann Arbor, May 1971, pp. 511-521.

LeSchack, L. A., "Potential Use of Satellite IR Data for Ice Thickness Mapping," Final Report on Contract 3-35384, March 1975, Development and Resources Transportation Co., Silver Spring.

Meeks, D. C., Ramseier, R. O., and Campbell, W. J., "A Study of Microwave Emission Properties of Sea Ice - AIDJEX 1972," Proceedings of the Ninth International Symposium on Remote Sensing of Environment, Environmental Research Institute of Michigan, Ann Arbor, April 1974, pp. 307-322.

Meier, M. F., and Edgerton, A. T., "Microwave Emission from Snow - A Progress Report," Proceedings of the Seventh International Symposium on Remote Sensing of Environment, Institute of Science and Technology, University of Michigan, Ann Arbor, May 1971, pp. 1155-1163.

Meyer, M. A., "Remote Sensing of Ice and Snow Thickness," Proceedings of the Fourth Symposium on Remote Sensing of Environment, Institute of Science and Technology, University of Michigan, Ann Arbor, April 1966, pp. 183-192.

Moffatt, D. L., and Puskar, R. J., "A Subsurface Electromagnetic
    Pulse Radar," Geophysics, vol. 41, no. 3, June 1976, pp.
    506-518.

Moore, R. P., and Hooper, J. O., "Microwave Radiometric Character-
    istics of Snow-Covered Terrain," Proceedings of the Ninth
    International Symposium of Remote Sensing of Environment,
    Environmental Research Institute of Michigan, Ann Arbor, April
    1974, pp. 1621-1632.

Page, D. F., Venier, G. O., and Cross, F. R., "Snow and Ice Depth
    Measurements by High Range Resolution Radar," Canadian
    Aeronautics and Space Journal, vol. 19, no. 10, December 1973,
    pp. 531-533.

Palosuo, E., and Sippola, M., "Crystal Orientation in Salt-Water
    Ice," in Ice and Snow Properties, Processes, and Applications,
    edited by W. D. Kingery, Cambridge, M.I.T. Press, 1963, pp.
    232-236.

Parashar, S. K., et al., "Investigation of Radar Discrimination
    of Sea Ice," Proceedings of the Ninth International Symposium
    on Remote Sensing of Environment, Environmental Research
    Institute of Michigan, Ann Arbor, April 1974, pp. 323-332.

Pascalar, H. G., and Sakamoto, R. T., "Ice Measurements with a
    Microwave Radiometer," Proceedings of the Third Symposium
    on Remote Sensing of Environment, Institute of Science and
    Technology, University of Michigan, Ann Arbor, October 1964,
    pp. 803-811.

Peake, W. H., "The Microwave Radiometer as a Remote Sensing
    Instrument," Report 1903-8, December 1968, The Ohio State
    University ElectroScience Laboratory, Department of Electrical
    Engineering; prepared under Contract NSR-36-008-027 for
    National Aeronautics and Space Administration.

Peake, W. H., and Oliver, T. L., "The Response of Terrestrial
    Surfaces at Microwave Frequencies," Report 2440-7, May 1971,
    The Ohio State University ElectroScience Laboratory, Department
    of Electrical Engineering; prepared under Contract F33615-67-
    C-1663 for the Air Force Avionics Laboratory, Wright-Patterson
    Air Force Base, Ohio.

Ploussios, G., "City Noise and Its Effect Upon Airborne Antenna Noise Temperatures at UHF," IEEE Transactions on Aerospace and Electronic Systems, vol. AES-4, no. 1, January 1968, pp. 41-51.

Poe, G., Stogryn, A., and Edgerton, A. T., "Microwave Emission Characteristics of Sea Ice," Report 1749R-2, 15 September 1972, Aerojet Electro Systems Company, Azusa.

Popov, A. E., and Sharkov, E. A., "Influence of Amplitude - Frequency Characteristic Shape of Microwave Radiometer on Registration of VHF Multilayer Medium Radiation," Radiotekhnika i Elektronika, vol. 21, no. 2, 1976, pp. 405-409.

Pounder, E. R., The Physics of Ice, New York, Pergamon Press, 1965.

Richmond, J. H., "Efficient   Solution for Plane and Cylindrical Multilayers," Report 1968-1, 10 August 1965, The Ohio State University ElectroScience Laboratory, Department of Electrical Engineering; prepared under Contract NOW 65-0329-d for Bureau of Naval Weapons, Washington, D. C.

Rouse, J. W., "Arctic Ice Type Identification by Radar," Proceedings of the IEEE, vol. 57, no. 4, April 1969, pp. 605-611.

Ruck, G. T., Barrick, D. E., Stuart, W. D., and Kirchbaum, C. K., Radar Cross-Section Handbook, New York, Plenum, 1970, p. 671.

Sackinger, W. M., and Byrd, R. C., "Backscatter of Millimeter Waves from Snow, Ice, and Sea Ice," IAEE Report 7207, 31 December 1972, Institute of Arctic Environmental Engineering, University of Alaska, Fairbanks.

Schmugge, T., et al., "Microwave Signatures of Snow and Fresh Water Ice," Report X-652-73-335, November 1973, Goddard Space Flight Center, Greenbelt, Maryland.

Seeger, C. L., Stumpers, F. L. H. M., and Van Hurck, N., "A 75 cm Receiver for Radio Astronomy and Some Observational Results," Philips Technical Review, vol. 21, no. 11, September 1960, pp. 317-348.

Simpson, R. A., "Electromagnetic Reflection and Transmission at Interfaces Involving Graded Dielectrics with Applications to Planetary Radar Astronomy," IEEE Trans. on Antennas and Propagation, vol. AP-24, no. 1, January 1976, pp. 17-24.

Sivaprasad, K., Stotz, K. C., and Surungi, N. N., "Reflection of
     Pulses at Oblique Incidence from Stratified Dispersive Media,"
     IEEE Trans. on Antennas and Propagation, vol. AP-24, no. 1,
     January 1976, pp. 95-99.

Skomal, E. N., "Distribution and Frequency Dependence of Incidental
     Man-Made HF/VHF Noise in Metropolitan Areas," IEEE Transactions
     on Electromagnetic Compatibility, vol. EMC-11, no. 2, May 1969,
     pp. 66-75.

Skomal, E. N., "Analysis of Airborne VHF/UHF Incidental Noise over
     Metropolitan Areas," IEEE Transactions on Electromagnetic
     Compatibility, vol. EMC-11, no. 2, May 1969, pp. 76-83.

Smith, B. M. E., and Evans, S., "Radio Echo Sounding: Absorption
     and Scattering by Water Inclusion and Ice Lenses," Journal
     of Glaciology, vol. 11, no. 61, 1972, pp. 133-146.

Sperry Microwave Electronics Division, "AN/AAR-33 Airborne Radio-
     meter System," Final Report on Contract TCG-02692-1A, December
     1967, Sperry Rand Corporation, Clearwater.

Stogryn, T., "Equations for Calculating the Dielectric Constant
     of Saline Water," IEEE Transactions on Microwave Theory and
     Techniques, August 1971, pp. 733-736.

Strong, A. E., and Fleming, M. H., "Aircraft Microwave Measurements
     of the Arctic Ice Pack," ESSA Technical Memorandum NESCTM 25,
     August 1970, Washington, D. C.

Thorndike, A. S., et al., "The Thickness Distribution of Sea Ice,"
     Journal of Geophysical Research, vol. 80, no. 33, November
     1975, pp. 4501-4513.

Tiuri, M., Hallikinen, M., and Kaski, K., "Experiments on Remote
     Sensing of Sea Ice Using a Microwave Radiometer," Report
     S 67, 1974, Radio Laboratory, Helsinki University of Technology,
     Otaniemi, Finland.

Tiuri, M., et al., "Passive Radiowave Sensing of the Thickness
     and Other Characteristics of Sea Ice," Tenth International
     Symposium on Remote Sensing of Environment, Environmental
     Research Institute, University of Michigan, Ann Arbor,
     October 1975.

Tou, J. T., and Gonzales, R. C., Pattern Recognition Principles,
     London, Addison-Wesley, 1974.

Tsang, L., and Kong, J. A., "Microwave Remote Sensing of a Two-Layer Random Medium," IEEE Trans. on Antennas and Propagation, vol. AP-24, no. 3, May 1976, pp. 283-288.

Valenzuela, G. R., "The Effective Reflection Coefficients in Forward Scatter from a Dielectric Slightly Rough Surface," Proceedings of the IEEE, vol. 58, no. 8, 1970, p. 1279.

Vickers, R. S., and Rose, G. C., "High Resolution Measurements of Snow Pack Stratigraphy," Proceedings of the Eighth International Symposium on Remote Sensing of Environment, Environmental Research Institute of Michigan, Ann Arbor, October 1972, pp. 261-277.

Vickers, R. S., Heighway, J. E., and Gedney, R. T., "Airborne Profiling of Ice Thickness Using a Short Pulse Radar," Advanced Concepts and Techniques in the Study of Snow and Ice Resources, an Interdisciplinary Symposium, National Academy of Sciences, Washington, D. C., 1974, pp. 422-431.

Vickers, R. S., "Microwave Properties of Ice from the Great Lakes," SRI Project 3571, January 1975, Stanford Research Institute, Menlo Park, California.

Von Hippel, A. R., Dielectric Materials and Applications, Cambridge, M.I.T. Press, 1961, p. 301.

Wilheit, T., "Aircraft Measurements of Microwave Emission from Arctic Sea Ice," Remote Sensing of Environment, vol. 2, 1972, pp. 129-139.

Yaplee, B. S., et al., "Nanosecond Radar Observation of Ocean Surface from a Stable Platform," IEEE Transactions on Geophysical Electronics, GE-9, 1971, pp. 170-174.

Yoshino, T., "The Reflection Properties of Radio Waves on the Ice Cap," IEEE Trans. on Antennas and Propagation, vol AP-15, no. 4, July 1967, pp. 542-551.

Yosida, A., Ice and Snow, Properties, Processes, and Applications, edited by W. D. Kingery, Cambridge, M.I.T. Press, 1963, pp. 485-527.

ADDITIONAL BIBLIOGRAPHY

Archibald, D. C., "An Aerial Ice Reconnaissance Platform with Remote Sensors Suitable for the Canadian Ice Reconnaissance Program," Sea Ice, Proceedings of an International Conference, Reykjavik, Iceland, May 10-13, 1971.

Auty, R. P., and Cole, R. H., "Dielectric Properties of Ice and Solid D_2O," Journal of Chemical Physics, vol. 20, no. 8, August 1952, pp. 1309-1314.

Bader, H., "The Physics and Mechanics of Snow as a Material," U. S. Army Cold Regions Research and Engineering Laboratory, Corps of Engineers, Hanover, New Hampshire, July 1962.

Bennington, K. O., "Some Crystal Growth Features of Sea Ice," Journal of Glaciology, vol. 4, no. 36, 1963, pp. 669-688.

Bennington, K. O., "Desalination Features in Natural Sea Ice," Journal of Glaciology, vol. 6, no. 48, 1967, pp. 845-857.

Cox, G. F. N., and Weeks, W. F., "Salinity Variations in Sea Ice," Journal of Glaciology, vol. 13, no. 67, 1974, pp. 109-120.

Evans, S., Drewry, D. J., and Robin, G. de Q., "Radio - Echo Sounding in Antarctica, 1971-72," The Polar Record, vol. 16, no. 101, 1972, pp. 207-212.

Frankenstein, G., and Garner, G., "Equations for Determining the Brine Volume of Sea Ice From -0.5° to -22.9° C," Journal of Glaciology, vol. 6, no. 48, 1967, pp. 943-944.

Gribbon, P. W. F., "Dielectric Relaxation in Temperate Glaciers," Journal of Glaciology, vol. 6, no. 48, 1967, pp. 897-909.

Jiracek, G. R., and Bentley, L. R., "Velocity of Electromagnetic Waves in Antarctic Ice," Antarctic Snow and Ice Studies II, vol. 16, Antarctic Research Series, Washington D. C., American Geophysical Union, 1971.

Lake, R. A., and Lewis, E. L., "Salt Rejection by Sea Ice During Growth," Journal of Geophysical Research, vol. 75, no. 3, January 1970, pp. 583-597.

Paige, R. A., "Stalactite Growth Beneath Sea Ice," Science, vol. 167, January 1970, pp. 171-172.

Sater, J. E., Ronhovde, A. G., and Van Allen, L. C., Arctic Environment and Resources, Washington, D. C., The Arctic Institute of North America, 1971.

Trepov, G. V., and Khokhlov, G. P., "Interferometri Measurements of the Electrical Parameters of the Ice Cover in the Meter Wavelength Range," The Physics of Ice, edited by V. V. Bogorodskii, Leningrad, Gidrometeorologicheskoe Izdatel' stvo, 1970, Israel Program for Scientific Translations, Jerusalem, 1971.

Vant, M. R., et al., "Dielectric Properties of Fresh and Sea Ice at 10 and 35 GHz," Journal of Applied Physics, vol. 45, no. 11, November 1974, pp. 4712-4717.

Walford, M. E. R., "Field Measurements of Dielectric Absorption in Antarctic Ice and Snow at Very High Frequencies," Journal of Glaciology, vol. 7, no. 49, 1968, pp. 89-94.

Yakovlev, G. N., Studies in Ice Physics and Ice Engineering, Leningrad, Gidrometeorologicheskoe Izdatel'stvo, 1971, Israel Program for Scientific Translations, Jerusalem, 1973.

Zubov, N. N., Arctic Ice, Izdatel'stvo Glavsevmorputi, Moscow.